Insights into the nature of iron based Fischer-Tropsch catalysts

Janbroers, Stephan

DOI
10.4233/uuid:e045dc8c-ebaa-4fae-b43a-5e3cc6028d2e

Publication date
2018

Document Version
Final published version

Citation (APA)
Janbroers, S. (2018). *Insights into the nature of iron based Fischer-Tropsch catalysts.* [Dissertation (TU Delft), Delft University of Technology]. https://doi.org/10.4233/uuid:e045dc8c-ebaa-4fae-b43a-5e3cc6028d2e

Important note
To cite this publication, please use the final published version (if applicable).
Please check the document version above.

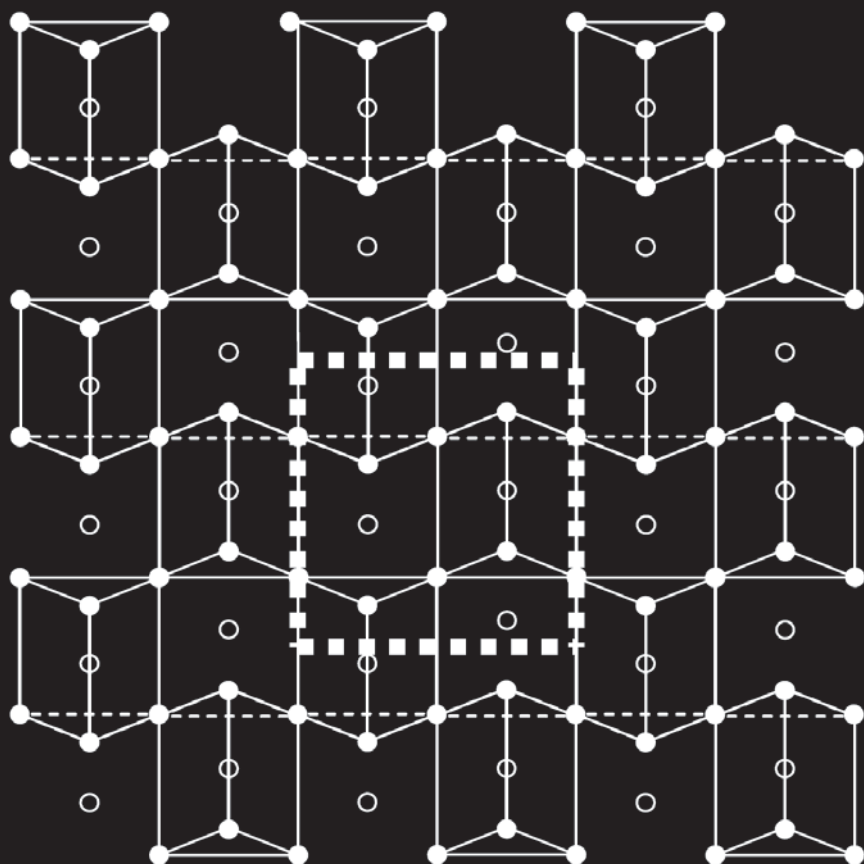# Insights into the nature of iron-based Fischer–Tropsch catalysts

Stephan Janbroers

Insights into the nature of iron-based Fischer–Tropsch catalysts

Insights into the nature of iron-based Fischer–Tropsch catalysts

Dissertation

for the purpose of obtaining the degree of doctor

at Delft University of Technology

by the authority of the Rector Magnificus

prof. dr. ir. T.H.J.J. van der Hagen

chair of the Board for Doctorates

to be defended publicly on

Tuesday 19 June 2018 at 12:30 o'clock

by

Stephan JANBROERS

HBO-ingenieur in Algemene Chemie,

Hogeschool van Amsterdam, The Nederlands

born in Amsterdam, The Nederlands

This dissertation has been approved by the
promotor: Prof. dr. H.W. Zandbergen
second promotor: Prof. dr. P.J. Kooyman

Composition of the doctoral committee:

Rector Magnificus   chairman
Prof. Dr. H.W. Zandbergen   Delft University of Technology
Prof. Dr. P. J. Kooyman   University of Cape Town

Independent members:

Prof. dr. J.J.C. Geerlings   Delft University of Technology
Prof. dr. E.A. Pidko   Delft University of Technology
Prof. dr. E.T.C. Vogt   Utrecht University
Prof. dr. J.W.M. Frenken   University of Amsterdam
Dr. T.W. Hansen   Technical University of Denmark
Prof. dr. ir. M. Makkee   Delft University of Technology

Outline of this thesis

This thesis is focused on iron based Fischer-Tropsch catalysts. It deals with different iron phases that might play a role in the catalysis. As the activation step takes place inside the reactor (in-situ at high temperature and pressure), studying the activation process is not trivial. As a result, the identity of the real active phase is still unknown. It is believed that iron carbides are the key components, being 5 times more active than iron oxides[1,2]. Also free carbon is thought to play an essential role in the catalytic process[3–6]. However, it was also suggested that part of this carbon is an artefact and could have been formed by air exposure during sample handling prior to analysis[7].

It is known that many published ex-situ characterization studies are unsuccessful[8], since the samples are sensitive to air exposure. During contact with ambient air, the catalyst is oxidized extensively and no information can be obtained anymore on the actual working catalyst. It was suggested that the best one can do is to perform a passivation, which is to expose the specimen to air under controlled conditions in order to prevent excessive oxidation. This method has been used in detailed TEM-EELS characterization studies[7,9]. Nevertheless, any oxidation (controlled or not) inevitably changes the active state of the catalyst surface under study.

To overcome this problem, (quasi) in-situ measurements can be performed, preventing exposure to air. This has been done extensively using X-Ray Diffraction (XRD) and Mössbauer spectroscopy[1,10–12]. However, these bulk techniques lack spatial resolution and do not necessarily give information on the catalyst surface, which is where the catalytic reactions take place. Recently, a study using in situ transmission X-ray microscopy (STXM) showed a large improvement in this respect, achieving a spatial resolution of several tens of nm[13,14]. It was demonstrated STXM is suitable to chemically image a catalyst under industrial relevant conditions. A technique that provides very high spatial resolutions (in the nm range) is HRTEM or STEM in combination with EELS[15]. However, the activated or used catalysts have to be transferred to the electron microscope without exposure to air. For this, a special sample holder is required[16] as is available at Delft University of Technology.

It is my aim to study iron based Fischer-Tropsch catalysts by doing (quasi) in-situ measurements on catalysts that have not been exposed to air and shed more light on the active phases in iron based catalysts.

Chapter 1

In this chapter I present an introduction and review of the research field.

Chapter 2

Here I demonstrate the detrimental effects of exposure to air of an activated iron based Fischer-Tropsch catalyst. In other words, it shows the need for careful sample handling in order to obtain relevant data.

Chapter 3

A detailed electron diffraction study on an activated catalyst is presented that has not been exposed to air. Interestingly, a specific Θ_∞-Fe_2C iron carbide is found that for a long time has been designated as a 'hypothetical' iron phase.

Chapter 4

This chapter describes a study where an oxidic catalyst precursor is activated inside an electron microscope (ETEM) in an attempt to follow the carburization process on a nanometer scale using HRTEM and EELS. Two catalysts are described, one non-promoted and one promoted with potassium.

Chapter 5

Catalytic performance data is presented for all catalysts that have been described in this thesis.

Chapter 6

Since the catalysts itself contain carbon, it is helpful to use stable, carbon free grids, in the TEM. This chapter describes a very practical way to prepare carbon free TEM grids that proved to be essential for many of the results presented in this thesis.

Chapter 7

This chapter contains the final conclusions.

References

1.   Davis, B. H. Fischer-Tropsch synthesis: relationship between iron catalyst composition and process variables. *Catal. Today* **84,** 83–98 (2003).

2.   Zhang, Y., Sirimanothan, N., O'Brien, R. J., Hamdeh, H. H. & Davis, B. H. Study of deactivation of iron-based Fischer-Tropsch synthesis catalysts. *Stud. Surf. Sci. Catal.* **139,** 125–132 (2001).

3.   Niemantsverdriet, J. W., Van Der Kraan, A. M., Van Der Baan, H. S. & Van Dijk, W. L. Behavior of metallic iron catalysts during Fischer-Tropsch synthesis studied with Moessbauer spectroscopy, x-ray diffraction, carbon content determination, and reaction kinetic measurements. *J. Phys. Chem.* **84,** 3363–3370 (1980).

4.   Reymond, J. P., Meriaudeau, P. & Teichner, S. J. Changes in the surface structure and composition of an iron catalyst of reduced or unreduced iron(IV) oxide during the reaction of carbon monoxide and hydrogen. *J. Catal.* **75,** 39–48 (1982).

5.   Bukur, D. B., Lang, X. & Ding, Y. Pretreatment effect studies with a precipitated iron Fischer-Tropsch catalyst in a slurry reactor. *Appl. Catal., A* **186,** 255–275 (1999).

6.   Bian, G., Oonuki, A., Koizumi, N., Kobayashi, Y. & Yamada, M. Syngas adsorption on precipitated iron catalysts reduced by H2, syngas or CO and on those used for high-pressure FT synthesis by in situ diffuse reflectance FTIR spectroscopy. *Appl. Catal., A* **219,** 13–24 (2001).

7.   Graham, U. M., Dozier, A. K., Srinivasan, R., Thomas, M. & Davis, B. H. Formation and characterization of nanozones in iron catalysts for Fischer-Tropsch synthesis. *Prepr. - Am. Chem. Soc., Div. Pet. Chem.* **50,** 178–181 (2005).

8.   Shroff, M. D. & Datye, A. K. The importance of passivation in the study of iron Fischer-Tropsch catalysts. *Catal. Lett.* **37,** 101–106 (1996).

9.   Jin, Y., Xu, H. & Datye, A. K. Electron Energy Loss Spectroscopy (EELS) of Iron Fischer-Tropsch Catalysts. *Microsc. Microanal.* **12,** 124–134 (2006).

10.   Jung, H. & Thomson, W. J. Dynamic x-ray diffraction study of an unsupported iron catalyst in Fischer-Tropsch synthesis. *J. Catal.* **134,** 654–667 (1992).

11.   Jung, H. & Thomson, W. J. Dynamic x-ray diffraction study of an unreduced iron oxide catalyst in Fischer-Tropsch synthesis. *J. Catal.* **139,** 375–382 (1993).

12.   Li, S. *et al.* Structural analysis of unpromoted Fe-based Fischer-Tropsch catalysts using X-ray absorption spectroscopy. *Appl. Catal., A* **219,** 215–222 (2001).

13. de Smit, E. *et al.* Nanoscale chemical imaging of a working catalyst by scanning transmission X-ray microscopy. *Nature* **456,** 222–225 (2008).

14. Gonzalez-Jimenez, I. D. *et al.* Hard X-ray Nanotomography of Catalytic Solids at Work. *Angew. Chem. Int. Ed. Engl.* (2012).

15. Lazar, S., Zandbergen, H. W., Botton, G. A., Wu, M.-Y. & Tichelaar, F. D. Materials science applications of HREELS in near edge structure analysis and low-energy loss spectroscopy. *Ultramicroscopy* **96,** 535–546 (2003).

16. Zandbergen, H. W., Kooyman, P. J. & an Langeveld, A. D. Electron Microscopy 1998, proceedings ICEM 14. in *Electron Microscopy 1998, proceedings ICEM 14* **II,** 491–492 (1998).

Contents

1

Introduction

1.1.   General introduction

The work described in this thesis concerns catalysts used in the so called Fischer-Tropsch synthesis (FTS) where synthesis gas (a mixture of hydrogen and carbon-monoxide) is transformed into larger molecules. More specifically, synthesis gas can be converted into fuels, specialty chemicals and high quality waxes.
Fischer-Tropsch fuels are of very high quality: they are free of aromatics and sulfur in contrast to transportation fuels derived from crude oil. Different oil companies are interested in the Fischer-Tropsch process since aromatics and sulfur are subject to more and more stringent legislation.

FTS is a polymerization process to produce hydrocarbons. The (simplified) reaction can be expressed as:

$$n\ CO + (2n + 1)\ H_2 \rightarrow C_nH_{2n+2} + n\ H_2O \hspace{3cm} \text{(eq. 1)}$$

On a catalyst surface, CO is adsorbed and then hydrogenated to form CHx monomers that, in its turn, can react with adsorbed alkyl groups. These groups can then either undergo ß-hydrogen abstraction leading to α-olefins or hydrogen addition leading to n-paraffin's. Under typical FTS conditions, α-olefins can re-adsorb and re-initiate CHx addition forming larger hydrocarbons. The proposed scheme as was published by Iglesia[1] is shown in Figure 1.1.1.
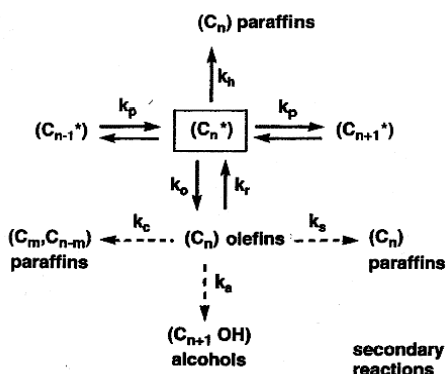
Figure 1.1.1: Chain growth pathways and possible secondary olefins in FT synthesis

The final chain length can be explained by selective inhibition or desorption. Based on typical FT products the relative rates can be depicted as follows[2]:
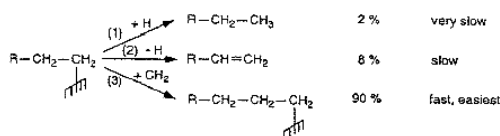
Figure 1.1.2: Relative reaction rates for desorption of (1) paraffin, (2) olefin, (3) chain prolongation

The chain growth reactions are assumed to start by insertion of a CH_2 monomer (bound to the surface) into an alkyl species also chemically bound to the surface[3]. Other mechanisms such as CO insertion are regarded as minor reactions as proven by experiments with labeled olefins[2,4]

The catalysts are usually based on cobalt or iron[5], each having their own advantages and disadvantages. In the current project, the focus will be on iron-based catalysts. The advantages of iron over cobalt are: relatively low cost, wide availability of iron, a high selectivity towards larger 'diesel' molecules[6,7] and water-gas-shift (WGS) activity as will be explained below.

The syngas is often derived from natural gas (e.g. by steam reforming), via coal- or biomass gasification[8]. Coal is an interesting raw material since there are very large reserves in the world. It can be seen as an interim fuel source when conventional oil is becoming too expensive or is depleted and sustainable alternatives have not yet been fully developed.

Typically, a high carbonacious feedstock leads to a syngas with H_2/CO ratio below 2[9]. Such syngas does not meet the stoichiometry requirements to make hydrocarbons as can be seen in equation 1. An advantage of iron-based catalysts is their ability to perform the WGS reaction[10]. In this reaction excess CO reacts with water to form additional hydrogen:
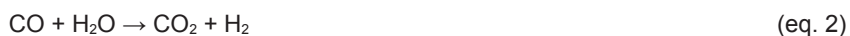
$$CO + H_2O \rightarrow CO_2 + H_2 \qquad\qquad\qquad (eq. 2)$$

Note that due to the WGS reaction, a syngas with a relatively low H_2/CO ratio can be used. Such syngas is typically obtained from coal or biomass. Downside however, is that a substantial amount of CO is converted into CO_2, making the iron based Fischer-Tropsch process less carbon-efficient. Next to this, CO_2 lowers the rate of hydrocarbon formation since it negatively influences the CO adsorption[11].

The rate of the of WGS reaction is defined as the rate of CO_2 formation (in mole CO_2^{-1} h^{-1} g^{-1}). The reaction is in itself dependent on the H_2O formed during the FT

reaction. As a consequence, the rate of WGS (r_{WGS}) can never exceed the rate of FT (r_{FT}).

The WGS equilibrium constant is highly dependent on temperature. Based on tabulated thermodynamic data, the following expression has been derived[12]:

$$\log(K_{WGS}) = -2.4198 + 0.0003855\,T + \frac{2180.6}{T} \qquad \text{(eq. 3)}$$

where K is the WGS equilibrium constant.

From test data, the approach to the WGS equilibrium can be calculated as follows:

$$K_{WGS} = \frac{P\,CO_2\,P\,H_2}{P\,CO\,P\,H_2O} \qquad \text{(eq. 4)}$$

1.1.1. Anderson-Schulz-Flory distribution

The final product distribution can be described by the Anderson-Schulz-Flory (ASF) distribution. The ASF mechanism assumes that the ratio of chain propagation rp, and termination, rt, are independent of the hydrocarbon chain length. The resulting hydrocarbon selectivity predicted is described as:

$$m_i = \alpha\,m_i\text{-}1 = (1 - \alpha)\,\alpha^{i-1} \qquad \text{(eq. 5)}$$

where mi is the mole fraction of hydrocarbon containing i carbon atoms and α is the probability for chain growth and is related to the probability for chain growth and termination as:

$$\alpha = rp / (rp + rt) \qquad \text{(eq. 6)}$$

So the ASF distribution is a function of α. A higher alpha means longer hydrocarbon chains. An example of the theoretical chain length distribution according to ASF for α = 0.88 is given in Figure 1.1.3:
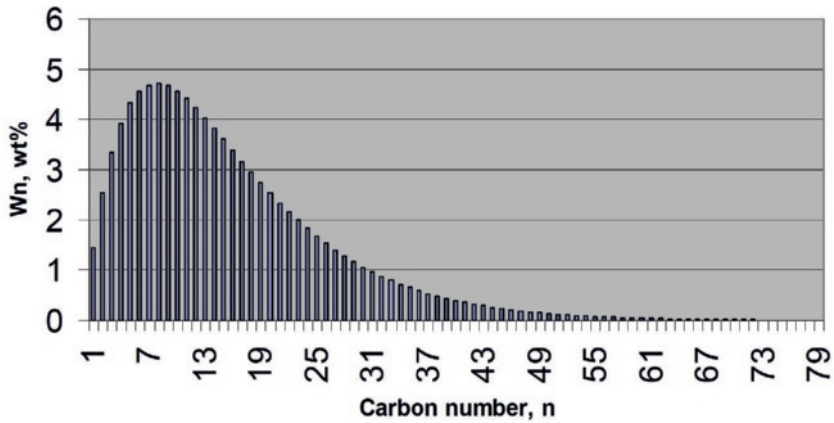
Figure 1.1.3: ASF example, alpha = 0.88

Typically, α is calculated using the ASF distribution by plotting the chain length 'n' versus the Log(Wn/n), as depicted in Figure 1.1.4. α can be calculated from the slope of the resulting line according to: $\log(\frac{W_n}{n})=n\log(\alpha)+\log\frac{(1-\alpha)^2}{\alpha}$ (eq. 7)

y = -0.0555x - 1.7861

Alpha = Inv.Log (-0.0555) = 0.88
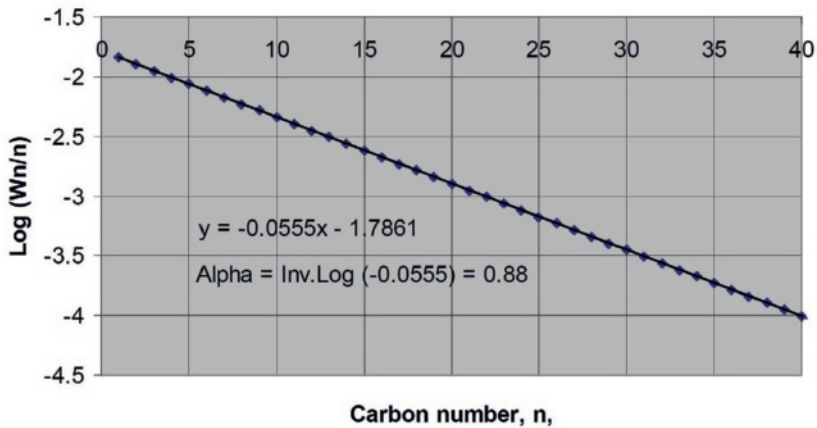
Figure 1.1.4: Carbon number (n) v.s. Log (Wn/n)

Much of the data generated however, both in small and large reactor systems, exhibit two values of α. In other words, no ideal behavior is observed. This is explained by re-adsorption of olefins that undergo further reaction and lead to higher α values[2].

1.2.   Iron based Fischer-Tropsch catalysts

Iron based Fischer-Tropsch catalysts can be prepared in different ways. In general, the best performing iron based Fischer-Tropsch catalysts are obtained via precipitation since this leads to a high number of active and accessible sites[13–17].

During precipitation, iron oxyhydroxides like FeOOH are formed. The nature of such species has been studied mainly by researchers in non-catalytic fields like the application of iron in recording media or as pigments. These studies have shown that there are different preparation variables that affect the phase composition and structure of the formed iron species during precipitation. The main parameters are: pH, temperature, solids content, the type of the precipitating agent and the iron-salt precursor[18].

The world's main source of iron in solution is ferrous sulfate, which is produced for the steel industry. However, the use of ferrous sulfate in Fischer-Tropsch is challenging since sulfate is difficult to remove from the iron precipitates while high concentrations of sulfate act as a catalyst poison[19,20]. As a result, ferric nitrate is often used as iron precursor.

Optimal catalytic behavior was observed with iron catalysts that were prepared by batch precipitation using Na_2CO_3, with a final pH between 6.8 and 8.0[21,22]. Diffenbach and Fauth[15] observed that precipitated iron catalysts prepared by continuous precipitation at pH 3.7 and 4.7, using Na_2CO_3 as a precipitant, showed unusually high olefin selectivity and stability. Anderson[22] also observed that the use of potassium, sodium, or ammonium carbonates as precipitating agents resulted in a better catalyst than when hydroxides were used. Studies by Motjope et al.[16,17] demonstrated that catalysts prepared using precipitating agents containing carbonate ions have larger pores than catalysts prepared using precipitating agents containing hydroxides. Precipitation at pH > 8, using an aqueous ammonia solution as a precipitating agent, results in the formation of large crystallites of FeOOH. Such crystallites are not observed when Na_2CO_3 and K_2CO_3 are used; in that case hematite is formed. Catalysts that contain FeOOH typically show higher CO conversion and lower selectivity towards olefins compared to catalysts that contain hematite as precursor. This is in agreement with the observations of Diffenbach and Fauth[15].

Note that a lot of research focused on catalysts that exhibit high "α", mainly for fuels production. The catalysts described in this thesis belong to this category. Note however that there is a different class of catalysts that that focuses on light olefins as building

blocks for the chemical industry (so called Fischer-Tropsch to Olefins)[23]. In this area, very interesting results were obtained using iron based Metal Organic Frameworks[24,25].

1.3. Effects of pretreatment and activation procedures

Despite almost a century of research, it is still not entirely clear what the active species in iron-based Fischer-Tropsch catalysts are. In some older papers, iron oxide was mentioned as being the most important phase for Fischer-Tropsch synthesis. However, more recent papers showed iron carbides are the most active species[26,27].

The pretreatment conditions for iron-based Fischer-Tropsch catalysts have a significant impact on the catalyst structure, steady state catalyst performance and lifetime[26,28–32]. Overall, the different pretreatment effects are not yet understood.

Luo described the different possible events occurring during the pretreatment under CO or H_2[31]. The reduction of Fe_2O_3 with CO occurs in two steps:

$$3\ Fe_2O_3 + CO \rightarrow 2\ Fe_3O_4 + CO_2 \hspace{3cm} \text{(eq. 8)}$$

$$5\ Fe_3O_4 + 32\ CO \rightarrow\ 3\ Fe_5C_2 + 26\ CO_2 \hspace{2.5cm} \text{(eq. 9)}$$

In addition, CO_2 may be formed by the Boudouard reaction:

$$2\ CO \rightarrow\ C + CO_2 \hspace{4cm} \text{(eq. 10)}$$

Typically, a CO-activated iron based catalyst contains approximately 50% to 75% more carbon than would be required to form Fe_5C_2, indicating that the Boudouard reaction indeed takes place.

The reduction of Fe_2O_3 with H_2 occurs also in two steps:

$$3\ Fe_2O_3 + H_2 \rightarrow 2\ Fe_3O_4 + H_2O \hspace{3cm} \text{(eq. 11)}$$

$$Fe_3O_4 + 4\ H_2 \rightarrow 3\ Fe + 4\ H_2O \hspace{3cm} \text{(eq. 12)}$$

Reduction in hydrogen leads to the formation of magnetite and subsequently to zero-valent iron, while in synthesis gas this metallic phase is rapidly converted into a mixture of several iron carbide phases [32–36].

Bukur et al.[28,30,37] extensively studied the effect of pretreatments using hydrogen, carbon-monoxide and syngas on the structure and final performance of precipitated iron catalysts using fixed bed- and CSTR reactors. It was shown that the BET surface areas and pore volumes decreased upon treatment with CO, H_2, or syngas. TPR results revealed that the reduction path displayed an easy reduction of Fe_2O_3 to Fe_3O_4, followed by a slow reduction to metallic iron when using H_2, or iron carbide when using CO. It was demonstrated that a catalyst reduced with hydrogen to only magnetite reached its steady state activity faster than a catalyst that was partially or completely reduced to metallic iron. In other words, catalysts that were either not reduced, or at least contained a sufficient amount of magnetite, clearly performed better than catalysts that were fully converted to metallic iron. The initial activity of the CO activated catalyst was relatively low, but increased with time. Its steady state activity was the highest among all the pretreatment procedures used. The relatively long period to reach steady-state activity for the CO activated catalysts, but also for the syngas activated catalyst, is suggested to be the result of the slow removal of carbon deposited on the surface during the pretreatment, and subsequent formation of the active sites[30,36] . This was confirmed by Shroff et al.[38], who demonstrated that a CO activated catalyst indeed displays a surface layer of carbon. It was suggested that this carbon layer protects the underlying iron carbide and is only observed when careful passivation is performed. In case the handling is not carefully performed, the catalyst surface will react with oxygen in an uncontrolled manner and the carbon surface layer is oxidized. In that case magnetite is observed, while this phase was originally not present on the surface of the catalyst.

Sudsakorn et al.[32] demonstrated that a pretreatment with hydrogen, in comparison with CO or syngas, delivered a catalyst with better porosity and a higher steady state Fischer-Tropsch activity. However, it was suggested by Davis[26] that activation in CO at 270°C for 24h will provide a good performing catalyst. The impact of pressure between 5 and 30 bar was found to be insignificant. This is partially in contradiction with Hao et al.[39] who concluded that carbides formation may be controlled primarily by activation pressure. Catalysts reduced at lower pressure contained more carbides and had higher catalyst activity.

1.4.   Promoters for iron-based Fischer-Tropsch catalysts

As described above, it is clear the specific iron phase, and the way this phase is obtained, influences the catalytic activity. Next to this, it is known that the catalyst performance can also be influenced by using chemical- and structural promoters.

1.4.1. Promotion by potassium

Potassium has long been used as a promoter for iron catalysts, and its influence on iron catalysts has been investigated by various groups[21,40–45]. Dry[21] noted that the presence of potassium results in an increase in the alkene yield and a decrease in the fraction of CH_4 that is produced. Besides, potassium can also increase the catalytic activity for Fischer-Tropsch and WGS reactions[44].

Dwyer and Hardenbergh[46] and Dictor and Bell[41] concluded that on iron surfaces potassium substantially increases the heat of adsorption of CO, decreases the heat of adsorption of H_2, and therefore enhances CO dissociation. This is in line with the higher CO adsorption found by Zhang et al[47]. In general these chemical effects are rationalized in terms of an electronic modification of the metal surface. It is believed that the adsorbed potassium ions establish a highly polarized dipole layer on the surface which lowers the work function of the system. The lower work function enhances the electron donor ability of the surface. In the case of CO this effect facilitates the back donation of electrons from the surface into anti-bonding orbitals on the molecule. The net result is an increase in the surface bond strength. Hydrogen chemisorption, on the other hand, involves the transfer of electrons to the iron surface. Therefore, hydrogen chemisorption is weaker on the potassium-modified surface, which makes that the presence of potassium decreases olefin hydrogenation.

Li et al.[40] demonstrated that potassium promotion leads to the nucleation of multiple carbide regions on iron oxide surfaces. The larger number of nucleation sites leads to higher initial carburization rates and especially to more and smaller FeC_x crystallites. These small crystallites provide higher active surface areas, shorter bulk diffusion distances, better carburization of Fe_2O_3 precursors and higher steady-state Fischer-Tropsch rates (for more details, see §1.5). It was also found that potassium does not lead to a distinct variation in the carbon species but changes the surface H/C ratio of carburized catalysts. Besides bulk iron carbide, several carbon species with different cluster sizes exist in the carburized catalysts, which have different reactivities towards hydrogen. The surface atomic carbon, the oligomerized carbon species and the bulk iron carbide are more reactive to hydrogen, whereas the large-size amorphous carbons are relatively inert to hydrogen[48] .

Next to the chemical promotion effect, it was suggested that potassium acts as a structural promoter as well because it increases the surface area of the active FeCx phases (§1.4.4).

Luo et al.[44] investigated the impact of the amount of potassium present as promoter on the Fischer-Tropsch reaction. Catalysts with different potassium loadings showed different induction periods during which the conversion increased from a low initial level

to a peak value before declining to reach stable activity. In general, it was observed that a lower K loading produced a slightly higher peak conversion and a shorter induction period, but the stabilized conversions and the stabilization periods were independent of the potassium content. Yang et al.[45] demonstrated that the impact of potassium on the performance of a precipitated iron-manganese catalyst is similar as described above for a precipitated iron catalyst.

1.4.2. Promotion by copper

Next to potassium, also copper is widely used as a promoter for iron Fischer-Tropsch catalysts[21,40,42–45,49–51].It is traditionally added to precipitated iron catalysts to facilitate the reduction of iron oxide to metallic iron by an enhanced adsorption and dissociation of H_2 on the catalyst surface. Copper has been shown to minimize sintering of iron catalysts when activating with hydrogen by significantly lowering the reduction temperature[21]. The effect of copper promotion on iron catalysts activated with carbon monoxide or syngas is not very well documented, although Koelbel and Ralek[52] have reported that only 0.1 wt% of copper is necessary for successful activation of Fe/Cu/K catalysts with syngas. Studies by Davis and coworkers[51,53,54] revealed that syngas activation at an elevated pressure (>0.80 MPa) requires the catalyst to be promoted with copper in order to achieve reasonable activity. Their work showed that promotion with copper lowered the reduction temperature and increased Fischer-Tropsch activity, regardless of the activation gas used. Carbon monoxide activation gave the highest activity for a 100Fe/4.4Si/5.2K (without copper) catalyst, while syngas activation was superior for a 100Fe/4.4Si/2.6Cu/5.2K (copper promoted) catalyst. Selectivity of the Fischer-Tropsch products was not affected by the activation gas employed or by copper promotion.

Rao et al.[42] found that copper promotion also provokes the formation of the iron carbide phase. Treatment of a 100Fe/3.6Si/0.71K (without copper) catalyst with syngas (H2:CO=0.7) for 24h at high pressure (1.31 MPa) and 270°C resulted in <18% syngas conversion. When a 100Fe/3.6Si/2.6Cu/0.71K (copper promoted) catalyst was treated similarly, it was found to undergo an induction period in which the syngas conversion increased to over 50%. Mössbauer spectroscopy analysis showed that the catalyst without Cu was composed of only Fe_3O_4, while the catalyst with Cu had been partially carbided. These results were confirmed by Li et al.[40], who revealed the structural evolution of Fe-Cu oxide precursors during exposure to syngas. The Cu-promoted Fe_2O_3 converts to Fe_3O_4 and subsequently to FeC_x more rapidly than the unpromoted Fe oxide. It was also demonstrated that CuO easily reduces to Cu^0. Once reduced, it provides sites for H_2 dissociation, which lead to adsorbed hydrogen species that reduce Fe_2O_3 to Fe_3O_4

at lower temperatures than for unpromoted Fe_2O_3. The final extent of carburization after longer contact times was also higher for Fe-Cu oxides than for the unpromoted Fe oxide samples. It was demonstrated that copper may induce the nucleation of multiple carbide regions on Fe oxide surfaces and hence results in small FeC_x crystallites with high Fischer-Tropsch activity.

1.4.3.   Promotion by alkali-earth metals

The relative impact of Group I alkali-earth metal promoters on the performance was shown to depend on the conversion level of the Fischer-Tropsch reaction[55]. Potassium is clearly the promoter that results in the highest activity at all conversion levels (see also §1.4.1). Nevertheless, at low conversions, lithium is nearly as effective as potassium in improving the catalytic activity. However, at high conversion levels it is one of the poorest promoters. At high conversions, lithium, cesium and rubidium act as inhibitors since they decrease the catalytic activity for CO conversion below that of the unpromoted iron catalyst. It has been shown by Jifan et.al that the distribution of alkali in the catalyst is dependent on the atomic radii[56–58] and influence the CO adsorption and retention of carbon species on the catalyst surface[56].

The major differences between the alkali metals at higher conversion levels are due to their impact upon the WGS reaction. At higher conversion levels, with syngas having an H_2/CO ratio of 0.7, the WGS reaction becomes rate controlling since hydrogen production becomes the rate limiting factor. Overall, the more basic the alkali promoter, the higher the rate of catalyst deactivation.

The effects of several Group II alkali-earth metals were evaluated by Luo and Davis[59] and compared to potassium promoters and the unpromoted iron catalyst. The iron-based Fischer-Tropsch catalysts promoted with Group II alkali-earth metals have generally lower overall Fischer-Tropsch activities and lower alpha values than the potassium promoted iron catalyst, but higher values than an unpromoted catalyst. Carbon dioxide rates indicate that a potassium promoted iron catalyst possesses better WGS activity than any Group II metal promoted catalyst when both are operated at high CO conversions. Calcium and magnesium can even suppress the WGS activity below that of unpromoted iron catalysts. Among the Group II metals, a barium promoted catalyst has the highest WGS activity.

In summary, all alkali-earth promoted catalysts yielded a higher liquid (C5+) and lower gas fractions than an unpromoted catalyst[59].

1.4.4. Structural promoters

One of the major problems in using an iron catalyst without structural promoters is the formation of catalyst fines accompanying physical breakage of the catalyst. In many instances, the catalyst is prepared by precipitation of the iron as a hydrous oxide, oxyhydroxide or hydroxide. Promoters may be incorporated during the precipitation step, during the washing step or just before spray-drying; but also by impregnation following spray-drying, or calcination. Most attempts to direct the structure of iron oxides by using promoters have been performed using SiO_2, ZnO, Al_2O_3, MgO and TiO_2 [21,60–70]. For a precipitated iron catalyst, structural promoters stabilize the small crystallites of the active phase and provide a robust skeletal structure that is needed to prevent breakage of the catalyst during the pretreatment and Fischer-Tropsch reaction. Hence, structural promoters are added primarily to improve or maintain surface area, and thereby to extend the lifetime of the catalyst.

For example, Zhao et al.[69] studied the BET surface areas and average pore sizes for catalysts with silica present. It was found that the BET surface area and pore volume generally increased with an increase in the total concentration of SiO_2.

It has been observed that the surface area of promoted iron oxide catalysts varies with the size of the metal promoter[65]. Promoters with an ionic radius smaller than iron produce a calcined material with a surface area higher than iron oxide while materials that contain a promoter with an ionic size larger than iron result in a material with a lower surface area than normal iron oxide. It has been demonstrated that the addition of silica or alumina enhances the surface area of iron oxide, while addition of alkali (e.g. K) or alkaline-earth (e.g. Ca) metals results in a decrease in surface area and pore volume with increasing metal-loading.

The presence of a promoter also dramatically alters the calcination behavior of a precipitated ion oxide catalyst precursor. The impact of added promoters upon the temperature at which crystallization towards hematite occurs has been shown to depend upon the ionic radius of the promoter. As the mismatch of ionic radius between the promoter and the iron ion increases, so does the temperature at which the formation of hematite occurs. In general, the temperature decreases with increasing ionic radius. The presence of small quantities of silica or alumina slows down the crystallization into hematite during calcination[65]. It was speculated by Milburn et al.[66] that when a promoter is present on the surface of the precipitated hydrous iron oxide particles, it always increases the transition temperature to form hematite.

Furthermore, structural promoters often results in a decrease in Fischer-Tropsch activity. For example, Bukur et al.[71] reported that both the Fischer-Tropsch and WGS activities decreased with increasing SiO_2 content, while obviously the stability of the catalyst was improved.

Yang et al.[62] evaluated iron–manganese catalysts with SiO_2 incorporated either by co-precipitation or as a binder after precipitation. It was found that the Fischer-Tropsch activity decreased with higher SiO_2 content, but the stability was significantly improved. The catalysts with precipitated SiO_2 displayed higher activity than those with binder SiO_2. As mentioned before, also here it was demonstrated that the incorporation of SiO_2 leads to an increase in surface area. The catalysts with co-precipitated SiO_2 showed the highest surface area strongest interaction between iron and the SiO_2 matrix compared to samples with SiO_2 as a binder. The strong iron–silica interaction inhibits the reduction in hydrogen and the carburization in syngas.

1.5. Structure and catalytic site evolution during Fischer-Tropsch reaction

As explained in paragraph 1.3, the catalysts need to be activated. This is typically done by exposing the oxidic precuror to either CO, H_2 followed by CO or a syngas mixture. Following the activation step, the iron catalyst is (almost) never at its maximum activity. During some period of time on stream, the activity and selectivity will change. The length and extent of the activity change depend on the catalyst composition and the reaction conditions. In general, an induction period is observed. This period is longer at lower temperature conditions and it is longer for catalysts with higher alkali contents as explained previously. The WGS activity of the catalyst also increases during the induction period and reaches generally a steady state value in less than 100h of FTS[26]. Since the activity and product selectivities are changing during the induction period, it is reasonable to expect that the chemical composition of the catalyst is undergoing changes as well. Besides, under reaction conditions, the reaction mixture becomes more oxidizing because of the formation of H_2O and CO_2. Initially, this induces the formation of magnetite[21,72]. However, with longer time on stream, it is said that the bulk iron is distributed among several Fe-phases, including α-Fe, Fe_3O_4, ε-Fe_3C, ε'-$Fe_{2.2}C$, χ-Fe_5C_2, and Fe_7C_3, which all have been detected in both freshly activated and used Fe-based Fischer-Tropsch catalysts[7,29,40,73,74]. Most of these phases have been proposed over time to be the active species for the Fischer-Tropsch reactions. The relative abundance of these phases depends on the reaction conditions. However, even after many (mainly ex situ) characterization studies, the composition of Fe-based Fischer-Tropsch catalysts during reaction and the identity of the active phase remain controversial.

In literature two models have been proposed regarding the role of the iron carbide phase:

1.   The carbide model[35]:

In this model, the catalytic activity is thought to be due to active surface sites located on the bulk carbide phase. The site density has been shown to follow the extent of bulk carburization.

2.   The competition model[75]:

In this model, surface iron atoms are competing for CO molecules to either form bulk carbides or hydrocarbons. Note that also here the formation of surface iron carbides is an essential step in the formation of hydrocarbons.

For both proposed reaction pathways the formation of surface iron carbides is essential, and the initial transformation of metallic iron into iron carbide induces an increase in Fischer-Tropsch activity. The decline, however, could be due to the deposition of inactive carbon on the active iron carbide surfaces. The nature of the carbon might also be important, since it is known that amorphous carbon deactivates a catalyst less severely than graphitic carbon[7].

Li et al.[40] studied the local structure and oxidation state of the starting Fe_2O_3 precursors promoted by Cu and / or K during FTS using in-situ X-ray absorption spectroscopy. It was confirmed that the activation of the Fe_2O_3 precursors occurs via the reduction to Fe_3O_4 followed by carburization to form iron carbides. Simultaneously with the initial stages of carburization the Fischer-Tropsch reaction rates increased, largely suggesting that the conversion of (near-) surface layers of Fe_3O_4 to FeC_x is sufficient for the formation of the required active sites. The initial rate of carburization, the extent of carburization and the Fischer-Tropsch rate at steady state conditions were highest for Fe_2O_3 precursors containing both Cu and K. The Cu and K promoted catalyst clearly shows an enhanced FeC_x formation, which was shown to go hand-in-hand with a higher Fischer-Tropsch activity. Based on these results, Li et al.[74] proposed a model for a promoted and unpromoted iron catalyst to describe the reduction and carburization of the Fe_2O_3 precursor in the presence of syngas. This is illustrated in Figure 1.5.1.
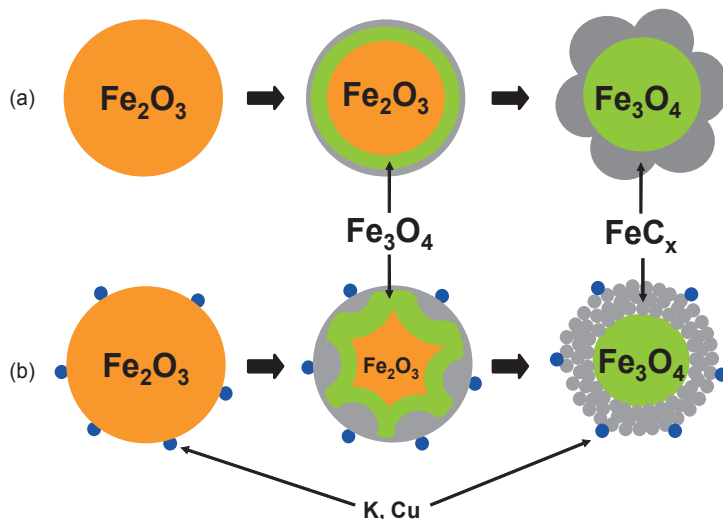
Figure 1.5.1: Shell core model

The model suggests that upon contact with syngas, lattice oxygen atoms at the Fe_2O_3 surface are removed by reaction with H_2 or CO (producing H_2O and CO_2 respectively). This leads to a different iron oxide: Fe_3O_4. The Fe_3O_4 is then converted to iron carbides (FeC_x), a reaction that is thermodynamically favored. When Cu and K are present, the H_2 and CO are activated and react with oxygen at the surface. This results in oxygen deficient regions on the surface. These rapid multiple nucleation processes lead to more fractured and accessible structures with a higher surface area that provide a larger number of sites for the Fischer-Tropsch reaction (viz. a higher activity). A nearly uniform iron carbide (FeC_x) shell will be formed on the unpromoted catalyst while on the promoted system an irregular carbide phase will be obtained. Indeed, in-situ XRD studies by Jung and Thomson[75,76] showed a fast transformation of Fe_2O_3 to Fe_3O_4 followed by a slow transformation to χ-Fe_5C_2. This also suggests a shrinking core process as explained above. The catalytic activity appeared to be directly related to the formation of χ-Fe_5C_2 and was suggested to be the active species.

In a study by Davis[26] samples of a potassium containing catalyst were withdrawn from the reactor at various reaction times during the early period of reaction (until the maximum conversion was obtained). During the induction period, Mössbauer data indicated that the sample underwent only slight changes, while dramatic changes in activity and selectivity were observed. After 24h activation the catalyst was essentially in

the carbide phase and remained in this phase as the activity and selectivity changed. A similar experiment as described above was performed, but now in a CSTR that was operated at low temperature. The phase present following activation in CO is essentially iron carbide (over 90%). Phase changes occurred with catalyst lifetime and these depended upon the catalyst composition. With an unpromoted iron catalyst, both the decline in catalytic activity and the transformation of the carbide phase to Fe_3O_4 occurred rapidly (within 200h), and were clearly related. On the other hand, for a similar catalyst but now containing potassium, the carbide phase was completely retained but the deactivation took place similarly to the unpromoted catalyst. It was demonstrated that the addition of silica retained the carbide phase. The presence of both K and Si were shown to cause synergistic effects for both the activity and carbide phase stability. Catalytic activity declined slowly, at less than 1% CO conversion/week, and the carbide phase declined to about 50% of the total iron phases (the remainder being Fe_3O_4) and then remained constant during about 3000h of synthesis.

The difference in performance between a catalyst with a significant carbide phase and a material that is essentially in the Fe_3O_4 phase was described by Zhang et al.[27]. A low alpha iron catalyst (see §1.1.1) that did not contain copper was activated with syngas and exhibited low (<20%) CO conversion during 100 hours of synthesis. Samples of this catalyst withdrawn during the first 100h were essentially in the Fe_3O_4 phase. The CO conversion after pure CO activation, following a short induction period, was over 90% and performed very stable. From this it can be concluded that the activity of the carbide phase is at least five times higher than that of the Fe_3O_4 phase.

In-situ XRD studies by Jung and Thomson[75,76] monitored similar changes in the catalyst structure during Fischer-Tropsch. The transformation from Fe_2O_3 to Fe_3O_4 at 543 K under syngas is very rapid while the subsequent transformation to χ-Fe_5C_2 is very slow and takes place via a shrinking core process (see also Figure 1.5.1). The catalytic activity appeared to be directly related to the formation of χ-Fe_5C_2 as was again shown by Ma et al. using pure χ-Fe_5C_2[77].

1.6.   Deactivation of the catalyst during Fischer-Tropsch reaction

One of the main causes for deactivation of iron based Fischer-Tropsch catalysts is the transformation of active surface carbon species and / or active iron carbide phases into inactive carbon or iron carbide forms[76,78]. Eliason and Bartholomew[79] proposed, based on an extensive kinetic study, a deactivation model involving 2 parallel pathways:

(a) conversion of atomic carbon to polymeric carbon species to graphitic carbon
(b) conversion of active carbon-rich iron carbides to inactive carbon-poor iron carbides

It was demonstrated that for K-promoted catalysts, deactivation pathway (a) was clearly prevalent, while for unpromoted catalysts both pathways (a) and (b) occurred.
More recently, Li et al.[80] suggested an alternative deactivation pathway, namely:

(c) conversion of active iron carbides into Fe_3O_4

In a study by Sault and Datye[81] on a K- and Cu-promoted (100 Fe/ 5 Cu/ 0.2 K) catalyst, the deactivation pathway (a) was confirmed to be predominant. Significant carbon deposition and some filament formation were observed after CO treatment at 280°C for 24h. However, Kalakkad et al.[82] demonstrated that for a deactivated K- and Cu-promoted catalyst iron carbides are present as well, suggesting that also pathway (b) may occur. XRD of an untreated catalyst showed it consisted entirely of Fe_2O_3 (hematite). The catalyst pretreated at 270°C exhibits the pattern of Fe_3O_4 (magnetite) and iron carbide. Both magnetite and iron carbide have diffraction lines at d-spacings of 2.10 nm, but the 100% intensity line for magnetite occurs at 1.79 nm. The ratio of the two peak areas should be around 3.33 if only magnetite was present in the sample. This ratio will decrease if there is an iron carbide phase present along with magnetite. They found a ratio of 2.12[7] and concluded that the catalyst sample exposed to CO at 270°C contained both magnetite and iron carbide phases. For the sample exposed to CO at 400°C, the peak at 1.79 nm that corresponds to magnetite has disappeared completely showing that the sample has been entirely transformed to iron carbide(s).

Concerning deactivation pathway (c), Li et al. observed, using XANES, EXAFS, and Mössbauer spectroscopy, the gradual re-oxidation of iron carbides into Fe_3O_4 with increasing time on stream. After 450h, Fe_3O_4 was the only detectable iron compound. The observed correlation between Fischer-Tropsch rates, iron carbide concentration and

the re-oxidation of the catalyst as CO conversion decreased, suggested that the deactivation may be directly related to the conversion of iron carbides into Fe_3O_4.

1.7. References

1. Iglesia, E. Design, synthesis, and use of cobalt-based Fischer-Tropsch synthesis catalysts. *Appl. Catal. A Gen.* **161,** 59–78 (1997).

2. Schulz, H. Major and minor reactions in Fischer-Tropsch synthesis on cobalt cobalt catalysts. *Top. Catal.* **26,** 73–85 (2004).

3. Elbashir, O. & Roberts, C. No Title. *Prepr. - Am. Chem. Soc., Div. Pet. Chem.- Pr. Arch. - Am. Inst. Chem. Eng.* **49,** 157 (2004).

4. Maitlis, P. M., Quyoum, R., Long, H. C. & Turner, M. L. Towards a chemical understanding of the Fischer–Tropsch reaction: alkene formation. *Appl. Catal. A Gen.* **186,** 363–374 (1999).

5. Pichler, H. Twenty-five years of synthesis of gasoline by catalytic conversion of carbon monoxide and hydrogen. *Adv. Catal. Relat. Subj.* **302,** 271 (1952).

6. Adeyiga, A. A. *Development of Attrition Resistant Iron-Based Fischer-Tropsch Catalysts*. (Grant No.: DE-FG26-99FT40619 for U.S. Department Of Energy, 2003).

7. Shroff, M. D. *et al.* Activation of precipitated iron Fischer-Tropsch synthesis catalysts. *J. Catal.* **156,** 185–207 (1995).

8. Van der Laan, G. P. *Kinetics, Selectivity and Scale Up of the Fischer-Tropsch Synthesis*. *University of Groningen* (Thesis, University of Groningen, 1999).

9. Laan, G. van der. Kinetics, selectivity and scale up of the Fischer-Tropsch synthesis. *NPT Procestechnol.* 1–251 (1999).

10. Bukur, D. B., Todic, B. & Elbashir, N. Role of water-gas-shift reaction in Fischer-Tropsch synthesis on iron catalysts: A review. *Catal. Today* **275,** 66–75 (2016).

11. Chun, D. H. *et al.* Negative Effects of CO2 in the Feed Stream on the Catalytic Performance of Precipitated Iron-Based Catalysts for Fischer-Tropsch Synthesis. *Catal. Letters* **142,** 452–459 (2012).

12. Callaghan, C. Kinetics and catalysis of the water-gas-shift reaction: A microkinetic and graph theoretic approach. (Worcester Polytechnic Institute, 2006).

13. Dry, M. E. & Hoogendoorn, J. C. Technology of the Fischer-Tropsch process. *Catal. Rev. - Sci. Eng.* **23,** 265–278 (1981).

14. Anderson, R. B. Forty years with the Fischer-Tropsch synthesis 1944-1984. *Stud. Surf. Sci. Catal.* **19,** 457–461 (1984).

15. Diffenbach, R. A. & Fauth, D. J. The role of pH in the performance of precipitated iron Fischer-Tropsch catalysts. *J. Catal.* **100,** 466–476 (1986).

16. Motjope, T. R., Dlamini, T. H., Coville, N. J. & Pollak, H. Effect of precipitating agent on the catalytic behavior of precipitated iron catalysts. *Hyperfine Interact.* **120/121,** 763–767 (1999).

17. Motjope, T. R., Dlamini, T. H., Coville, N. J. & Hearne, G. R. Application of in situ Mossbauer spectroscopy to investigate the effect of precipitating agents on precipitated iron Fischer-Tropsch catalysts. *Catal. Today* **71,** 335–341 (2002).

18. Diffenbach, R. A. & Fauth, D. J. The role of pH in the performance of precipitated iron Fischer-Tropsch catalysts. *J. Catal.* **100,** 466–476 (1986).

19. Coville, N. J. & Bromfield, T. C. The effect of sulfide ions on a precipitated iron Fischer-Tropsch catalyst. *Appl. Catal., A* **186,** 297–307 (1999).

20. Dry, M. E. Fischer-Tropsch synthesis over iron catalysts. *Catal. Lett.* **7,** 241–251 (1990).

21. Dry, M. E. in *Catal. Sci. Technol.* **1,** 159–255 (Springer-Verlag, 1981).

22. Anderson, R. B. *The Fischer-Tropsch Synthesis*. **630-08-0,** (Academic Press, 1984).

23. Ruitenbeek, M., Dugulan, A. I. & Jong, K. P. De. Effect of precursor on the catalytic performance of supported iron catalysts for the Fischer–Tropsch synthesis of lower olefins. *Catal. Today* (2013). doi:10.1016/j.cattod.2013.03.018

24. Oar-Arteta, L., Valero-Romero, M. J., Wezendonk, T., Kapteijn, F. & Gascon, J. Formulation and catalytic performance of MOF-derived Fe@C/Al composites for high temperature Fischer-Tropsch synthesis. *Catal. Sci. Technol.* **8,** 210–220 (2018).

25. Wezendonk, T. A. *et al.* Elucidating the Nature of Fe Species during Pyrolysis of the Fe-BTC MOF into Highly Active and Stable Fischer-Tropsch Catalysts. *ACS Catal.* **6,** 3236–3247 (2016).

26. Davis, B. H. Fischer-Tropsch synthesis: relationship between iron catalyst composition and process variables. *Catal. Today* **84,** 83–98 (2003).

27. Zhang, Y., Sirimanothan, N., O'Brien, R. J., Hamdeh, H. H. & Davis, B. H. Study of deactivation of iron-based Fischer-Tropsch synthesis catalysts. *Stud. Surf. Sci. Catal.* **139,** 125–132 (2001).

28. Bukur, D. B. *et al.* Activation Studies with a Precipitated Iron Catalyst for Fischer-Tropsch Synthesis. *J. Catal.* **155,** 353–365 (1995).

29. Bukur, D. B., Lang, X., Nowicki, Zl. & Manne, R. K. Activation studies with a precipitated iron catalysts for Fischer-Tropsch synthesis. II. Reaction studies. *J. Catal.* **155,** 366–375 (1995).

30. Bukur, D. B., Lang, X. & Ding, Y. Pretreatment effect studies with a precipitated iron Fischer-Tropsch catalyst in a slurry reactor. *Appl. Catal., A* **186,** 255–275 (1999).

31.   Luo, M. & Davis, B. H. Fischer-Tropsch synthesis: activation of low-alpha potassium promoted iron catalysts. *Fuel Process. Technol.* **83,** 49–65 (2003).

32.   Sudsakorn, K., Goodwin Jr., J. G. & Adeyiga, A. A. Effect of activation method on Fe FTS catalysts: investigation at the site level using SSITKA. *J. Catal.* **213,** 204–210 (2003).

33.   Ding, M. *et al.* Transformation of carbonaceous species and its influence on catalytic performance for iron-based Fischer-Tropsch synthesis catalyst. *J. Mol. Catal. A Chem.* **351,** 165–173 (2011).

34.   Amelse, J. A., Butt, J. B. & Schwartz, L. H. Carburization of supported iron synthesis catalysts. *J. Phys. Chem.* **82,** 558–563 (1978).

35.   Raupp, G. B. & Delgass, W. N. Moessbauer investigation of supported iron and iron-nickel (FeNi) catalysts. II. Carbides formed by Fischer-Tropsch synthesis. *J. Catal.* **58,** 348–360 (1979).

36.   Bian, G., Oonuki, A., Koizumi, N., Kobayashi, Y. & Yamada, M. Syngas adsorption on precipitated iron catalysts reduced by H2, syngas or CO and on those used for high-pressure FT synthesis by in situ diffuse reflectance FTIR spectroscopy. *Appl. Catal., A* **219,** 13–24 (2001).

37.   Huffman, G. P. *et al.* Activation studies with a precipitated iron catalyst for Fischer-Tropsch synthesis. I. Characterization studies. *J. Catal.* **155,** 353–365 (1995).

38.   Shroff, M. D. & Datye, A. K. The importance of passivation in the study of iron Fischer-Tropsch catalysts. *Catal. Lett.* **37,** 101–106 (1996).

39.   Hao, Q., Bai, L., Xiang, H. & Li, Y. Activation pressure studies with an iron-based catalyst for slurry Fischer-Tropsch synthesis. *J. Nat. Gas Chem.* **18,** 429–435 (2009).

40.   Li, S., Meitzner, G. D. & Iglesia, E. Structure and site evolution of iron oxide catalyst precursors during the Fischer-Tropsch synthesis. *J. Phys. Chem. B* **105,** 5743–5750 (2001).

41.   Dictor, R. A. & Bell, A. T. Fischer-Tropsch synthesis over reduced and unreduced iron oxide catalysts. *J. Catal.* **97,** 121–136 (1986).

42.   Rao, K. R. P. M. *et al.* Mössbauer Study of Iron Fischer−Tropsch Catalysts during Activation and Synthesis. *Energy & Fuels* **10,** 546–551 (1996).

43.   Raje, A. P., O'Brien, R. J. & Davis, B. H. Effect of potassium promotion on iron-based catalysts for Fischer-Tropsch synthesis. *J. Catal.* **180,** 36–43 (1998).

44.   Luo, M., O'Brien, R. J., Bao, S. & Davis, B. H. Fischer-Tropsch synthesis: induction and steady-state activity of high-alpha potassium promoted iron catalysts. *Appl. Catal., A* **239,** 111–120 (2003).

45.   Yang, Y., Xiang, H.-W., Xu, Y.-Y., Bai, L. & Li, Y.-W. Effect of potassium promoter on precipitated iron-manganese catalyst for Fischer-Tropsch synthesis. *Appl. Catal., A* **266,** 181–194 (2004).

46.   Dwyer, D. J. & Hardenbergh, J. H. Catalytic reduction of carbon monoxide over potassium modified iron surfaces.

47.   Zhang, H., Ma, H., Zhang, H., Ying, W. & Fang, D. Effects of Zr and K Promoters on Precipitated Iron-Based Catalysts for Fischer-Tropsch Synthesis. *Catal. Letters* **142,** 131–137 (2012).

48.   Zhang, C.-H. *et al.* Adsorption and reaction of CO and hydrogen on iron-based Fischer-Tropsch synthesis catalysts. *J. Mol. Catal. A Chem.* **328,** 35–43 (2010).

49.   Mao, W.-Y. *et al.* Influence of Copper Loading on the Surface Species and Catalytic Properties in the Formation of Oxygenated By-products During FTS Over FeCuKLa/SiO2 Catalysts. *Catal. Letters* **142,** 1098–1106 (2012).

50.   Bell, A. T. Fischer-Tropsch Synthesis over Reduced Iron Oxide Catalysts and Unreduced. *J. Catal.* **136,** 121–136 (1986).

51.   O'Brien, R. J. & Davis, B. H. Impact of Copper on an Alkali Promoted Iron Fischer-Tropsch Catalyst. *Catal. Lett.* **94,** 1–6 (2004).

52.   Koelbel, H. & Ralek, M. The Fischer-Tropsch synthesis in the liquid phase. *Catal. Rev. - Sci. Eng.* **21,** 225–274 (1980).

53.   O'Brien, R. J., Xu, L., Spicer, R. L. & Davis, B. H. Activation Study of Precipitated Iron Fischer-Tropsch Catalysts. *Energy & Fuels* **10,** 921–926 (1996).

54.   O'Brien, R. J. *et al.* Activity and selectivity of precipitated iron Fischer-Tropsch catalysts. *Catal. Today* **36,** 325–334 (1997).

55.   Ngantsoue-Hoc, W., Luo, M., Zhang, Y., O'Brien, R. J. & Davis, B. H. Fischer-Tropsch synthesis: activity and selectivity for Group I alkali promoted iron-based catalysts. *Appl. Catal., A* **236,** 77–89 (2002).

56.   Li, J., Cheng, X., Zhang, C., Yang, Y. & Li, Y. Effects of alkali on iron-based catalysts for Fischer-Tropsch synthesis: CO chemisorptions study. *J. Mol. Catal. A Chem.* **396,** 174–180 (2015).

57.   Li, J. *et al.* Alkalis in iron-based Fischer-Tropsch synthesis catalysts: distribution, migration and promotion. *J. Chem. Technol. Biotechnol.* Ahead of Print (2017). doi:10.1002/jctb.5152

58.   Li, J. *et al.* Effect of alkalis on iron-based Fischer-Tropsch synthesis catalysts: Alkali-FeOx interaction, reduction, and catalytic performance. *Appl. Catal. A Gen.* **528,** 131–141 (2016).

59.   Luo, M. & Davis, B. H. Fischer-Tropsch synthesis: Group II alkali-earth metal promoted catalysts. *Appl. Catal., A* **246,** 171–181 (2003).

60. Park, M. *et al.* Studies on nanosized iron based modified catalyst for Fischer-Tropsch synthesis application. *J. Nanosci. Nanotechnol.* **11,** 1447–1450 (2011).

61. Dlamini, H., Motjope, T. R., Joorst, G., ter Stege, G. & Mdleleni, M. Changes in Physico-Chemical Properties of Iron-Based Fischer–Tropsch Catalyst Induced by SiO2 Addition. *Catal. Lett.* **78,** 201–207 (2002).

62. Yang, Y. *et al.* Structure and Fischer–Tropsch performance of iron–manganese catalyst incorporated with SiO. *Appl. Catal., A* **284,** 105–122 (2005).

63. Mogorosi, R. P., Fischer, N., Claeys, M. & van Eric., S. Strong-metal-support interaction by molecular design: Fe-silicate interactions in Fischer-Tropsch catalysts. *J. Catal.* **289,** 140–150 (2012).

64. Jager, B. & Espinoza, R. L. Advances in low temperature Fischer-Tropsch synthesis. *Catal. Today* **23,** 17–28 (1995).

65. Milburn, D. R., Chary, K. V. R. & Davis, B. H. Promoted iron Fischer-Tropsch catalysts: characterization by nitrogen sorption. *Appl. Catal., A* **144,** 121–132 (1996).

66. Milburn, D. R., Chary, K. V. R., O'Brien, R. J. & Davis, B. H. Promoted iron Fischer-Tropsch catalysts: characterization by thermal analysis. *Appl. Catal., A* **144,** 133–146 (1996).

67. O'Brien, R. J., Xu, L., Raje, A. P., Bao, S. & Davis, B. H. Activity, selectivity and attrition characteristics of supported iron Fischer-Tropsch catalysts. *Appl. Catal., A* **196,** 173–178 (2000).

68. Pham, H. N., Viergutz, A., Gormley, R. J. & Datye, A. K. Improving the attrition resistance of slurry phase heterogeneous catalysts. *Powder Technol.* **110,** 196–203 (2000).

69. Zhao, R., Goodwin, J. G., Jothimurugesan, K., Gangwal, S. K. & Spivey, J. J. Spray-Dried Iron Fischer−Tropsch Catalysts. 1. Effect of Structure on the Attrition Resistance of the Catalysts in the Calcined State. *Ind. Eng. Chem. Res.* **40,** 1065–1075 (2001).

70. Sudsakorn, K., Goodwin, J. G., Jothimurugesan, K. & Adeyiga, A. a. Preparation of Attrition-Resistant Spray-Dried Fe Fischer−Tropsch Catalysts Using Precipitated SiO 2. *Ind. Eng. Chem. Res.* **40,** 4778–4784 (2001).

71. Bukur, D. B. *et al.* Binder/support effects on the activity and selectivity of iron catalysts in the Fischer-Tropsch synthesis. *Ind. Eng. Chem. Res.* **29,** 1588–1599 (1990).

72. Satterfield, C. N., Hanlon, R. T., Tung, S. E., Zou, Z. M. & Papaefthymiou, G. C. Initial behavior of a reduced fused-magnetite catalyst in the Fischer-Tropsch synthesis. *Ind. Eng. Chem. Prod. Res. Dev.* **25,** 401–407 (1986).

73. O'Brien, R. J. *et al.* Fischer-Tropsch synthesis: impact of potassium and zirconium promoters on the activity and structure of an ultrafine iron oxide catalyst. *Top. Catal.* **2,** 1–15 (1995).

74.   Li, S., Ding, W., Meitzner, G. D. & Iglesia, E. Spectroscopic and Transient Kinetic Studies of Site Requirements in Iron-Catalyzed Fischer-Tropsch Synthesis. *J. Phys. Chem. B* **106,** 85–91 (2002).

75.   Jung, H. & Thomson, W. J. Dynamic x-ray diffraction study of an unreduced iron oxide catalyst in Fischer-Tropsch synthesis. *J. Catal.* **139,** 375–382 (1993).

76.   Jung, H. & Thomson, W. J. Dynamic x-ray diffraction study of an unsupported iron catalyst in Fischer-Tropsch synthesis. *J. Catal.* **134,** 654–667 (1992).

77.   Ma, D. Insight into iron-based Fischer-Tropsch synthesis reaction. in *Abstracts of Papers, 251st ACS National Meeting & Exposition, San Diego, CA, United States, March 13-17, 2016* CATL-446 (American Chemical Society, 2016).

78.   Dwyer, D. J. & Hardenbergh, J. H. The catalytic reduction of carbon monoxide over iron surfaces: a surface science investigation. *J. Catal.* **87,** 66–76 (1984).

79.   Eliason, S. A. & Bartholomew, C. H. Reaction and deactivation kinetics for Fischer-Tropsch synthesis on unpromoted and potassium-promoted iron catalysts. *Appl. Catal., A* **186,** 229–243 (1999).

80.   Li, S. *et al.* Structural analysis of unpromoted Fe-based Fischer-Tropsch catalysts using X-ray absorption spectroscopy. *Appl. Catal., A* **219,** 215–222 (2001).

81.   Sault, A. G. & Datye, A. K. An auger electron spectroscopy study of the activation of iron Fischer-Tropsch catalysts. *J. Catal.* 136–149 (1993).

82.   Kalakkad, D. S., Shroff, M. D., Kohler, S., Jackson, N. B. & Datye, A. K. Attrition of precipitated iron Fischer-Tropsch catalysts. *Appl. Catal., A* **133,** 335–350 (1995).

CHAPTER 1

2

Effects of re-oxidation

In this chapter we report a model study in which exposure to air is prevented completely by performing both XRD and TEM-EELS in quasi in-situ mode. We found that, starting from hematite precursors, carburized catalysts contain mainly iron carbide of as yet unknown structure and some magnetite. The latter is not covered with amorphous carbon, whereas the carbide is. Overall, carburized catalysts change significantly upon (controlled or uncontrolled) air exposure.

During re-oxidation carbon is freed and deposited as a separate amorphous phase. From these results it is clear that, when studying iron-based Fischer-Tropsch catalysts, exposure to air should be avoided completely.

2.1. <u>Introduction</u>

Although assumed to be iron carbide, the active phase of iron-based Fischer-Tropsch catalysts remains unresolved. An important issue is the air-sensitivity of the active catalysts. Here we report a model study using both XRD and TEM-EELS in which exposure to air is completely prevented. The work has been conducted on iron-based Fischer-Tropsh catalysts that were prepared by precipitation since this typically renders the best catalytic performance[2–6]. Also different promoters like copper and potassium were added to enhance the catalytic activity even further[7–16].

As the activation step takes place inside the reactor (in-situ at high temperature and pressure), studying this activation process is not trivial. As a result, the identity of the real active phase is still unknown. It is believed that iron carbides are the key components, being 5 times more active than iron oxides[17,18]. Free carbon is thought to play an essential part in the catalytic process[19–22]. It was also suggested that part of this carbon could have been formed by air exposure during sample handling prior to analysis[23].

It is known that many published ex-situ characterization studies are not representative for the real catalyst[24], since the samples are sensitive to air exposure. During contact with ambient air, the catalyst is oxidized extensively and no information can be obtained anymore on the actual working catalyst. It was suggested that the best one can do is to perform a passivation, which is to expose the specimen to air under controlled conditions in order to prevent excessive oxidation. This method has been used in detailed TEM-EELS characterization studies[23,25,26]. Nevertheless, any oxidation (controlled or not) inevitably changes the active state of the catalyst surface under study.

To overcome this problem, (quasi) in-situ measurements should be performed, preventing exposure to air. This has been done extensively using X-Ray Diffraction (XRD) and Mössbauer spectroscopy[17,27–29]. However, these bulk techniques lack spatial resolution and do not necessarily give information on the catalyst surface (which is where the catalytic reactions take place). Recently, a study using in situ transmission X-ray microscopy showed a large improvement in this respect, achieving a spatial resolution of several tens of nm[30]. A technique that provides very high spatial resolutions (in the nm range) is HRTEM or STEM in combination with EELS[31]. However, the activated or used catalysts have to be transferred to the electron microscope without exposure to air.

In our model study, samples are mounted on a gold-palladium microgrid supported on a gold grid[32], all in an Ar glove box. Samples are transferred to the microscope in a special protective atmosphere transfer sample holder under exclusion of air[33]. Once the closed holder is inside the microscope, it is opened again and the sample can be studied. Using this equipment, no passivation is required and the catalyst surface can be studied without having been exposed to air.

We study carburized iron catalysts using quasi in-situ XRD, TEM and EELS. We report the effects of both controlled passivation and uncontrolled exposure to air. Note that our carburized samples represent catalysts after CO activation at atmospheric pressure only. Depending on reaction conditions, the catalyst is again prone to changes during prolonged FT reaction[10].

2.2.   Experimental

2.2.1.   Catalyst preparation

A first sample was prepared by precipitating iron nitrate with ammonia. While stirring at 70°C, 11.2 kg 4N ammonia was added to a solution of 5.06 kg $Fe(NO_3)_3 \cdot 9H_2O$ and 14.6 kg water until the pH reached 7.4. After filtration and subsequent washing with demineralized water, a 5 wt% slurry was prepared by adding additional water. To this slurry, K_2CO_3 and $Cu(NO_3)_2 \cdot 3H_2O$ were added to obtain a final catalyst loading of 0.8 wt % K_2O and 0.8wt% CuO. The slurry was spray-dried using a conventional spray-drier (Type Niro SD-6.3-R equipped with a Niro FU11 rotary atomizer). Settings: rotary speed = 12600 rpm, inlet temperature = 400°C, outlet temperature = 140°C. Calcination was performed using a Carbolite HTR 11/150 rotary furnace (ramp = 2°/min, final temperature = 300°C, dwell time = 4 hours).

A second sample was prepared in a similar way with the exception that no potassium or copper were added before spray-drying. Instead, the equivalent of 0.8wt% K_2O and 0.8wt % CuO were added after spray-drying via a two-step incipient wetness impregnation using a solution of K_2CO_3 and $Cu(NO_3)_2 \cdot 3H_2O$ respectively. Each impregnation was followed by a drying and calcination step as described above.

A hematite reference was prepared by calcining the spray-dried intermediate twice at 1000°C (ramp = 5°/min, dwell = 10 hours), cooling to room temperature after each calcination step.

2.2.2. Carburization experiments

Catalyst activation was mimicked using a specially designed set-up consisting of a calibrated flow meter, quartz U-tube, and an oven (see 2.2.1). 350 mg Iron oxide catalyst precursor was sandwiched in between quartz-wool at the bottom of the U-tube.
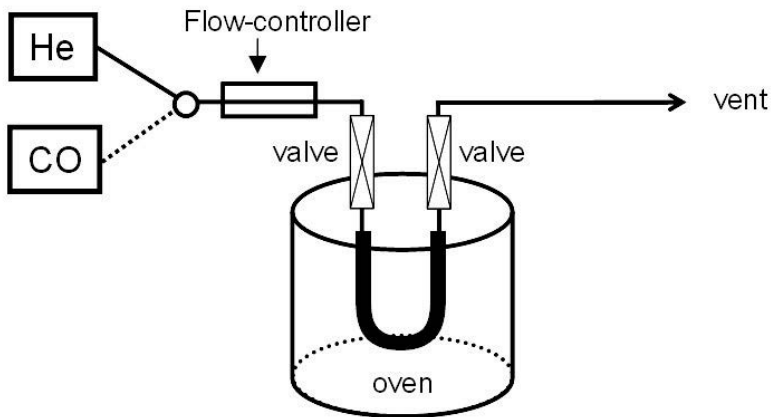
Figure 2.2.1: Schematic representation of the carburization set-up

The carburization procedure was performed at atmospheric pressure:
- 2 °C / min to 150°C in helium (10 ml/min)
- Switch to carbon monoxide (5 ml/min)
- 2°C / min to 270 °C
- dwell for 24 hours
- switch to helium (10 ml/min)
- cool down to room temperature

The U-tube was closed and the sample was transferred to a glove-box.

2.2.3. Small scale oxidation / passivation experiments

The effects of oxidation were investigated using two different methods:

1. An uncontrolled exposure to air by simply taking out the TEM holder from the microscope after studying the carburized samples. After two minutes of exposure, the TEM holder was reinserted into the microscope.

2. A controlled exposure to air (passivation) as indicated by Shroff et al.[24]. We used a vacuum chamber into which we could insert the (closed) protective atmosphere transfer TEM holder (see Figure 2.2.2). By lowering the pressure to 40 mbar using a turbo pump, an atmosphere of 0.8 % O_2 was created. The TEM holder was opened once the chamber pressure was stable. The samples were then exposed for 30 minutes at room temperature. Note that we closed the holder again during transport back to the TEM, so the only exposure to oxygen was inside the passivation set-up.

By performing these treatments on the catalyst dispersed on the TEM grid, we were able to study exactly the same areas of the samples before and after oxidation.
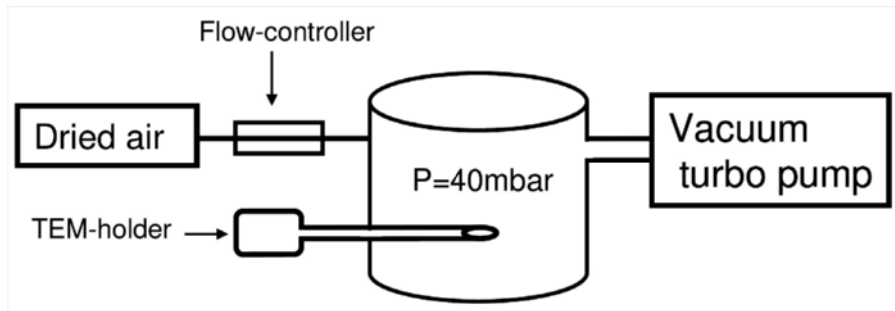
Figure 2.2.2: Schematic representation of the passivation set-up

2.2.4. X-Ray Diffraction (XRD)

XRD was performed using a Bruker D8 diffractometer equipped with a Cu Kα source. Variable (θ-compensating) anti-scatter and divergence slits were used. Rietveld refinement was performed using the GSAS software package[34].

The carburized samples were measured quasi in-situ under nitrogen using a special dome (Bruker AB100B36). Unfortunately, the subsequent passivation of these samples proceeded in a less controlled manner than originally planned. However, as TEM-EELS analysis of these samples shows similar results compared to other properly passivated samples we consider these samples as passivated properly.

2.2.5. TEM-EELS

The samples were examined using a FEI Tecnai F20 TEM equipped with a Field Emission Gun (FEG), a Gatan 4k x 4k ultrascan camera and a Gatan Image Filter (GIF), operated at 200 kV. The EELS edges were quantified by integration of the peak areas as described by Mitchell[35]. We used the peak areas to determine the valence states of the iron species and to calculate iron/oxygen ratios, which is a semi-quantitative way to determine the relative degrees of oxidation. From Fourier Transforms using Digital Micrograph 3.1™, we were able to determine lattice spacings. Special carbon-free TEM grids were used to minimize interference[32]. Details on the preparation of these grids can be found in Chapter 6.

2.3. Results and discussion

2.3.1. The oxidic catalyst precursors

XRD results of the calcined oxidic precursors prove that hematite (Fe_2O_3) is the main crystalline phase present (see Figure 2.3.1).
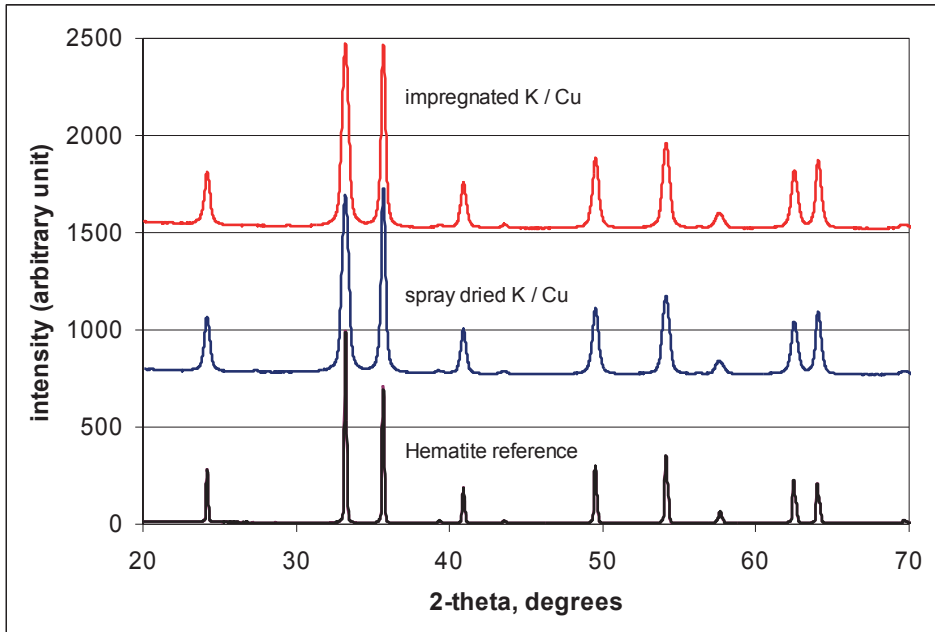
Figure 2.3.1: XRD patterns of the oxidic precursors compared to a Hematite reference

TEM images show spherical / elliptical crystallites with sizes of about 5 to 50 nm. At higher magnification lattice spacings can be observed, consistent with the d-spacings of hematite [Figure 2.3.2; JCPDS#33664].
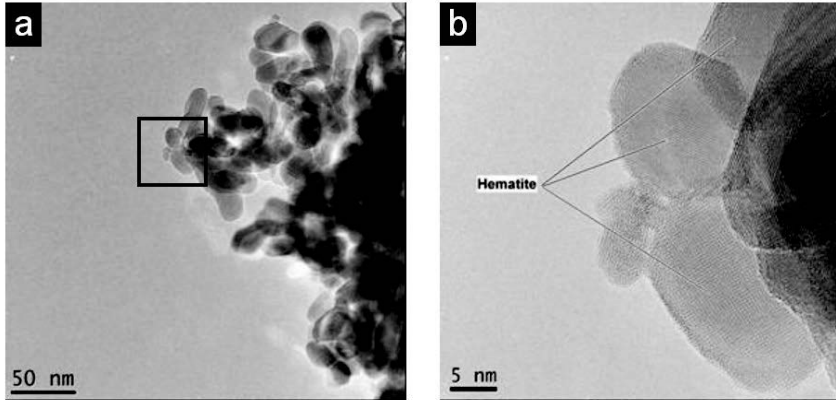
Figure 2.3.2: TEM micrographs of the spray dried sample showing the precursor morphology (a) and lattice spacings at higher magnification (b)

By calculating the L_3/L_2 ratios (area/area) from EELS data (Figure 2.3.3), the oxidation state of the iron can be determined[25]. We found L_3/L_2 ratios of 5.7, 5.8 and 5.4 for both samples and the hematite reference, respectively. This proves the iron in all samples is Fe(III), consistent with the hematite structure.
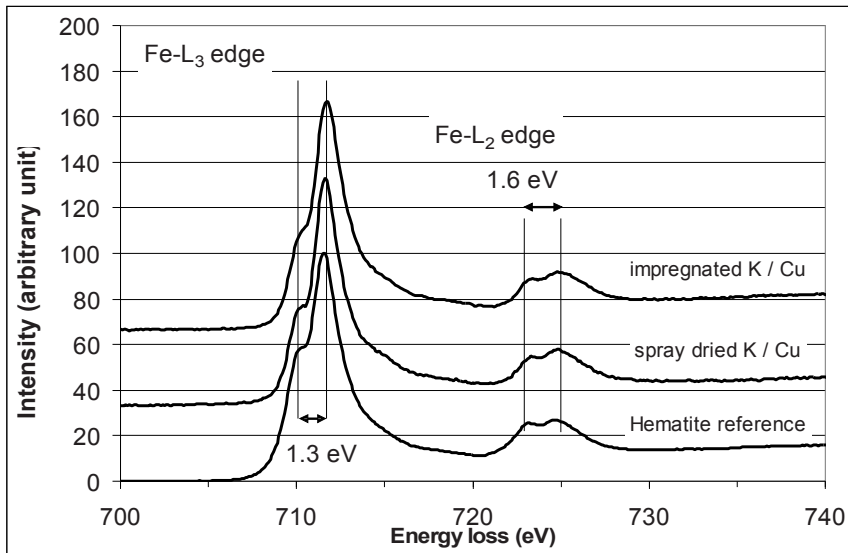
Figure 2.3.3: EELS data of the catalyst precursors compared to a hematite reference

2.3.2. The carburized samples

A typical XRD pattern of a carburized sample is shown in Figure 2.3.4 (black line), together with a scan of the sample after exposure to oxygen (gray line). No hematite is found anymore. Magnetite (Fe_3O_4) is clearly present in both samples, albeit as a minor phase. The scan is dominated by signals from a poorly crystalline iron carbide phase characterized by diffraction lines at 39.2°, 41.0°, 43.5°, 46.8°, 58.5° and 67.7°2θ (d-spacings of 2.30Å, 2.20Å, 2.08Å, 1.94Å, 1.58Å and 1.38Å, respectively). Upon oxidation this phase decreases in intensity, while the background is enhanced by a substantial amount of amorphous halo.
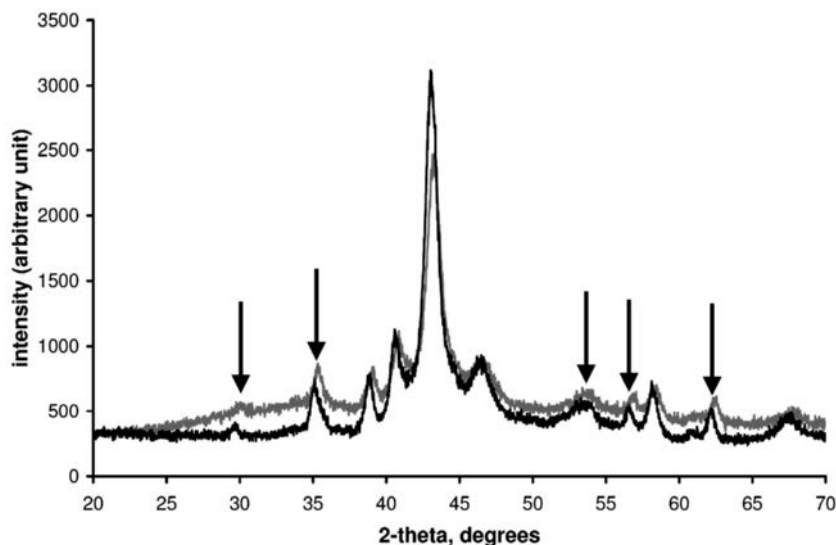
Figure 2.3.4: Powder XRD patterns after carburization (black line) and passivation (gray line) of the spray dried catalyst. Arrows indicate diffraction lines due to magnetite.

Crystal structures are known for ε'-$Fe_{2.2}C$, χ-Fe_5C_2, ε-Fe_3C and Fe_7C_3[36], η-Fe_2C[37], θ-Fe_3C[38] and Fe_4C[39]. However, none of these structures yields a simulated pattern corresponding completely to the XRD pattern obtained here. Datye et al. published a pattern that appears to be similar to our data[40], explaining the differences as due to severely faulted χ-Fe_5C_2. Likewise, Jin[41] provides powder XRD patterns of iron carbides in which this phase appears to be present (among other phases). He, too, suggests the

signal is due to χ-Fe$_5$C$_2$. In our case Rietveld refinement, using magnetite and χ-Fe$_5$C$_2$ as phases for the simulation, could not give a satisfactory match at all. An unrealistic shape of the fitted background is obtained due to several intense lines of χ-Fe$_5$C$_2$ inevitably becoming very broad to match the observed scan, which is necessarily compensated for by the fitted background as shown in Figure 2.3.5.
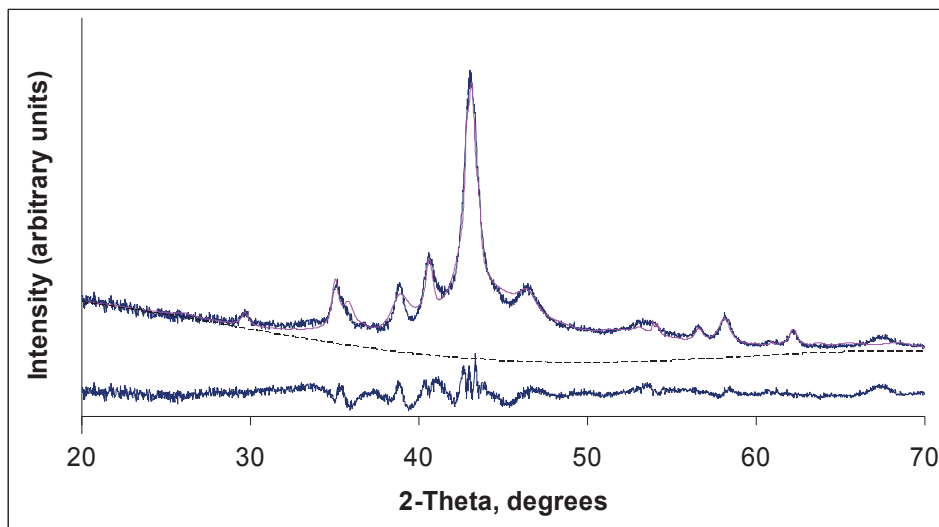
Figure 2.3.5: *Rietveld refinement of the powder XRD scan from figure 2.3.4.*

Different iron carbides can be formed with varying iron to carbon ratios[42,43], their formation depending on both the nature of the catalyst as well as the reaction conditions[19]. Based on the data we have available, no conclusions can be drawn about the structure we obtained under our (atmospheric pressure) activation condition.

Typical TEM images of the carburized samples are shown in Figure 2.3.6. Note that the specimens were carefully transported under inert to avoid oxidation. In addition we adapted methods to ensure no external contaminations (including carbon pick-up from the air) could occur[32]. The morphology of the oxidic precursor changed completely upon carburization. The spherical / elliptical crystallites become much more irregularly shaped and different crystalline phases are observed. Also, small amounts of graphitic and amorphous carbon are detected. By performing Fourier Transforms of the crystalline areas we are able to distinguish between iron oxide and iron carbide species. The areas

used for these calculations are indicated I-V in each image; the results are shown Table 1.

Spacings around 2.1Å cannot unambiguously be assigned to magnetite (2.10Å) or iron carbide (2.08Å). In some cases, spacings between 3.9 and 4.1 Å are found which we cannot yet assign to a specific phase. A detailed electron diffraction study will be undertaken in the near future to identify this unknown phase. EELS data (not shown) confirm the XRD findings. The L_3/L_2 ratios (area/area) decrease from about 5.8 to 2.9, showing the iron species to be reduced to either metallic iron or iron carbides.
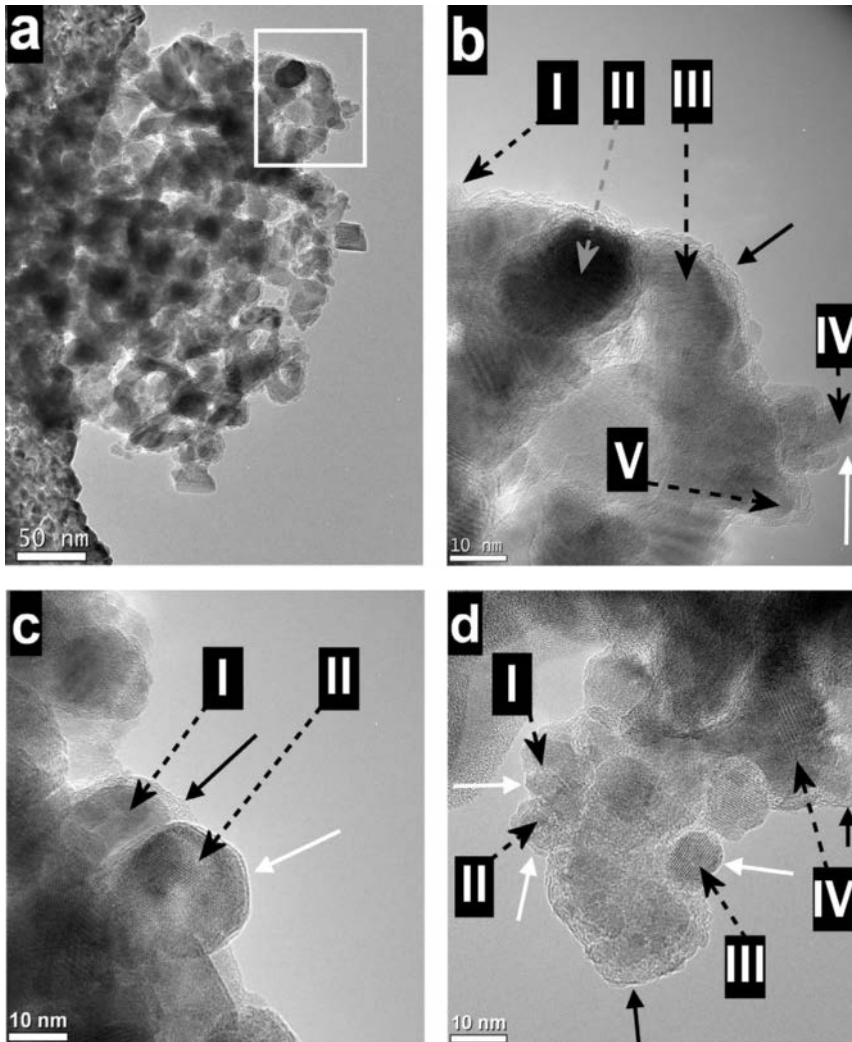
Figure 2.3.6: TEM images of carburized samples; a-c are the 'spray dried catalyst'; d is the impregnated catalyst. The area highlighted in a is magnified in b. The white arrows show the clean iron oxide surface; the black arrows show carbon layers. The dotted arrows indicate the areas used for FFT analysis.

Figure	Area	spacing (Å)	corresponding °2 theta	assignment	carbon layer present
a	I	2.50	35.3	magnetite	No
	II	2.33	38.0	iron carbide	Yes
	II	2.27	39.0	iron carbide	Yes
	II	2.36	37.5	iron carbide	Yes
	III	2.05	43.2	iron carbide / m	Yes
	III	2.06	42.8	iron carbide / m	Yes
	III	1.97	44.8	iron carbide	Yes
	III	3.94	22.5	unknown	Yes
	IV	2.94	30.1	magnetite	No
	V	2.06	42.9	magnetite / iron	Yes
	V	1.96	45.0	iron carbide	Yes
	V	2.09	42.3	iron carbide / m	Yes
c	I	2.13	41.4	magnetite / iron	Yes
	I	2.48	35.7	magnetite	Yes
	I	2.21	40.0	iron carbide	Yes
	I	1.91	46.3	iron carbide	Yes
	I	2.13	41.4	magnetite / iron	Yes
	II	2.13	41.5	magnetite / iron	No
	II	3.98	22.2	unknown	No
	II	2.44	36.2	magnetite	No
	II	2.80	31.5	magnetite	No
	II	2.47	35.8	magnetite	No
	II	4.12	21.5	unknown	No
d	I	2.44	36.2	magnetite	No
	II	2.87	30.8	magnetite	No
	III	2.95	30.0	magnetite	No
	III	2.52	35.1	magnetite	No
	III	2.06	42.9	magnetite	No
	III	2.47	35.8	magnetite	No
	III	4.83	18.3	unknown	No
	IV	1.90	46.5	iron carbide	Yes
	IV	2.15	41.0	iron carbide	Yes
	IV	2.14	41.2	iron carbide	Yes
	V	2.58	34.3	magnetite	Yes
	V	2.50	35.3	magnetite	Yes
	V	1.94	45.6	iron carbide	Yes
	V	1.96	45.1	iron carbide	Yes
	V	4.09	21.6	unknown	Yes

Table 1: FFT results and phase assignments as indicated in Figure 2.3.6.

Different carbon layers are highlighted with black arrows in Figure 2.3.6b-d. The white arrows show the magnetite crystallites without any carbon layers. Our data show that amorphous carbon is present after the carburization but that these deposits reside on the carbide phases and not on the magnetite. This is consistent with the work of Shroff et al.[44] although no explanation was given at the time. Bukur et al.[45] assumed a Boudouard

reaction is responsible for the carbon deposits while, more recently, Jin et al.[25] suggested that an excess of carbon from the iron-carbide phases can precipitate on the particle surface during cooling of the sample prior to analyses. In other words, the carbon layers may not even be present under reaction conditions.

Overall, the exact mechanism is still unclear. In an attempt to elucidate this issue, we performed in-situ TEM-EELS carburization studies (see Chapter 4).

2.3.3. Uncontrolled oxidation

In 1996, Shroff published a paper entitled *'The importance of passivation in the study of iron Fischer-Tropsch catalysts'[24]*. It stated that uncontrolled exposure of activated iron-based FT catalysts to air should be avoided. Subsequently, several other research groups have adapted passivation procedures, such as Mansker et al.[46]. Our data confirm the detrimental effect of uncontrolled exposure to air, although we observe similar detrimental phenomena after passivation (vide infra). We transferred a carburized catalyst under inert as explained in section 2.2.3 (Figure 2.3.7a). Following detailed TEM-EELS study, this catalyst was exposed to oxidation in an uncontrolled manner while present on the TEM grid (Figure 2.3.7b). The data (of the same area of the catalyst) show that the morphology changed completely. Many crystallites disappear after exposure to air and regroup into completely different particles, indicating that the oxidation is not limited to a surface layer.
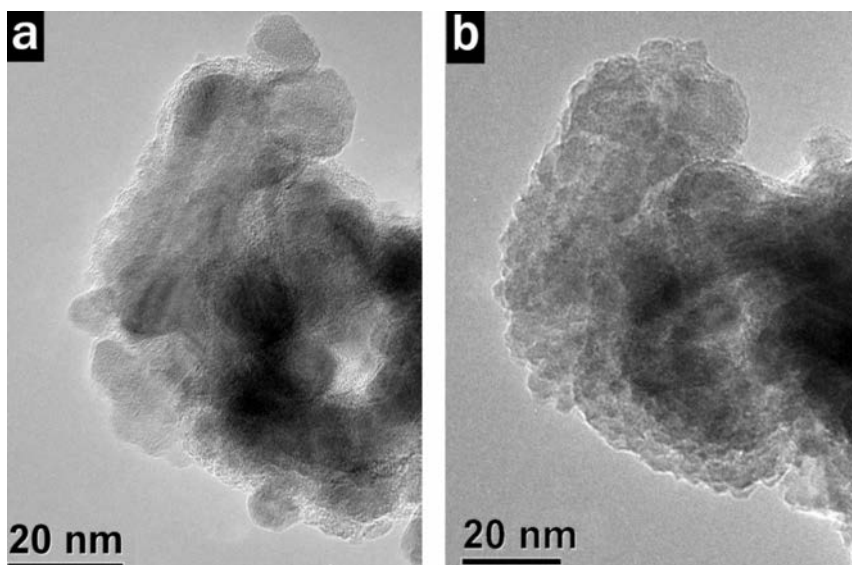
Figure 2.3.7: TEM images of the same area showing the carburized 'spray dried' sample before (a) and after (b) uncontrolled oxidation.

EELS data of the same area are presented in Figure 2.3.8. The edge intensities are normalized to the total iron edge area, allowing quantitative comparison. Figure 2.3.8a shows that the iron L_3/L_2 ratio (area/area) increased from 2.9 to 3.8; in Figure 2.3.8b the Fe/O ratio (area/area) decreased from 11.3 to 7.2. Both observations prove the sample has been oxidized.
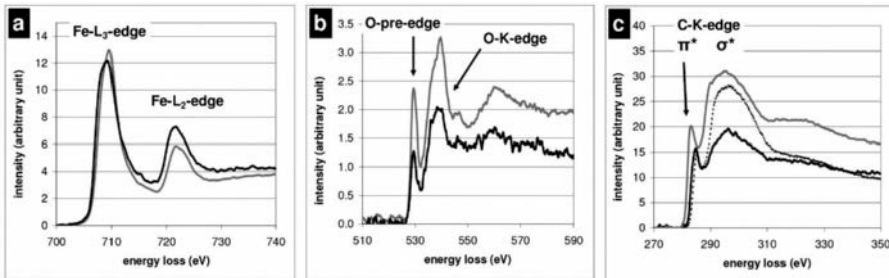
Figure 2.3.8: EEL spectra showing the iron, oxygen and carbon edges before (black) and after (gray) uncontrolled oxidation. 'c' also shows an amorphous carbon reference (dotted line; for illustrative purposes only)

The carbon K-edges (Figure 2.3.8c) show a change in the π^* to σ^* ratio after oxidation. The higher σ^* peak indicates a more amorphous character, similar to the amorphous carbon reference. The increase in total peak area after exposure to air suggests that the relative amount of carbon has increased. This increase is caused by mobile carbon species liberated from all over the sample, migrating to the area under observation and decomposing there under the electron beam, forming amorphous carbon. Although the exact nature of the mobile carbon species is unclear, this effect is consistent for all re-oxidized samples described in this paper (including the passivated ones). Due to the instability of the samples after exposure to air, accurate measurements become increasingly difficult. Since the species are mobile and decompose under the electron beam, the carbon build-up during the TEM-EELS measurements is considerable as shown in Figure 2.3.9.
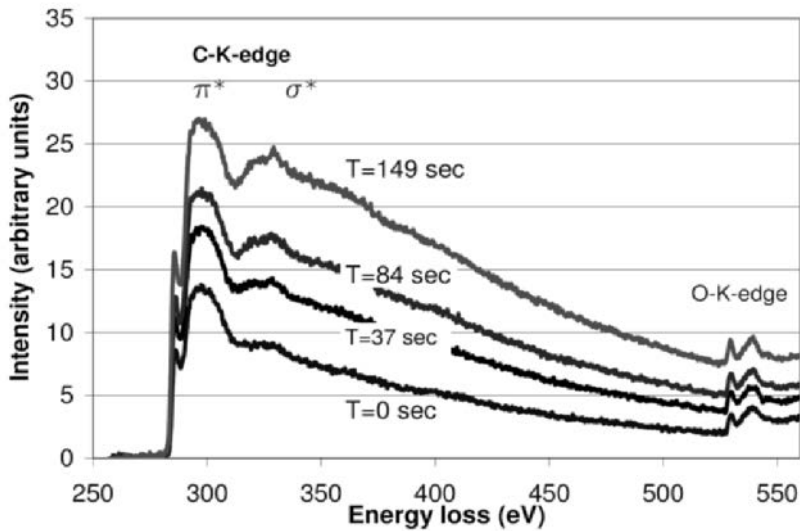
Figure 2.3.9: Effect of carbon accumulation in time

We confirmed that the TEM grids themselves show no contamination at all even after prolonged exposure to ambient air[32], making it highly unlikely that this contamination is introduced by adsorption of hydrocarbons during air exposure. To exclude other side effects, we also measured areas that had not been exposed to the electron beam prior to exposure to air, obtaining identical results . In other words, the carbon build-up we observed is not induced by the electron beam before air exposure. Therefore, these mobile carbon species are formed during exposure to air. The carbon is liberated from the iron-carbon species as was proposed by Graham et al.[23] The exact nature of these mobile carbon species is not yet known but will be studied in more detail.

2.3.4. The effect of passivation

As explained previously, iron oxide particles are still observed in carburized samples, without any carbon layers present at their surface. Passivation induces changes, although the effects are more subtle than after uncontrolled exposure to air. Apart from an overall thickening of the carbon layers that were already present before exposure, all iron oxide particles are now also covered with carbon layers (compare Figure 2.3.10a with b and c with d). This is especially clear at higher magnification as shown in Figure 2.3.10a-b and Table 1 (summarizing the corresponding FFT results).
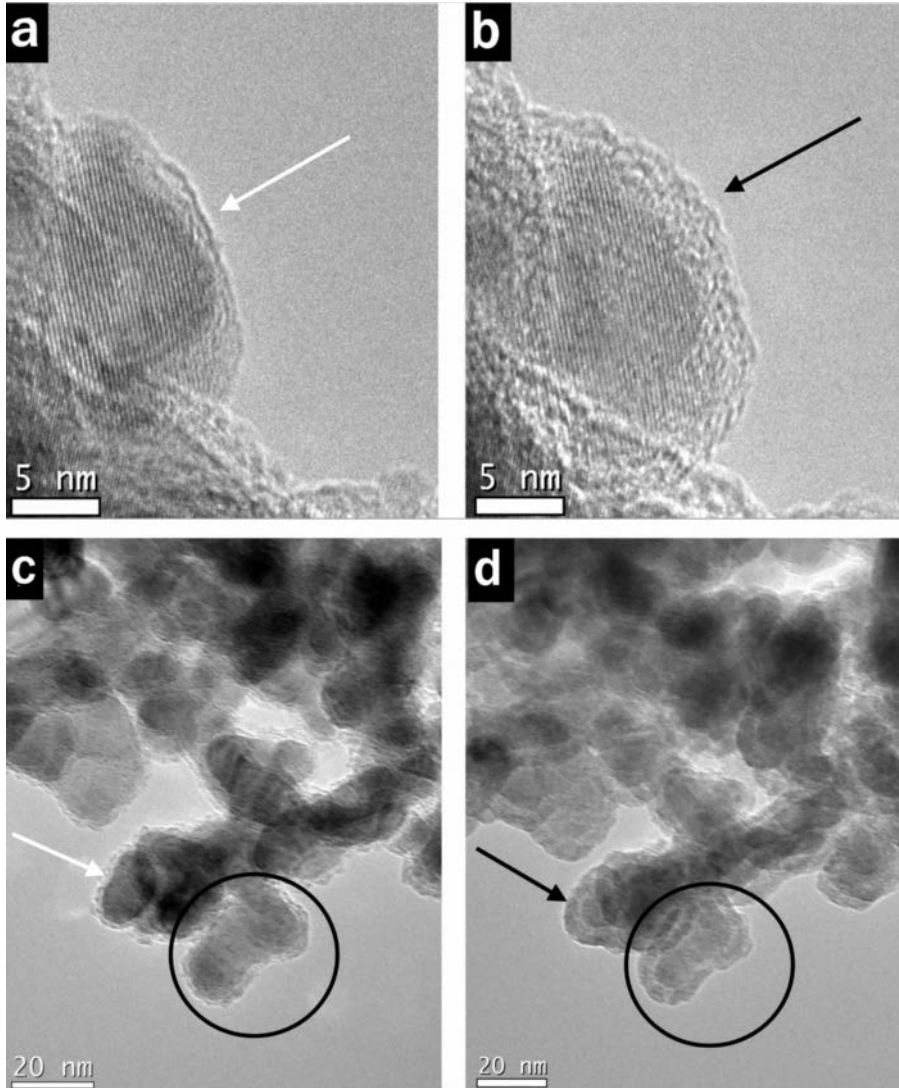
Figure 2.3.10: TEM images before (a, c; spray dried and impregnated respectively) and after passivation (b, d). Changes are indicated with white and black arrows before and after passivation respectively

EELS data show the carbides have been oxidized after passivation. Figure 2.3.11a-c show the iron-, oxygen- and carbon edges of the particle indicated by a circle in Figure 2.3.10c-d. The L_3/L_2 ratio (area/area) of the iron edge has increased from 2.6 to 4.3 after passivation. In addition, the Fe / O ratio (area/area) changed from 11.7 to 0.6. Before passivation, the carbon K-edge (Figure 2.3.11c; black line) shows a relatively high π^*-line compared to the σ^*-line. This is a confirmation of the carbidic character. The

shape of the edge suggests that some graphitic carbon might be present as well. This effect has been described before[25]. After passivation, the amount of carbon has increased considerably as explained before. Mobile carbon is liberated from the iron carbide phase and the crystallinity of the carbon decreases.
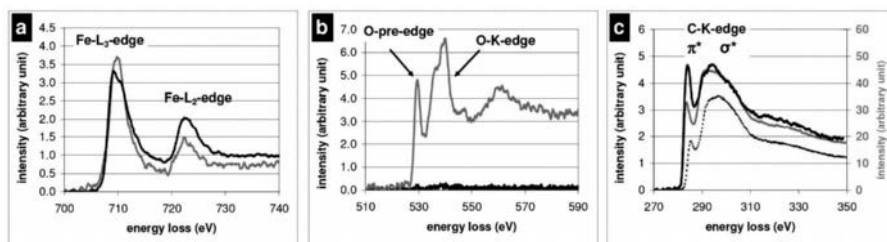
Figure 2.3.11: EEL spectra showing the iron, oxygen and carbon edges before (black) and after passivation (gray). 6c also shows an amorphous carbon reference (dotted line; for illustrative purposes only)

Amorphous deposits on the iron species have been described extensively. It is undisputed that such layers can be formed during carburization[44,45,47] but also during the Fischer-Tropsch synthesis (related to deactivation)[19].

However, Graham et al.[23] stated that passivation of iron carbide could also result in the deposition of carbon if the only reaction with oxygen was to produce Fe_3O_4 and Fe_2O_3. In other words, they suggest the layered carbon that is found on iron carbides as well as iron oxides might partially be an artifact of exposure to air. Our data confirm these suggestions.

Our findings agree with those of Shroff et al.[44], who found that carbide particles were covered with a surface film of carbon while the magnetite surface was clean. He found that these surface films are formed during a Fischer-Tropsch reaction. However, we observed these carbon layers already directly after the CO activation procedure so without the need to passivate or perform any Fischer-Tropsch reaction. This contradiction might be explained by the much shorter activation times applied by Shroff; viz. 2 hours compared to 24 hours for our samples. In fact, Shroff hardly found any carbide formation after 2 hours of CO activation. It seems likely that the catalyst was still being carburized while exposed to a syngas mixture, and the carbon deposits were formed via the Boudouard reaction.

Note that we see a substantial increase in carbon layer thickness after passivation. It is difficult to ascertain the exact catalyst surface from published data obtained for samples that have been exposed to air.

2.4.   Conclusions

Carburization of iron Fischer-Tropsch catalysts in CO yields a mixture of different phases. XRD and TEM-EELS show the precursor hematite is reduced to magnetite and iron carbide. The reduction of iron is clearly seen from the lower L_3/L_2 edge ratio (about 3.0 for iron carbide compared to 5.4 for hematite and magnetite). XRD shows mainly iron carbide with an unknown structure to be present next to magnetite. TEM results show that after carburization carbon layers are present but reside predominantly on iron-carbide species and not on iron oxide species.

Exposure to air leads to re-oxidation of the iron carbides. This is evident from the increase in EELS L_3/L_2 iron edge ratios and the decrease of the total iron to oxygen ratio. After exposure to air, the iron oxide species are covered in amorphous carbon. We believe that during re-oxidation, carbon is liberated from its solid solution in iron or iron carbide and deposited as a separate amorphous phase. Additional research is required to determine the exact nature of these mobile carbon species. Nevertheless, our data show that the carbon surface layers can change, or even form, during exposure to air. Overall, activated iron-based Fischer-Tropsch catalysts are very air-sensitive. Even after careful passivation the catalyst surface changes significantly and does not represent the actual catalyst surface anymore. When studying these catalysts, any exposure to air should be avoided.

2.5.   References

1.   Janbroers, S., Zandbergen, H. W., Louwen, J. N. & Kooyman, P. J. Insights into the nature of iron-based Fischer–Tropsch catalysts from quasi in situ TEM-EELS and XRD. *J. Catal.* **268,** 235–242 (2009).

2.   Dry, M. E. & Hoogendoorn, J. C. Technology of the Fischer-Tropsch process. *Catal. Rev. - Sci. Eng.* **23,** 265–278 (1981).

3.   Anderson, R. B. Forty years with the Fischer-Tropsch synthesis 1944-1984. *Stud. Surf. Sci. Catal.* **19,** 457–461 (1984).

4.   Diffenbach, R. A. & Fauth, D. J. The role of pH in the performance of precipitated iron Fischer-Tropsch catalysts. *J. Catal.* **100,** 466–476 (1986).

5.   Motjope, T. R., Dlamini, T. H., Coville, N. J. & Pollak, H. Effect of precipitating agent on the catalytic behavior of precipitated iron catalysts. *Hyperfine Interact.* **120/121,** 763–767 (1999).

6. Motjope, T. R., Dlamini, T. H., Coville, N. J. & Hearne, G. R. Application of in situ Mossbauer spectroscopy to investigate the effect of precipitating agents on precipitated iron Fischer-Tropsch catalysts. *Catal. Today* **71,** 335–341 (2002).

7. Dry, M. E. in *Catal. Sci. Technol.* **1,** 159–255 (Springer-Verlag, 1981).

8. Li, S., Meitzner, G. D. & Iglesia, E. Structure and site evolution of iron oxide catalyst precursors during the Fischer-Tropsch synthesis. *J. Phys. Chem. B* **105,** 5743–5750 (2001).

9. Dictor, R. A. & Bell, A. T. Fischer-Tropsch synthesis over reduced and unreduced iron oxide catalysts. *J. Catal.* **97,** 121–136 (1986).

10. Rao, K. R. P. M. *et al.* Mössbauer Study of Iron Fischer−Tropsch Catalysts during Activation and Synthesis. *Energy & Fuels* **10,** 546–551 (1996).

11. Raje, A. P., O'Brien, R. J. & Davis, B. H. Effect of potassium promotion on iron-based catalysts for Fischer-Tropsch synthesis. *J. Catal.* **180,** 36–43 (1998).

12. Luo, M., O'Brien, R. J., Bao, S. & Davis, B. H. Fischer-Tropsch synthesis: induction and steady-state activity of high-alpha potassium promoted iron catalysts. *Appl. Catal., A* **239,** 111–120 (2003).

13. Yang, Y., Xiang, H.-W., Xu, Y.-Y., Bai, L. & Li, Y.-W. Effect of potassium promoter on precipitated iron-manganese catalyst for Fischer-Tropsch synthesis. *Appl. Catal., A* **266,** 181–194 (2004).

14. O'Brien, R. J. & Davis, B. H. Impact of Copper on an Alkali Promoted Iron Fischer-Tropsch Catalyst. *Catal. Lett.* **94,** 1–6 (2004).

15. Li, J. *et al.* Effect of alkalis on iron-based Fischer-Tropsch synthesis catalysts: Alkali-FeOx interaction, reduction, and catalytic performance. *Appl. Catal. A Gen.* **528,** 131–141 (2016).

16. Jiang, F., Zhang, M., Liu, B., Xu, Y. & Liu, X. Insights into the influence of support and potassium or sulfur promoter on iron-based Fischer-Tropsch synthesis: understanding the control of catalytic activity, selectivity to lower olefins, and catalyst deactivation. *Catal. Sci. Technol.* **7,** 1245–1265 (2017).

17. Davis, B. H. Fischer-Tropsch synthesis: relationship between iron catalyst composition and process variables. *Catal. Today* **84,** 83–98 (2003).

18. Zhang, Y., Sirimanothan, N., O'Brien, R. J., Hamdeh, H. H. & Davis, B. H. Study of deactivation of iron-based Fischer-Tropsch synthesis catalysts. *Stud. Surf. Sci. Catal.* **139,** 125–132 (2001).

19. Niemantsverdriet, J. W., Van Der Kraan, A. M., Van Der Baan, H. S. & Van Dijk, W. L. Behavior of metallic iron catalysts during Fischer-Tropsch synthesis studied with Moessbauer spectroscopy, x-ray diffraction, carbon content determination, and reaction kinetic measurements. *J. Phys. Chem.* **84,** 3363–3370 (1980).

20. Reymond, J. P., Meriaudeau, P. & Teichner, S. J. Changes in the surface structure and composition of an iron catalyst of reduced or unreduced iron(IV) oxide during the reaction of carbon monoxide and hydrogen. *J. Catal.* **75,** 39–48 (1982).

21. Bukur, D. B., Lang, X. & Ding, Y. Pretreatment effect studies with a precipitated iron Fischer-Tropsch catalyst in a slurry reactor. *Appl. Catal., A* **186,** 255–275 (1999).

22. Bian, G., Oonuki, A., Koizumi, N., Kobayashi, Y. & Yamada, M. Syngas adsorption on precipitated iron catalysts reduced by H2, syngas or CO and on those used for high-pressure FT synthesis by in situ diffuse reflectance FTIR spectroscopy. *Appl. Catal., A* **219,** 13–24 (2001).

23. Graham, U. M., Dozier, A. K., Srinivasan, R., Thomas, M. & Davis, B. H. Formation and characterization of nanozones in iron catalysts for Fischer-Tropsch synthesis. *Prepr. - Am. Chem. Soc., Div. Pet. Chem.* **50,** 178–181 (2005).

24. Shroff, M. D. & Datye, A. K. The importance of passivation in the study of iron Fischer-Tropsch catalysts. *Catal. Lett.* **37,** 101–106 (1996).

25. Jin, Y., Xu, H. & Datye, A. K. Electron Energy Loss Spectroscopy (EELS) of Iron Fischer-Tropsch Catalysts. *Microsc. Microanal.* **12,** 124–134 (2006).

26. Su, D. S., Zhang, B. & Schlogl, R. Electron Microscopy of Solid Catalysts-Transforming from a Challenge to a Toolbox. *Chem. Rev. (Washington, DC, United States)* **115,** 2818–2882 (2015).

27. Jung, H. & Thomson, W. J. Dynamic x-ray diffraction study of an unsupported iron catalyst in Fischer-Tropsch synthesis. *J. Catal.* **134,** 654–667 (1992).

28. Jung, H. & Thomson, W. J. Dynamic x-ray diffraction study of an unreduced iron oxide catalyst in Fischer-Tropsch synthesis. *J. Catal.* **139,** 375–382 (1993).

29. Li, S. *et al.* Structural analysis of unpromoted Fe-based Fischer-Tropsch catalysts using X-ray absorption spectroscopy. *Appl. Catal., A* **219,** 215–222 (2001).

30. de Smit, E. *et al.* Nanoscale chemical imaging of a working catalyst by scanning transmission X-ray microscopy. *Nature* **456,** 222–225 (2008).

31. Lazar, S., Zandbergen, H. W., Botton, G. A., Wu, M.-Y. & Tichelaar, F. D. Materials science applications of HREELS in near edge structure analysis and low-energy loss spectroscopy. *Ultramicroscopy* **96,** 535–546 (2003).

32. Janbroers, S., Zandbergen, H. W., de Kruijff, T. R., Xu, Q. & Kooyman, P. J. Preparation of carbon-free TEM microgrids by metal sputtering. *Ultramicroscopy* **109,** 1105–9 (2009).

33. Zandbergen, H. W., Kooyman, P. J. & an Langeveld, A. D. Electron Microscopy 1998, proceedings ICEM 14. in *Electron Microscopy 1998, proceedings ICEM 14* **II,** 491–492 (1998).

34. Larson, A. C. & Von Dreele, R. B. *General Structure Analysis System (GSAS).* (Los Alamos National Laboratory, 2000).

35. Mitchell, D. R. G. Measure EELS Peak Intensities script version 2.1, http://www.felmi-zfe.tugraz.at/dm_scripts/http://www.felmi-zfe.tugraz.at/dm_scripts/. (2006).

36. Krishnan, K. M. Iron L3,2 near-edge fine structure studies. *Ultramicroscopy* **32,** 309–311 (1990).

37. Hirotsu, Y. & Nagakura, S. Crystal structure and morphology of the carbide precipitated from martensitic high carbon steel during the first stage of tempering. *Acta Met.* **20,** 645–655 (1972).

38. Fruchart, D., Fruchart, R., Chaudouet, P., Senateur, J. P. & Rouault, A. No Title. *J. Sol. State Chem.* **51,** 246–252 (1984).

39. Pinsker, Z. G. & Kaverin, S. V. No Title. *Ref. Krist.* **1,** 66–72 (1956).

40. Datye, A. K. *et al.* The nature of the active phase in iron Fischer-Tropsch catalysts. *Stud. Surf. Sci. Catal.* **130B,** 1139–1144 (2000).

41. Jin, Y. Phase transformation of iron-based catalysts for Fischer-Tropsch synthesis. *Thesis Univ. New Mex. USA* (1999).

42. Le Caër, G., Dubois, J. M., Pijolat, M., Perrichon, V. & Bussiere, P. Characterization by Moessbauer spectroscopy of iron carbides formed by Fischer-Tropsch synthesis. *J. Phys. Chem.* **86,** 4799–4808 (1982).

43. Le Caër, G. Structural model for commensurate and non-periodic carbides formed by christallization of amorphous iron carbon alloys. *Mater. Sci. Eng.* **97,** 273–277 (1988).

44. Shroff, M. D. *et al.* Activation of precipitated iron Fischer-Tropsch synthesis catalysts. *J. Catal.* **156,** 185–207 (1995).

45. Bukur, D. B. *et al.* Activation Studies with a Precipitated Iron Catalyst for Fischer-Tropsch Synthesis. *J. Catal.* **155,** 353–365 (1995).

46. Jin, Y., Mansker, L. D., Bukur, D. B. & Datye, A. K. Characterization of slurry phase iron catalysts for Fischer-Tropsch synthesis. *Appl. Catal., A* **186,** 277–296 (1999).

47. Jin, Y. & Datye, A. K. Phase transformations in iron Fischer-Tropsch catalysts during temperature-programmed reduction. *J. Catal.* **196,** 8–17 (2000).

CHAPTER 2

3

A combined X-RAY and electron diffraction study of freshly carburized iron based Fischer-Tropsch catalyst

In the previous chapter, we discussed the unsolved nature of a powder X-ray diffraction (PXRD) pattern obtained in a quasi in-situ analysis of carburized Fisher-Tropsch catalysts. Here we report a characterization study in which we combine electron diffraction (ED) and PXRD to elucidate the unidentified iron carbide.

By simulating ED data we found a faulted iron carbide structure with features of χ-Fe$_5$C$_2$ and, for what in the literature has been designated as 'hypothetical', θ_∞-Fe$_2$C. The faulted nature of the carbide is confirmed by the ED patterns.

Our stacking fault model can explain the previously observed PXRD pattern.

3.1. Introduction

In Chapter 2 we discussed (quasi) in-situ TEM measurements and an unresolved PXRD pattern obtained from a carburized Fisher-Tropsch catalyst[1]. It was found that the PXRD pattern could not easily be matched with any known carbide phases.

In literature, a model for a general class of layered carbide structures has been outlined. Andersson and Hyde[2] were the first to show that the structures of both known (χ-Fe$_5$C$_2$ and θ-Fe$_3$C) and unknown carbides can be generated by assuming different frequencies of twinning defects in a hexagonal close packed (hcp) iron lattice. Each twinning defect creates a layer of hexagonal prisms of iron atoms in which carbon atoms reside. The resulting carbide structure is built from such trigonal prismatic layers interspersed by any number, including zero, of iron hcp layers. Nagakura et al.[3] successfully used this model to characterize intermediate phases between χ-Fe$_5$C$_2$ and θ-Fe$_3$C from their TEM micrographs and ED patterns. Le Caër and Bauer-Grosse[4] pointed out that χ-Fe$_5$C$_2$ is intermediate between the θ-Fe$_3$C carbide and a hypothetical carbide that can be constructed in the twinning model, by assuming there are no iron layers between the trigonal prismatic layers at all. In the nomenclature first introduced by Nagakura et al., this hypothetical carbide should be called "θ_∞-Fe$_2$C" as was suggested by Aouni and Bauer-Grosse[5]. In principle, a whole range of intermediates between θ_∞-Fe$_2$C and θ-Fe$_3$C is conceivable with Fe/C ratios ranging from 2 to 3. The authors showed that for Fe/C ratios of about 2.36, the ED spot density around the central spot over a number of patterns corresponded to a stacking of layers intermediate between the χ-Fe$_5$C$_2$ and θ_∞-Fe$_2$C compatible modes.

In an attempt to fully elucidate the unknown structure, we have recorded ED patterns of randomly chosen areas with a crystalline appearance.

3.2. Materials and Methods

The sample preparation, including carburization experiments, is described in paragraph 2.2 of the previous chapter.

3.2.1. X-Ray Diffraction (XRD)

XRD was performed using a Bruker D8 diffractometer equipped with a Cu Kα source. Variable (θ-compensating) anti-scatter and divergence slits were used. Rietveld refinement was performed using the GSAS software package[6]. The carburized sample was measured quasi in-situ under nitrogen using a special dome (Bruker AB100B36).

3.2.2. Electron Diffraction

The samples were examined using both a Philips CM200 and a FEI Titan transmission electron microscope equipped with a field emission gun operated at 200 kV and 300 kV respectively. Special carbon-free TEM grids were used to minimize interference[7]. Details on the preparation of these grids can be found in Chapter 6. Samples were loaded in a special airtight sample transfer holder in a glove box and introduced into the TEM without any contact with the ambient atmosphere[8].

3.2.3. Computational Details

The PXRD pattern was simulated using DIFFaX written by Treacy et al.[9] ED patterns were simulated using JECP/ED written by X.Z. Li[10]. With this program, diffraction patterns with geometrical factors and kinematical intensities are calculated.

3.3. Results and Discussion

3.3.1. Powder X-Ray Diffraction

The PXRD scan we obtained is shown in Figure 2. Magnetite is clearly present, albeit as a minor phase. The scan is dominated by a signal from a poorly crystalline iron carbide phase. This pattern is characterized by diffraction angles at 39.0, 40.8, 43.1, 46.6, 58.1 and 67.6 °2θ (or spacings of 2.31, 2.21, 2.10, 1.95, 1.59 and 1.39 Å respectively). Datye et al. published a pattern that appears to be similar and assigned it to faulted χ-Fe$_5$C$_2$[11]. They also reported a substantial contribution from the Eckstrom-Adcock Fe$_7$C$_3$ carbide

for which we cannot find any evidence. Also Jin et al.[12] and Mansker[13] reported PXRD patterns of iron carbides, in some of which the 'unknown phase' appears to be present (among other phases). They also assigned the pattern to be faulted χ-Fe$_5$C$_2$.

The picture below shows our observed pattern and a simulated scan for χ-Fe$_5$C$_2$. As can be seen, it is difficult to fit the observed pattern into an χ-Fe$_5$C$_2$ assignment.
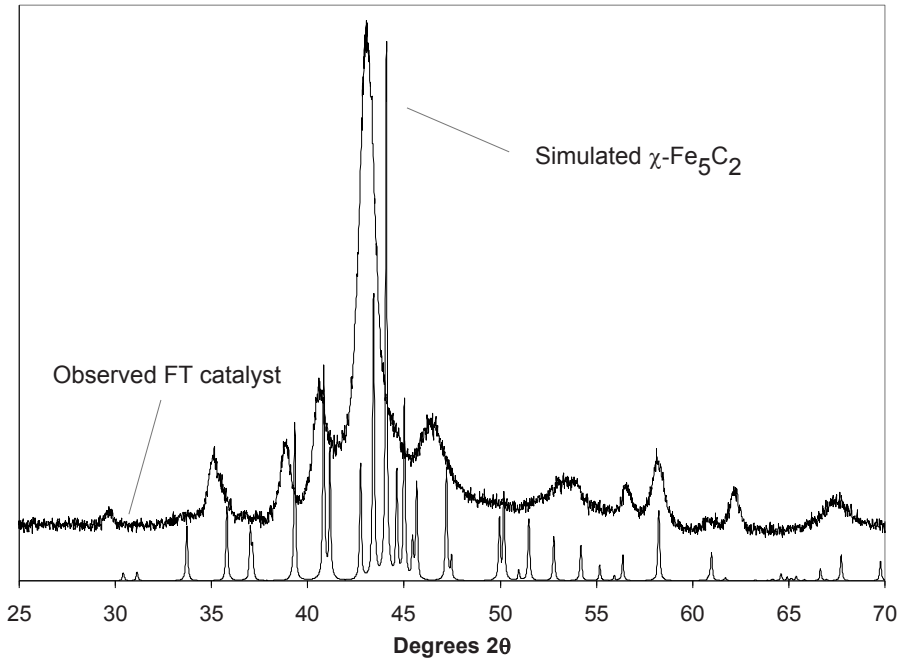
Figure 1: Observed PXRD scan of our carbururized catalyst versus χ-Fe$_5$C$_2$

In an attempt to resolve the observed pattern, we have performed Rietveld refinement using the GSAS program[6] allowing the maximum amount of freedom (which includes choosing the crystal structure for χ-Fe$_5$C$_2$ rather than the C$_{2/c}$ symmetry as Du Plessis recommends[14]) and refining all six cell parameters as well as using a 15 parameter model for anisotropic line broadening[15]. However, we were unable to obtain a satisfactory match. Figure 2 shows the best result we obtained. Computed and observed diffraction angles are not sufficiently aligned even with full account of sample displacement shift. Note that the most intense reflection in the simulated χ-Fe$_5$C$_2$ pattern (at about 44.2 °2θ) is essentially absent in our observed scans leading to a very unrealistic fitted background.

Also note that the cell parameters obtained from our best Rietveld fit, being 89.52°, 100.80° and 93.94° are substantially different from those determined by Du Plessis

(being 89.88°, 97.77° and 89.96° respectively), showing that the observed pattern cannot easily be matched with χ-Fe_5C_2.

Du Plessis has refined and, in some cases, re-determined crystal structures for the carbides ε'-$Fe_{2.2}C$, χ-Fe_5C_2, ε-Fe_3C and Fe_7C_3[14]. Crystal structures are also known for η-Fe_2C[16], θ-Fe_3C[17] and Fe_4C[18]. However, none of these structures yield a simulated pattern fully corresponding to the XRD pattern we found. Consequently, we turned to electron diffraction of seemingly crystalline areas in our sample in an attempt to elucidate the carbide structure.
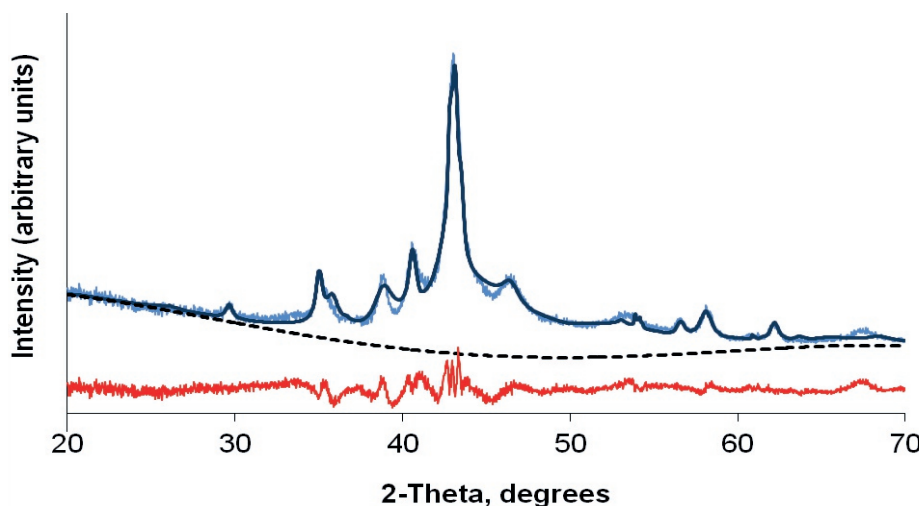
Figure 2: Rietveld refinement of the PXRD scan from figure 1.The upper part of the graph shows the measured and simulated scan, the bottom part the difference between the two. Magnetite and χ-Fe_5C_2 were used as phases. Although χ-Fe_5C_2 can explain some of the iron carbide signal, the match is not satisfactory. Note the fitted background (dashed line). Its unrealistic shape is due the fact that some intense lines χ-Fe_5C_2 must necessarily become very broad to match the observed scan. This is compensated for by the fitted background.

3.3.2. Electron diffraction

In our sample we found ED patterns resembling those simulated from the crystal structure of χ-Fe_5C_2 (see Figure 3).
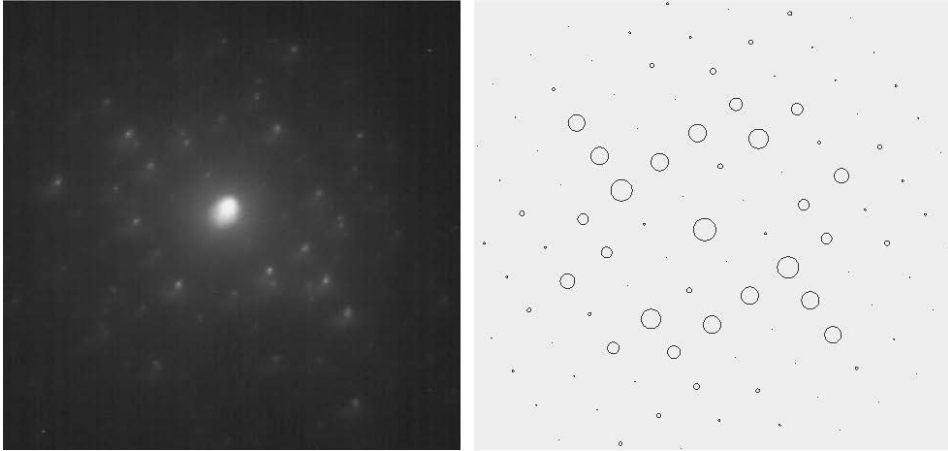
Figure 3: Observed ED pattern (left) compared to one simulated for χ-Fe₅C₂ carbide assuming (1 1 0) zone vector. The circle size in the simulated pattern represents the spot intensity

However, we also recorded ED patterns that could not be assigned to any known carbide nor to magnetite. In order to clarify what we found, we first have to consider the relation between the structures of θ-Fe$_3$C, χ-Fe$_5$C$_2$ and θ_∞-Fe$_2$C in more detail.

We first consider the structure of χ-Fe$_5$C$_2$ as shown in Figure 4.
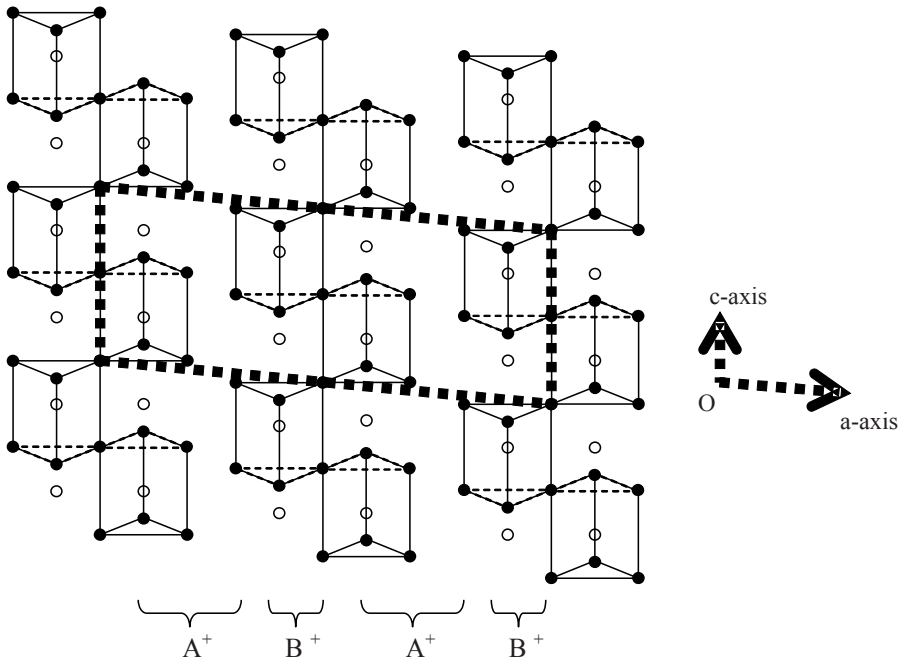
Figure 4: The structure of χ-Fe5C2 shown as a stacking of two different layers

Figure 4 shows a schematic representation of the monoclinic[19] crystal structure of χ-Fe_5C_2. The a and c axes of the unit cell are given as thick dashed lines; the b axis is perpendicular to the paper, pointing down. Based on the Andersson-Hyde model[2] the iron atoms (given as black circles) form a severely faulted hexagonal lattice. At each fault plane, the iron atoms form trigonal prisms that contain the carbide C atoms (open circles). When these faults occur at intermittent layers, the prisms share corners and edges. In the figure, only half the prisms were drawn explicitly, for the sake of clarity. As shown in the figure, χ-Fe_5C_2 can be visualized built from alternately three and two iron layers without stacking faults; we will call these the A^+ and B^+ layers (the reason for naming such layers as well as the "+" superscript will become clear later on). In the space group symmetry of monoclinic χ-Fe_5C_2 ($C_{2/c}$), each atom has a copy displaced along half the a and half the b axis (and at the same position along the c-axis). This of course also holds for the layers as shown in the picture.

The crystal structure of θ-Fe_3C is shown in Figure 5.
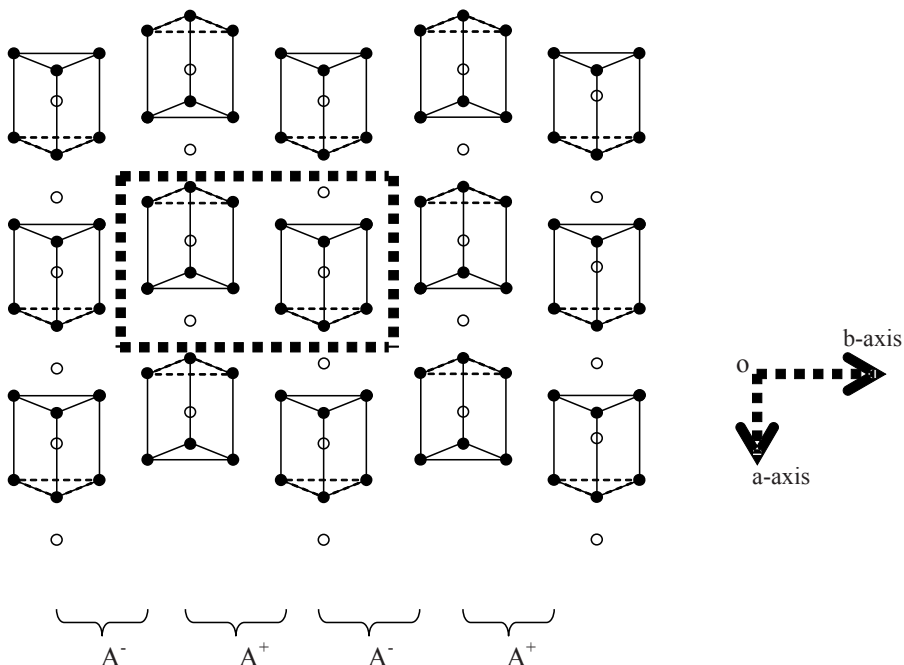
Figure 5: The structure of θ-Fe_3C shown as a stacking of A type layers

This structure is also built up from layers of trigonal prisms. Alternating layers are all topologically equivalent to the A layer in the χ-Fe_5C_2 structure, except that every other

layer is inverted along the a axis of the θ-Fe₃C crystal structure[16]. We will therefore designate these layers as A⁺ and A⁻. The θ-Fe₃C structure viewed this way is an A⁺A⁻ A⁺A⁻ A⁺A⁻ A⁺A⁻… stacking sequence (with specific stacking vectors).

Compared to χ-Fe₅C₂, θ-Fe₃C has more Fe layers and therefore a lower carbon content. In this respect, stacking only B layers would lead to a higher carbon content than χ-Fe₅C₂. This structure, the "hypothetical θ∞-Fe₂C" carbide[17] is given in Figure 6. The corresponding unit cell has P$_{bcm}$ symmetry[5].
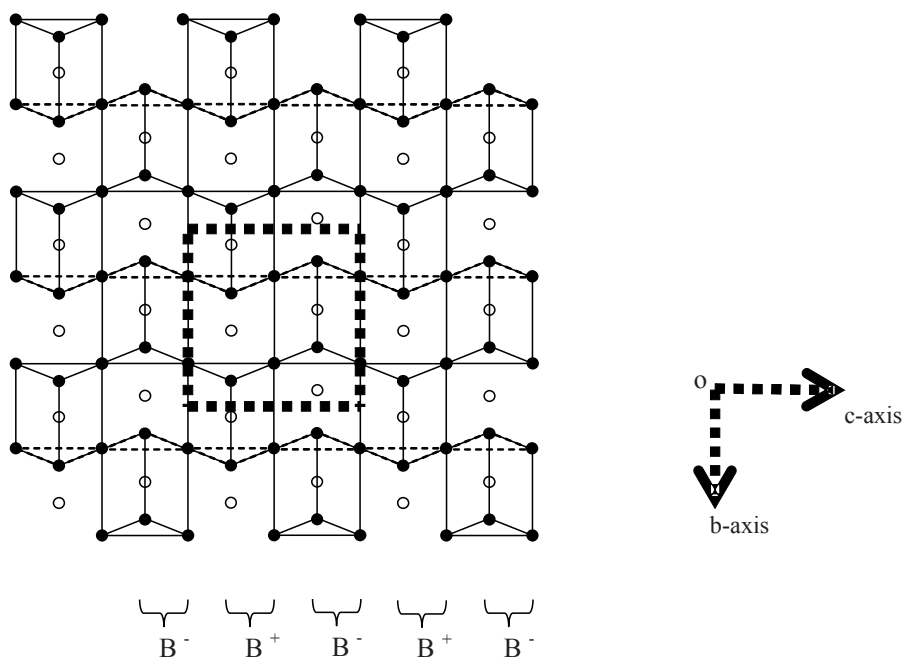
Figure 6: The structure of θ∞–Fe₂C shown as a stacking of B type layers

In order to investigate whether the observed PXRD pattern could be explained by a particular stacking of A and B layers, we have created a numerical model able to account for all possible stacking modes.

The structural units for the A and B layers and displacement vectors are given in fractional coordinates. These refer to three orthogonal axes: a=4.625 Å, b=5.059 Å and c=5.741 Å long. The c-axis is the stacking direction. Axes a and b therefore determine the layer dimensions.

The lengths of both the b and c axes have been directly derived from the crystal structure of χ-Fe₅C₂; the a axis length has been adapted from 4.579 Å in χ-Fe₅C₂ to 4.625 Å for a

better match between the simulated and observed PXRD pattern (*vide infra*). The fractional coordinates were all derived from the χ-Fe_5C_2 crystal structure and are given in Table 1:

A^+ unit		
Atom	X	y
C1	-0.391	0.156
C2	0.209	-0.344
Fe1	-0.182	0.5
Fe2	0	0
Fe3	0.486	-0.155
Fe4	0.332	0.345
Fe5	-0.168	0.215
Fe6	-0.014	-0.285
B^+ unit		
atom	X	y
C1	0	0
C2	-0.4	-0.5
Fe1	0.209	-0.344
Fe2	0.391	0.156
Fe3	-0.134	0.298
Fe4	-0.266	-0.202

Table 1: fractional coordinates of the A+ and B+ units

The A^- and B^- units are equivalent to the A^+ and B^+ units, respectively, except for the inversion of the sign of the fractional y coordinate.

The stacking vectors used are shown in Table 2.

Vector	x	y	z	Forms
$A^+ \to B^+$	0.109	0.412	0.598	χ-Fe_5C_2
$A^+ \to A^-$	0.5	0.573	0.587	θ-Fe_3C
$B^+ \to A^+$	0.391	-0.554	0.402	χ-Fe_5C_2
$B^+ \to B^-$	0	-0.403	0.402	θ_∞-Fe_2C
$A^- \to A^+$	0.5	0.427	0.587	θ-Fe_3C
$A^- \to B^-$	0.109	-0.412	0.598	χ-Fe_5C_2
$B^- \to B^+$	0	0.403	0.402	θ_∞-Fe_2C
$B^- \to A^-$	0.391	0.554	0.402	χ-Fe_5C_2

Table 2: stacking vectors of different iron carbides

The stacking vectors were derived from the known crystal structures of χ-Fe$_5$C$_2$ and θ-Fe$_3$C and the P$_{bcm}$ symmetry assumed for the hypothetical θ_∞-Fe$_2$C. Note that the y-components of two A$^+$→ B$^+$ and two B$^+$→ A$^+$ vectors do not add up to an integer number. This is as it should be, because it makes the layers shift along the b vector and thereby introduces the monoclinic angle in the unit cell of χ-Fe$_5$C$_2$.

DIFFaX simulations

DIFFaX[9] was used to simulate the diffraction pattern resulting from non-perfect layer stackings. The A and B units defined in the previous paragraph, as well as the stacking vectors, were first checked to see if the powder patterns for perfect χ-Fe$_5$C$_2$ and θ-Fe$_3$C corresponded to those directly simulated from the crystal structure.
We were able to obtain a satisfactory match between the observed and simulated powder pattern (see Figure 7) by stipulating the following:

1. An A$^+$ layer is always followed by a B$^+$ and an A$^-$ layer is always followed by a B$^-$
2. A B$^+$ layer has 60% probability to be followed by a B$^-$ layer and 40% probability to be followed by A$^+$; likewise a B$^-$ has 60% probability to be followed by a B$^+$ layer and 40% probability to be followed by A$^-$
3. A total of fifteen A and B layers are stacked in any single crystallite
4. The layers are about 20 nm in diameter

Although we have based the lattice and atom coordinates as much as possible on those of the known χ-Fe$_5$C$_2$ structure, we found we had to increase the size of the first reference axis in our simulations to 4.625 Å. We speculate that the increase in axis length reflects a partial transition from χ-Fe$_5$C$_2$ to θ_∞-Fe$_2$C. The corresponding experimental axis lengths are 4.525 Å (c axis of θ-Fe$_3$C) and 4.579 Å (b axis of χ-Fe$_5$C$_2$). The 20 nm diameter for the layers is based on the agreement between observed and simulated peak broadening as was the total number of 15 layers, which is equivalent to a height of about 7 nm. These dimensions are in agreement with the TEM images of the freshly carburized catalyst as shown in Chapter 2.
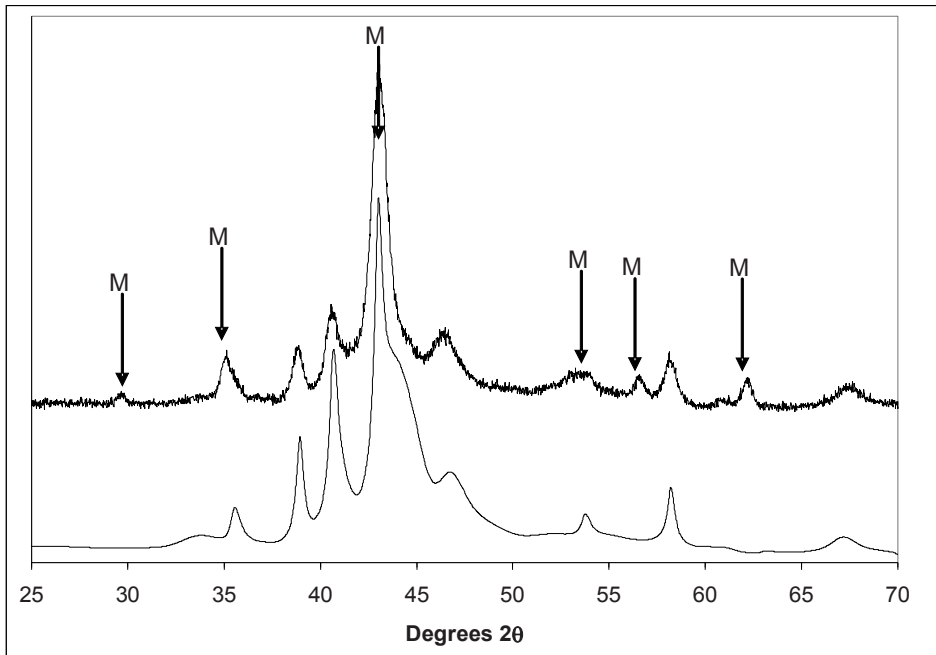
Figure 7: DIFFaX simulated (bottom) and observed powder pattern (top). In this figure, the powder pattern simulated is based on a random interchange of χ-Fe_5C_2 and θ_∞–Fe_2C type stacking. "M" designates signal due to magnetite.

When stacking sequences of the type $A^+A^-A^+A^-$… (that correspond to the θ-Fe_3C structure) are allowed, this reduces the agreement between observed and simulated pattern. This is shown in Figure 8. The simulated pattern in this figure is based on similar rules as before except that in this case a B layer is always followed by the appropriate A layer, but an A layer has a 60% chance of being followed by an A layer of opposite sign. Among the features that do not agree with the experimentally observed pattern we find a broad signal at about 38 °2θ and quite different general structure in the 45-50 °2θ and > 67 °2θ ranges. We conclude that θ-Fe_3C type stacking makes no or a very minor contribution to the experimentally observed pattern.
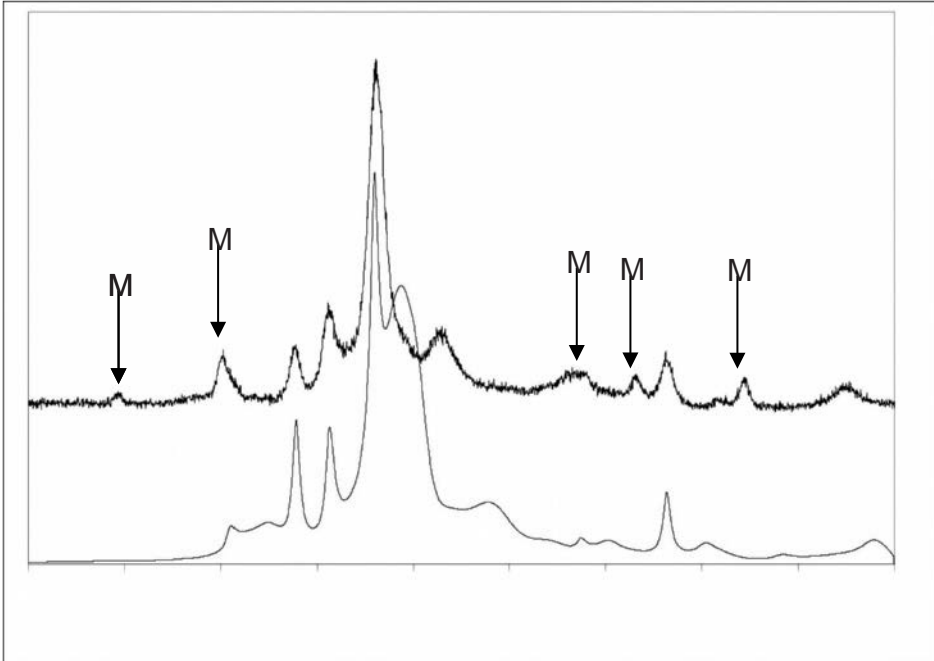
Figure 8: DIFFaX simulated (bottom) and observed powder pattern (top). In this figure, the powder pattern simulated is based on a random interchange of χ-Fe$_5$C$_2$ and θ-Fe$_3$C stacking. The agreement between observed and simulated is substantially less than shown in figure 9 for a random interchange of χ-Fe$_5$C$_2$ and θ_∞-Fe$_2$C."M" designates signal due to magnetite.

Evidence for the "hypothetical" θ_∞-Fe$_2$C

The structure of θ_∞-Fe$_2$C, taken as a perfect crystal, commensurable with the DIFFaX simulations can be described as in Table 3:

SG: P$_{bcm}$		
a		4.625
b		5.059
c		4.616
atom	x	y
Fe1	0.091	0.395
Fe2	0.423	0.75
C1	0.3	0.048

Tabel 3: lattice parameters and fractional coordinates of θ_∞–Fe$_2$C

In view of the relatively high probability of $B^+B^-B^+B^-$… type stackings, we would expect to find among our ED patterns some that correspond to the θ_∞-Fe_2C structure. And, in fact, we do as is shown in Figure 9. However, we have only found ED patterns for a zone vector perpendicular to the B layers, so the number of layers in the crystallites may be quite small.

Note that the different intensity ratios between spots in the simulated and observed patterns suggest that the atom coordinates could be improved upon.
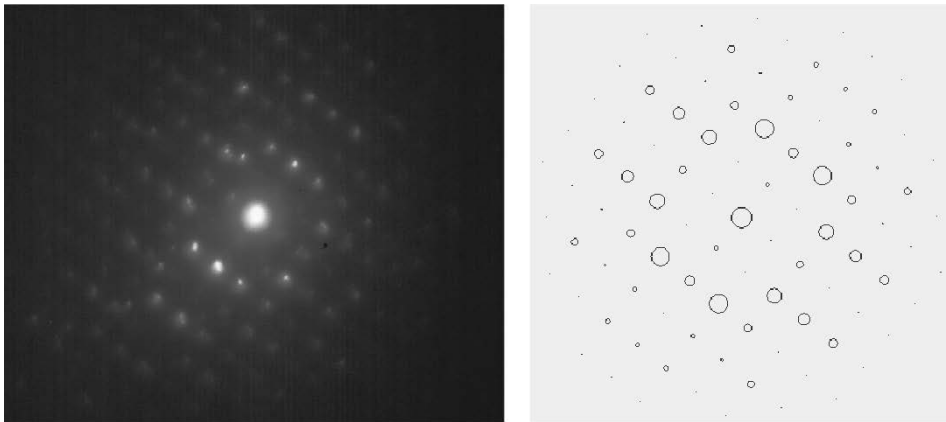
Figure 9: An experimental ED pattern compared to one simulated based on the assumed Pbcm θ_∞−Fe_2C structure

Also some streaked patterns were found as shown in Figure 10. Such patterns are indicative of crystalline material that is well ordered in at least one direction and disordered in at least one other. This suggests a random stacking of layers in a way that fits with the crystal structure of χ-Fe_5C_2 for a few layers but also with at least one other crystal structure for a different sequence of layers. By calibrating the pixel distance between the streaks with the inverse spacings in Figures 3 and 9 using the ImageJ program and the EXTRAX plug-in [20,21], we can assign the streaked patterns to what corresponds to the ED pattern observed with a (0 1 3) zone vector for χ-Fe_5C_2 and a (1 3 0) zone vector for θ_∞-Fe_2C. These two patterns share a common base vector determined only by the two lattice vectors spanning the layers. As shown in Figure 11, however, the other base vector is different. Thus the two patterns from the idealized structures fit in one direction, but not in the other.
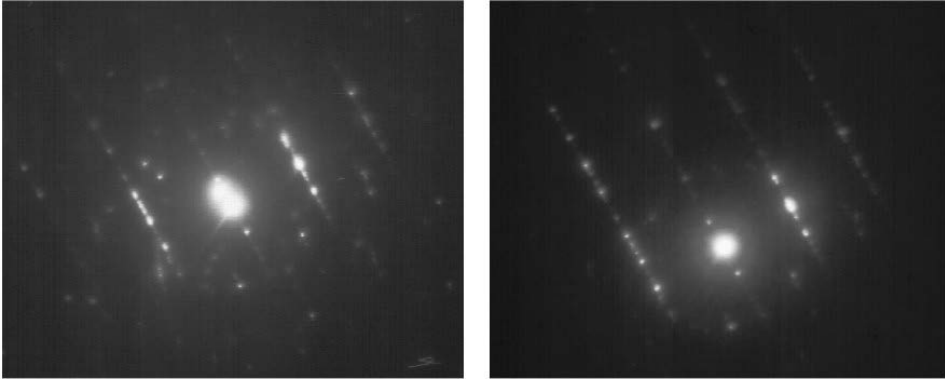
Figure 10: Some typical streaked ED patterns observed
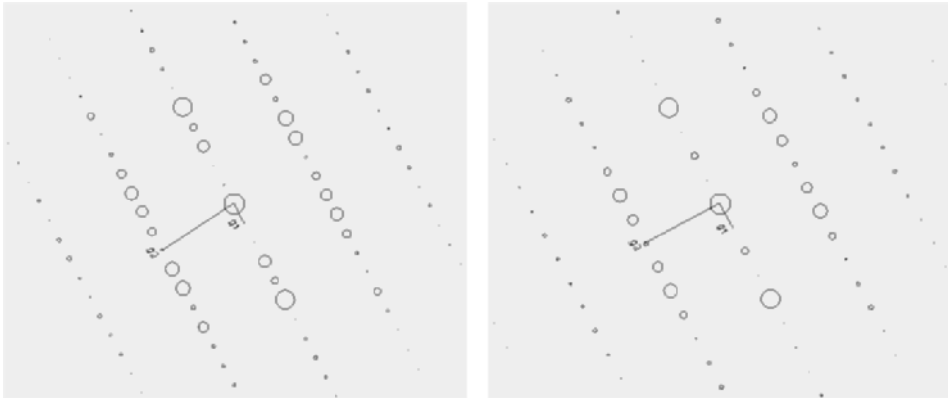
Figure 11: Simulated ED patterns for (left) χ–Fe$_5$C$_2$ (zone axis (0 1 3)) and (right) θ_∞–Fe$_2$C (zone axis (1 3 0)). The g2 base vectors in both patterns are of the same length, but the g1 vector is of different length (and has a different angle to the g2 vector).

Overall, it is probably not meaningful to characterize the observed carbide as "a mixture of χ-Fe$_5$C$_2$ and θ-Fe$_3$C". Instead, it should be thought of in general terms as a particular representative of a whole class of Stacked Prismatic Layer (SPL) carbides. We recommended not describing observed PXRD patterns of Fischer-Tropsch carbides into the known carbide structures. A more detailed analysis, combining several methods of characterization will often be required for a full and more meaningful characterization. Although we have found the PXRD pattern from Figure 2 and 7 in all our caburized samples, it does not necessarily follow that it should be generally encountered in freshly carburized Fe-based Fisher-Tropsch catalysts. De Smit et al.[22] have shown how the nature of the carbide formed during the carburization phase depends on the chemical potential of carbon. It is conceivable that the carbide structure found and characterized in

this paper is only formed under the specific conditions outlined in the experimental part (including the dopants present).

From the stacking probabilities we can compute that the average crystallite consists of 28.6% A layers and 71.4% B layers and therefore has a Fe/C ratio of 2.29, obviously in between 2.5 (as in χ-Fe_5C_2) and 2.0 (as in θ_∞-Fe_2C). It reflects a stronger driving force for carbon to dissolve into iron than possible in χ-Fe_5C_2. It may also have been the faulted nature of iron produced on reducing magnetite that allowed uptake of carbon to this amount.

3.4.   Conclusions

By combining information from both X-ray powder diffraction and (TEM) electron diffraction we characterized an unknown iron carbide phase. It is built up from two different layers (A and B; Layer A contains three and B contains two iron sub-layers while both have one sub-layer of carbon.). The well known χ-Fe_5C_2 carbide consists of a regular $A^+B^+A^+B^+A^+B^+$… stacking, while θ-Fe_3C carbide consists of an $A^+A^-A^+A^-$… stacking (A^- and A^+ are similar except for an inversion along one direction).

The carbide present in our freshly carburized FT catalyst is found to consist of an irregular stacking in which A^+ is always followed by B^+ (and A^- by B^-) but B^+ has a 60% chance of being followed by B^- instead of A^+ (and, likewise, B^- has a 60% chance of being followed by B^+). This stacking model explains the observed PXRD pattern (as is shown by a comparison between the experimental pattern and the one simulated by the DIFFaX program). We get further confirmation from the fact that among the Diffraction Patterns recorded in the TEM we find patterns nearly identical with patterns simulated by the JECP/ED program for the χ-Fe_5C_2 carbide ($A^+B^+A^+B^+A^+B^+$… or, equivalently, $A^-B^-A^-B^-A^-B^-$…) and for what in the literature has been designated as the "hypothetical θ_∞-Fe_2C" ($B^+B^-B^+B^-$…); we also find experimental electron diffraction patterns showing the faulted nature of the resulting carbide that are fully explained by the adopted structure model.

One implication of this structure model is that the C-content is higher than in the pure χ-Fe_5C_2 carbide (Fe/C = 2.29 instead of 2.5). At this point we can only speculate about cause and effect: whether the faulted nature of the carbide allows more carbon to be stored or whether the chemical potential of carbon during the carburization process forces the faulted structure on the carbide. To estimate the relative stability of the θ_∞-Fe_2C, we made Projector-Augmented Wave (PAW) calculations as discussed in Appendix A.

3.5.   References

1.   Janbroers, S., Louwen, J., Zandbergen, H. W. & Kooyman, P. J. Insights into the nature of iron-based Fischer-Tropsch catalysts from quasi in situ TEM-EELS and XRD. *J. Catal.* **268,** 235–242 (2009).

2.   Andersson, S. & Hyde, B. . Twinning on the Unit Cell Level as a Structure-Building Operation in the Solid State. *J. solid state Chem. solid state Chem.* **9,** 92–101 (1974).

3.   Nagakura, S., Toshiaki, S. & Kusunoki Michiko. Structure of the Precipitated Particles at the Third Stage of Tempering of Martensitic Iron--Carbon Steel Studied by High Resolution Electron Microscopy. *Trans. Jpn. Inst. Met.* **22,** 699–709 (1981).

4.   Le Caër, G. & Bauer-Grosse, E. Aperiodic carbides formed by crystallization of amorphous Fe-C alloys. *Hyperfine Interact.* **47,** 55–67 (1989).

5.   Aouni, A. & Bauer-Grosse, E. New periodic and aperiodic triangular prismatic sheet carbides obtained by crystallization of Mn1−xCx amorphous films and described by the chemical twinning model. *J. Alloy. Comp.* **335,** 157–164 (2002).

6.   Larson, A. C. & Von Dreele, R. B. *General Structure Analysis System (GSAS).* (Los Alamos National Laboratory, 2000).

7.   Janbroers, S., Zandbergen, H. W., de Kruijff, T. R., Xu, Q. & Kooyman, P. J. Preparation of carbon-free TEM microgrids by metal sputtering. *Ultramicroscopy* **109,** 1105–9 (2009).

8.   Zandbergen, H. W., Kooyman, P. J. & an Langeveld, A. D. Electron Microscopy 1998, proceedings ICEM 14. in *Electron Microscopy 1998, proceedings ICEM 14* **II,** 491–492 (1998).

9.   Treacy, M. M. J., Newsam, J. M. & Deem, M. W. A General Recursion Method for Calculating Diffracted Intensities from Crystals Containing Planar Faults. *Proc. R. Soc. London. Ser. A Math. Phys. Sci.* **433,** 499–520 (1991).

10.   Li, X. Z. A computer program for simulation of selected-area and precession electron diffraction patterns. *J. Appl. Crystallogr.* **36,** 956 (2003).

11.   Datye, A. K. *et al.* The nature of the active phase in iron Fischer-Tropsch catalysts. *Stud. Surf. Sci. Catal.* **130B,** 1139–1144 (2000).

12.   Jin, Y. Phase transformation of iron-based catalysts for Fischer-Tropsch synthesis. *Thesis Univ. New Mex. USA* (1999).

13.   Mansker, L. D. Characterization of working iron Fischer-Tropsch catalysts using quantitative diffraction methods. *Thesis Univ. New Mex. USA* (1999).

14.   Plessis, H. E. Du. The crystal structures of the iron carbides. *Thesis Univ. Johannesbg.* (2008).

15. Stephens, P. W. Phenomenological model of anisotropic peak broadening in powder diffraction. *J. Appl. Crystallogr.* **32,** 281–289 (1999).

16. Hirotsu, Y. & Nagakura, S. Crystal structure and morphology of the carbide precipitated from martensitic high carbon steel during the first stage of tempering. *Acta Met.* **20,** 645–655 (1972).

17. Fruchart, D., Fruchart, R., Chaudouet, P., Senateur, J. P. & Rouault, A. No Title. *J. Sol. State Chem.* **51,** 246–252 (1984).

18. Pinsker, Z. G. & Kaverin, S. V. No Title. *Ref. Krist.* **1,** 66–72 (1956).

19. Retief, J. J. Powder diffraction data and Rietveld refinement of Hägg-carbide, χ-Fe5C2. *Powder Diffr.* **14,** 130–132 (1999).

20. Abramoff, M. D., Magalhães, P. J. & Ram, S. J. No Title. *Biophotonics Int.* **11,** 36–42 (2004).

21. Dorcet, V., Larose, X., Fermin, C., Bissey, M. & Boullay, P. Extrax: an ImageJ plug-in for electron diffraction intensity extraction. *J. Appl. Crystallogr.* **43,** 191–195 (2010).

22. de Smit, E. *et al.* Stability and reactivity of -chi-theta iron carbide catalyst phases in Fischer-Tropsch synthesis: controlling mu(C). PG - 14928-41. *J. Am. Chem. Soc.* **132,** 14928–14941 (2010).

CHAPTER 3

4

In situ carburization

4.1.   Introduction

Because the catalytically active species are not iron oxides but iron carbides[1], the catalyst precursor needs to be activated. A very convenient activation procedure is a reaction with carbon monoxide[2,3]. Since this activation step is usually performed inside the reactor (in situ at high temperature and high pressure), studying this process is not trivial. To overcome this problem, (quasi) in situ X-Ray Diffraction (XRD) and Mössbauer spectroscopy can be performed[4–8]. However, these bulk techniques lack spatial resolution and do not necessarily give information on the catalyst surface where the catalytic reactions take place. Another approach is to do quasi in situ carburizations and transfer the samples into a transmission electron microscope without exposure to air as reported earlier[9]. However, via this route it is very difficult to study the actual transformations of one specific region at the nanoscale. Therefore, we turned to an Environmental Transmission Electron Microscope (ETEM)[8,10,11], where the evolution of nanoscale areas can be followed using imaging techniques during the carburization process. In addition, Electron Energy Loss Spectroscopy (EELS) provides information about the composition and oxidation state of individual nano particles. A disadvantage of ETEM is that the maximum pressure is at least two orders of magnitude lower (maximum 50 Torr but in practice 5 Torr to prevent losing resolution) than what is normally used during catalyst activation (typically 750 Torr or higher). In this study we compare results obtained from the ETEM with quasi in situ data of catalysts carburized at higher pressures.

4.2.   Materials and Methods

4.2.1.   Catalyst preparation

Catalyst precursors were prepared by precipitation of iron nitrate with ammonia. While stirring at 70°C, 11.2 kg 4N ammonia was added to a solution of 5.06 kg $Fe(NO_3)_3 \cdot 9H_2O$ in 14.6 kg water, leading to a pH of 7.4. After filtration, the filter cake was washed three times with 1.7 liters of demineralized water (5.1 liters in total). Then, a 10 wt% slurry was prepared by adding 5.7 liters water to 4.0 kg wet based filter cake while stirring. The slurry was subsequently split into two parts to prepare a non-promoted and a potassium promoted catalyst precursor.

For the non-promoted precursor, the slurry was spray-dried using a conventional spray-drier (type Niro SD-6.3-R equipped with a Niro FU11 rotary atomizer). The following settings were used: rotary speed = 12600 rpm, inlet temperature = 400°C, outlet

temperature = 140°C. A static calcination was performed using a shallow bed of catalyst powder using the following settings: ramp = 2°/min, final temperature = 350°C, dwell = 4 hours.

For the potassium-promoted precursor, 36.6 grams of K_2CO_3 were added to the slurry to obtain an equivalent of 5.4 wt% K_2O on the final catalyst. The sample was spray-dried and calcined as described for the non-promoted sample.

4.2.2. Transmission Electron Microscopy

In this paper we present data obtained from two different electron microscopes. The in situ carburizations were performed using a Tecnai F-20 field emission microscope operating at 200 kV. The gas reaction cell (ECELL, essentially a flow micro reactor) of this instrument allows us to perform atomic level observations of reactions at pressures up to 8 Torr, while reactions with gases under heating but without imaging can be performed up to 50 Torr. We denote this microscope as 'ETEM'.

Various reference experiments were performed using a traditional high-vacuum FEI Tecnai F20 microscope operated at 200 kV. In case of in situ heating experiments *(vide infra)* we used a Gatan 652 double tilt heating holder. In this paper we denote this microscope as 'TEM'.

Both microscopes are equipped with a Gatan Imaging Filter (GIF) to perform EELS. The EELS data were obtained using the following, fixed conditions: camera length = 71 mm, entrance aperture = 2mm, dispersion = 0.30 eV / channel, exposure time = 2 s. The EELS edges are quantified by integration of the peak areas as described by Mitchell[12]. We used the peak areas to determine the valence states of the iron species and to calculate iron/oxygen ratios, which is a semi-quantitative way to determine the relative degrees of oxidation. Images were recorded with a Gatan CCD camera using Digital Micrograph 3.1™ software.

4.2.3. ETEM experiments (in situ carburizations)

Samples were prepared by dispersing iron-oxide precursors onto either Au/Pd microgrids[13] (for the non-promoted sample) or 50 mesh 99.997% pure Pt grids[11] (for the potassium promoted sample). Details on the preparation of these grids can be found in Chapter 6.

The initial morphology of the iron-oxide precursors was characterized in 1 Torr nitrogen gas at 150°C prior to the carburization process. 150°C was used to avoid formation of

mobile iron-carbonyl species that might influence our measurements. Three different experiments were performed in which the samples were reacted with carbon monoxide as described in Table 1. In general, reactions with CO gas were performed between 1 and 20 Torr. Since it is not possible to do TEM or EELS measurements at 20 Torr, the pressure was lowered to 1 - 3.5 Torr as indicated in Table 1 prior to data collection.

	Gas	Temperature (°C)*	Pressure (Torr)	Time (min)	cumulative Time (min)	Grid	Stage#	Fe-L_3/L_2 ratio	Fe/O ratio
Experiment 1 0% K2O	N$_2$	150	1	0		Au/Pd	M	5.5	-
	CO	293	1	40	40		RS		
	CO	293	1	60	100		M	4.9	3.6
	CO	400	1	120	220		RS		
	CO	400	1	60	280		M	-	-
	CO	400	1	60	340		RS		
	CO	400	1	75	415		M	-	-
	CO	400	20	120	535		RS		
	CO	400	1	10	545		M	4.6	5.6
Experiment 2 5.4% K2O	N$_2$	150	1	0	0	Pt	M	5.1	2.7
	CO	270	1	60	60		RS	-	-
	CO	270	1	45	105		M	5.2	2.8
	CO	270	20	90	195		RS	-	-
	CO	270	1	20	215		M	4.9	3.2
	CO	270	20	120	335		RS	-	-
	CO	270	1	15	350		M	4.6	3.8
	CO	270	20	120	470		RS	-	-
	CO	270	1	-	470		M	3.1	31.3
	Vacuum	150	0	overnight	490		-	-	-
	CO	400	10	80	490		RS	-	
	CO	400	20	25	615		-	-	-
	CO	400	3.5	20	635		M	2.8	75.0
Experiment 3 5.4% K$_2$O	N$_2$	150	1	0		Pt	M	5.0	3.0
	CO	400	20	120	120		RS	-	-
	CO	400	1	60	180		M	2.8	45
	CO	400	20	60	240		RS	-	-
	CO	400	1	60	300		M	2.7	135

Table 1: T and P sequence using the ETEM;

Typical ramp rates are about 20°C per minute; #M=measurement, RS=reaction step

4.2.4. TEM reference experiments

A reference experiment was performed in the TEM (not the ETEM) by heating the potassium promoted catalyst in vacuum without CO gas (experiment 4). The catalyst was dispersed onto an Au/Pd microgrid and heated as indicated in Table 2.
To study the possible influence of noble metal TEM grids that were used during the ETEM experiments, two quasi in situ experiments were performed.
The in situ conditions were mimicked using a specially designed set-up consisting of a calibrated flow meter, a sealable quartz U-tube and an oven. Either a sample mounted on a TEM grid (experiment 5) or 350 mg iron oxide catalyst powder (experiment 6) was

sandwiched in between quartz-wool at the bottom of the U-tube. The carburization procedure was performed at atmospheric pressure according to the following procedure:

- 5 °C / min to 150°C in nitrogen (flow = 5 ml/min)
- dwell for 5 minutes
- switch to 3% carbon monoxide in nitrogen (flow = 5 ml/min)
- 5°C / min to 270 °C
- dwell for 4 hours
- switch to nitrogen gas (flow = 5 ml/min)
- cool down to room temperature

The U-tube was closed and the sample was transported to a glove-box. To avoid re-oxidation, samples were transferred into the TEM microscope using a special transfer holder[14], avoiding the need for the commonly applied passivation procedure[15].

	Gas	Temperature (°C)	Pressure (Torr)	Time (min)	cumulative Time (min)	Grid	Fe-L_3/L_2 ratio	Fe/O ratio
Experiment 4 5.4% K2O	Vacuum	23	1	0	0	Au/Pd	5.7	2.4
	Vacuum	270	1	150	150		5.2	2.5
	Vacuum	270	1	105	255		5.1	2.5
	Vacuum	400	1	5	260		5.1	2.7
	Vacuum	400	1	25	285		4.9	2.7
	Vacuum	400	1	45	330		4.9	4.1
Experiment 5 5.4% K2O	N$_2$/CO	270	750	240	240	Au/Pd	5.5	2.4
Experiment 6 5.4% K2O	N$_2$/CO	270	750	240	240	none	5.3	2.4

Table 2: experimental details of the reference experiments

4.2.5. X-Ray Diffraction (XRD)

XRD was performed using a Bruker type D8 equipped with a Cu Kα source. Variable (θ-compensating) anti-scatter and divergence slits were used.

4.3.   Results and discussion

4.3.1.   Oxidic precursors

XRD shows both catalyst precursors to consist of the hematite phase [JCPDS#33664; Figure 1].
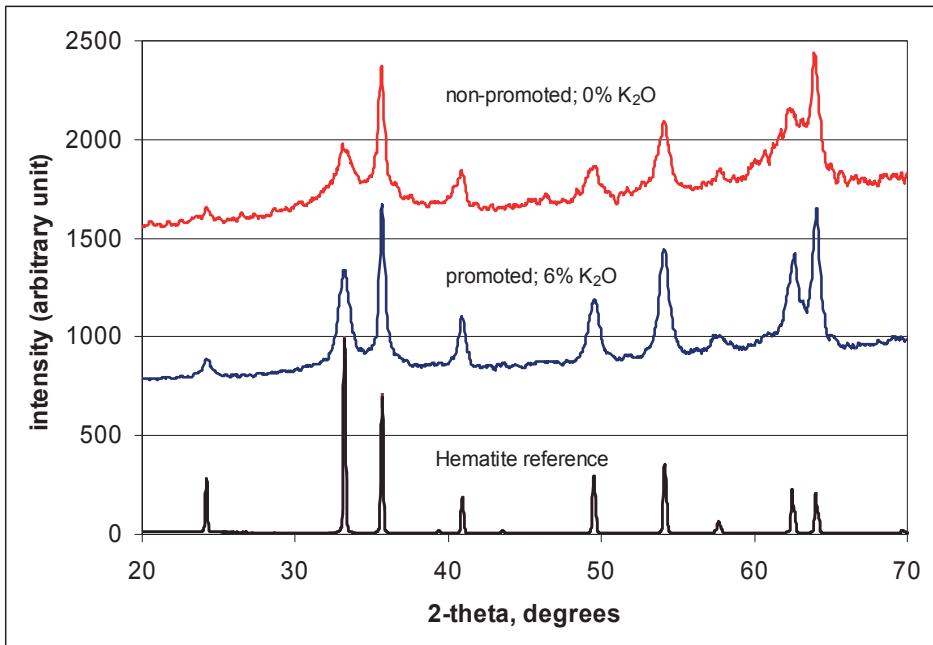
Figure 1: XRD patterns of the catalyst precursors

TEM images of the non-promoted and promoted catalysts are presented in Figure 1a and Figure 1b, respectively. Small iron oxide crystallites are observed (< 50 nm). EELS of both pre-cursor catalysts shows L_3/L_2 ratios of 5.5 and 5.1 respectively (see Table 1), close to a hematite reference value of 5.4[9].
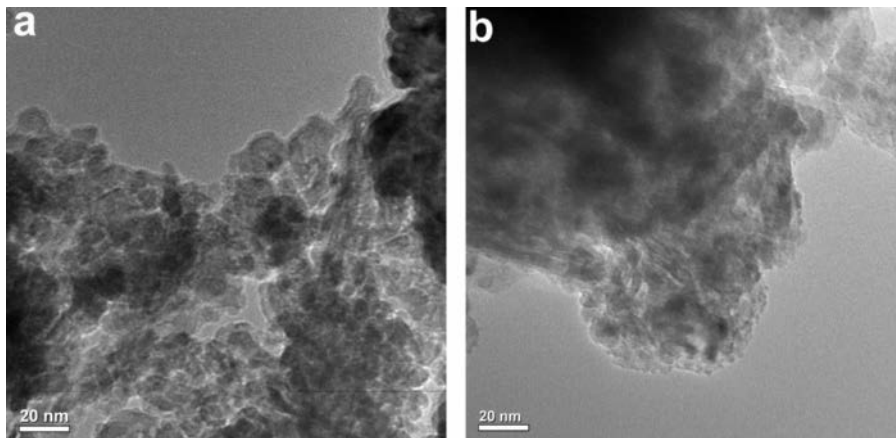
Figure 2: TEM images of non-promoted (a) and promoted (b) catalyst precursors

4.3.2. Experiment 1, in situ carburization of a non-promoted precursor

While under flowing nitrogen (1 Torr pressure), a non-promoted sample was first heated to 150°C inside the microscope. At this stage no CO gas was introduced to avoid formation of volatile iron-carbonyl species (that could possibly change our specimen). After equilibration at 150°C, the flow of nitrogen was stopped and the sample was subjected to 1 Torr CO gas. The temperature was increased to about 293°C. After 195 minutes, no morphological changes were observed visually in TEM (represented by Figure 3a). However, after an additional 120 minutes at 400°C (total t = 545 min), in combination with an increased CO pressure of 20 Torr, major sintering occurred. Figure 3a and Figure 3b show TEM micrographs of the same area before and after sintering.
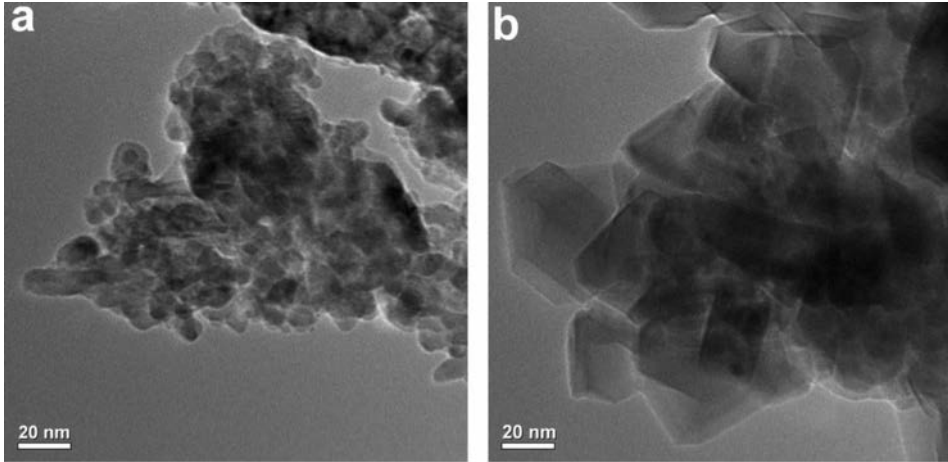
Figure 3: The same area of a non-promoted sample before (a) and after sintering (b)

Note that often stabilizers (such as silica) are added to the catalyst formulation to increase the thermal stability[16]. However, in this model study no stabilizer was used and therefore our samples are likely more prone to sintering.

Next to the morphology, also the chemical composition changed. Based on EEL spectra the iron and oxygen edge areas were determined to calculate the iron L_3/L_2 and iron/oxygen. The data are presented in Table 1 and show the Fe-L_3/L_2 ratio to decrease, indicating a reduction of the iron species. In addition the Fe/O ratio increases, showing oxygen to be removed from the lattice during the procedure. It seems likely to assume that hematite (Fe_2O_3) is reduced to magnetite (Fe_3O_4) consistent with the first step of carburization as previously shown by Li et al.[17]. Surprisingly, this reduction is accompanied by huge sintering even at temperatures much lower than the Tammann temperature[18]. No carbon edges could be found apart from the typical CO signature from CO gas inside the microscope as shown in Figure:
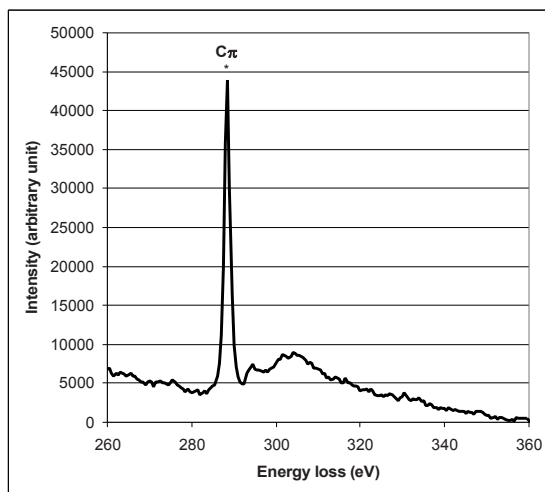
Figure 4: EELS of CO gas inside the microscope

In conclusion, no iron carbides were formed in this 'non-promoted' precursor. Since potassium is a well known promoter to facilitate carburization[19–27] we changed to a potassium-promoted precursor in further experiments.

4.3.3.   Experiments 2 and 3, in situ carburizations of a potassium promoted precursor

For experiment 2, we equilibrated a potassium promoted precursor at 150°C in flowing nitrogen at 1 Torr to avoid any iron carbonyl formation. Subsequently, we switched to 1 Torr of CO gas and began the carburization experiment as summarized in Table 1.
The catalyst precursor consists of small iron oxide crystallites (Figure 2b and 5a). Under influence of 20 Torr CO gas the catalyst starts to sinter as observed in the previous experiment (Figure 5b). After prolonged CO treatment (t = 470 min.), about 50 nm size crystallites grow out of the sintered clusters (Figure 5c). This formation is consistent with previous findings[28]. Further extension of the CO treatment leads to breaking-up of these new crystallites into smaller crystallites of about 5 to 30 nm (t = 635 min; Figure 5d and 5f.). Note that Figure 5e and 5f are magnified areas as indicated in Figure 5c and 5d respectively.
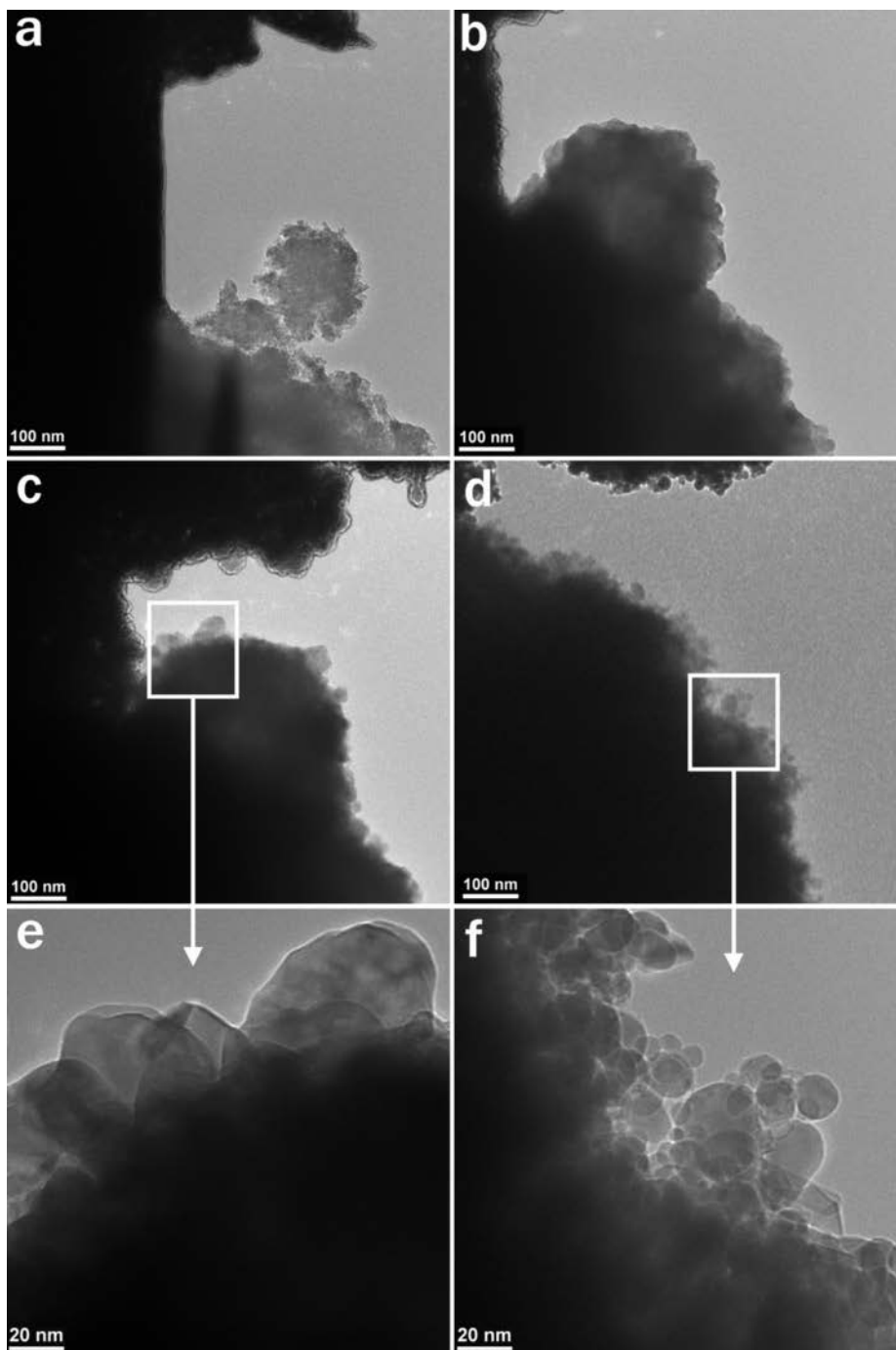
Figure 5: TEM micrographs of experiment 2 after 0 min. (a), 350 min. (b), 470 min. (c, e) and 635 minutes (d,f).

EELS data measured at the various stages of transformation are shown in Figure 6a and Figure 6b. Due to the opaqueness of the sintered particles we only obtained EELS data from the rim of these features. Note that the carbon and potassium edges (Figure 6a) are close together and sometimes difficult to distinguish (C-K edge = 284 eV, K-L_3 edge = 294 eV and K-L_2 edge = 296 eV).

Figure 6: EEL spectra of experiment 2 showing potassium, carbon and nitrogen edges (a) and oxygen and iron edges (b) after 0, 215, 470 and 635 minutes respectively. Data are normalized on the iron edges.

At t=0 minutes, potassium edges are observed close to 300 eV. A contribution close to 400 eV is from the nitrogen gas (N-K edge). Oxygen presence is seen between 525 and 550 eV. The iron L_3/L_2 edge ratio is 5.1 which is typical for hematite[29]. After 215 minutes reaction in CO, a very small C-π^* edge is observed at 287 eV. The potassium contribution is still pronounced as well as the iron oxide features. After 470 minutes the C-π^* edge has increased slightly, indicating a small amount of carbide formation. The potassium edges can still be distinguished while the oxygen contribution is decreasing. The iron L_3/L_2 edge ratio is lowered to 3.1, proving the iron is in a reduced state. However, since the number of electrons in the 3d subshell of iron carbide is the same as in fully reduced iron, it is not possible to distinguish between these species. Nonetheless, since there are only very small carbon and oxygen contributions, we conclude metallic

iron is present (which is thermodynamically possible at these temperatures[30]. This is also confirmed by lattice spacings of 2.02Å, that fit the (110) lattice plane of α-Fe (2.027Å ; JCPD# 6-696) as shown in Figure 7.
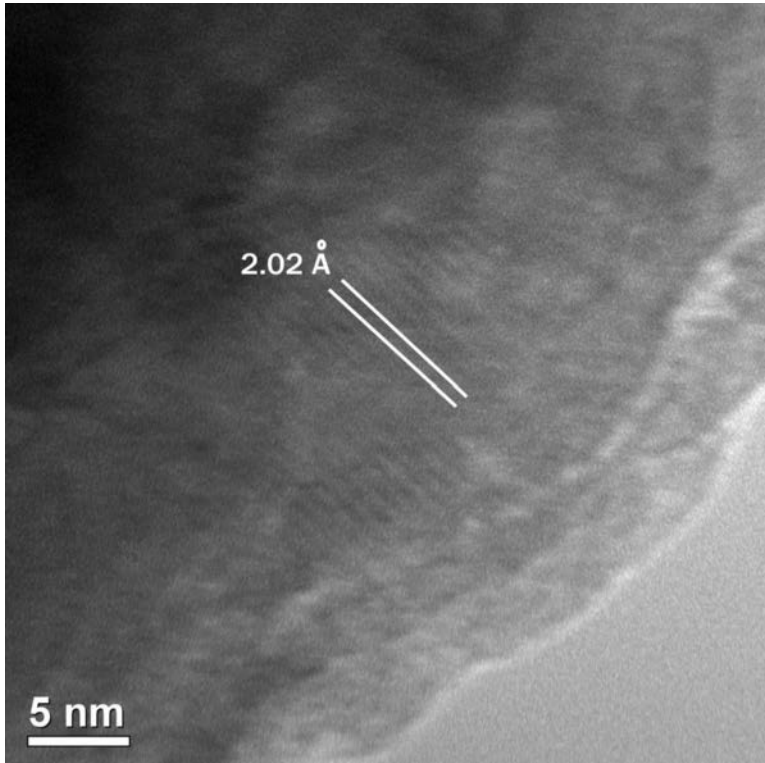
Figure 7: TEM micrograph showing lattice spacings which are consistent with α-Fe

For experiment 3, our potassium promoted precursor was again equilibrated at 150°C in flowing nitrogen to avoid any iron carbonyl formation. Then we switched to CO gas according to Table 1. Note that for this run we increased the temperature to 400°C to speed up the carburization process. In time, again large sintering and iron carbide formation was observed similar as described for experiments 1 and 2. EELS data are presented in Figure 8a and 8b. As can be expected, identical data are obtained as for experiment 2 at the start of the run. After 180 minutes reaction in CO, a very small C-π* edge is observed at 287 eV while the oxygen contribution is minimal. The iron L_3/L_2 edge ratio is lowered to 2.8 proving the iron is in a reduced state. This is a clear indication that at the rim of the sintered particles metallic iron is formed. After 300 minutes a distinct

carbide edge is obtained. The potassium feature is now scavenged by the large carbon contribution. From the iron L_3/L_2 edge ratio of 2.7 we conclude the iron is still in a reduced state.

The results again show that the Fe-L_3/L_2 ratio's decline over time, similar to experiments 1 and 2. The increasing Fe/O ratio (Tabel 1) proves the sample is losing oxygen and iron carbides are formed. Our data show that during these phase changes metallic iron is an intermediate species.
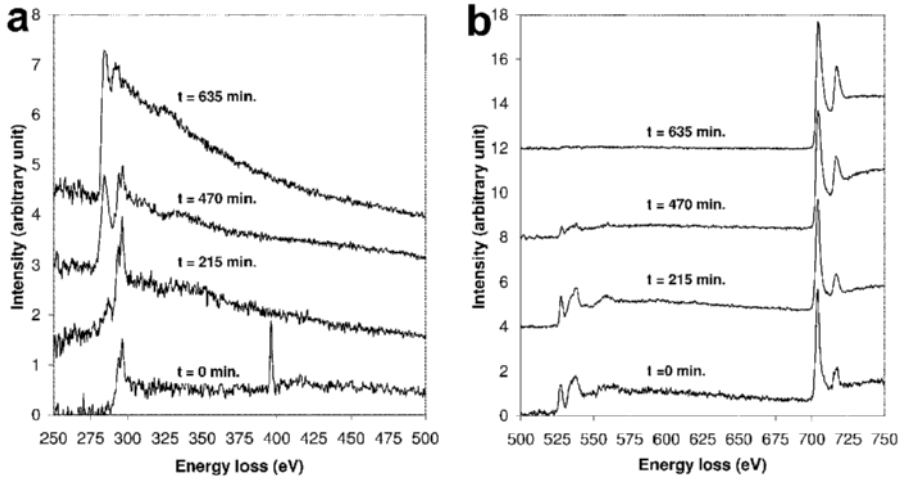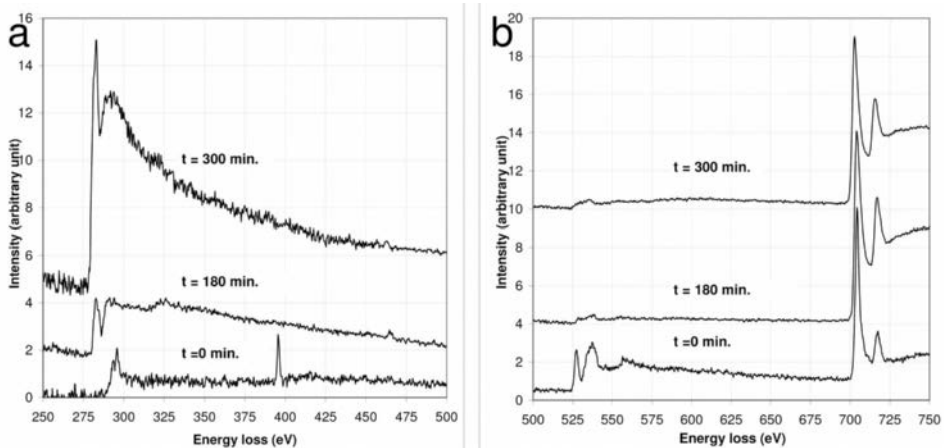

Figure 8: EEL spectra of experiment 3 showing potassium, carbon and nitrogen edges (a) and oxygen and iron edges (b) after 0, 180 and 300 minutes respectively. Data are normalized on the iron edges.

It is known that a combination of low pressure and a reducing gas leads to extensive sintering at temperatures above 800°C[31,32]. Our results show that similar effects can be observed at lower temperatures after prolonged reaction times. Distinct carbide edges are obtained that prove iron carbide formation. Interestingly, no carbon deposits are observed on these iron carbide particles (Figure 5f) as opposed to previous reports that state simultaneous carbon deposition with carbide formation[33]. This discrepancy can be explained if we consider the so called 'competition model'[34]. According to this model, carbon monoxide dissociates and the carbon quickly dissolves into a metallic iron phase. As a result we don't see carbon deposits. Since others usually don't reduce the iron oxide all the way to metallic iron, and this fast dissolution does not occur in iron oxide, it could explain why others do see carbon deposits. However, even when the iron carbides are fully developed (like in Figure 5f) still no amorphous carbon layers are detected. This seems in line with the suggestions made by Jin et al.[29] that carbon layers may be absent

at reaction conditions but are formed during cooling of the sample prior to analyses. In addition, commonly applied passivation procedures might also lead to carbon deposits as we reported previously[9].

The potassium edge is no longer visible due to the large carbon contribution. The iron L3/L2 edge ratio of 2.8 shows the iron is still in a reduced state. Overall, the results show that the Fe-L_3/L_2 ratios decline over time, similar to what was observed in experiment 1. Based on the increasing Fe/O ratio (Table 1), the sample is losing oxygen while carbides are formed.

4.3.4. Experiment 4, in situ heating experiment

The same potassium promoted sample as used in experiments 2 and 3 was heated inside the TEM microscope as indicated in Table 2. In contrast to the previous experiment, the sample was kept in vacuum (1 Torr) and no CO gas was present. During heating to 270°C, the sample is stable and no significant changes are observed. Even after a dwell time of 240 minutes no sintering is observed and the crystallites are similar to the starting material as shown in the next Figure.
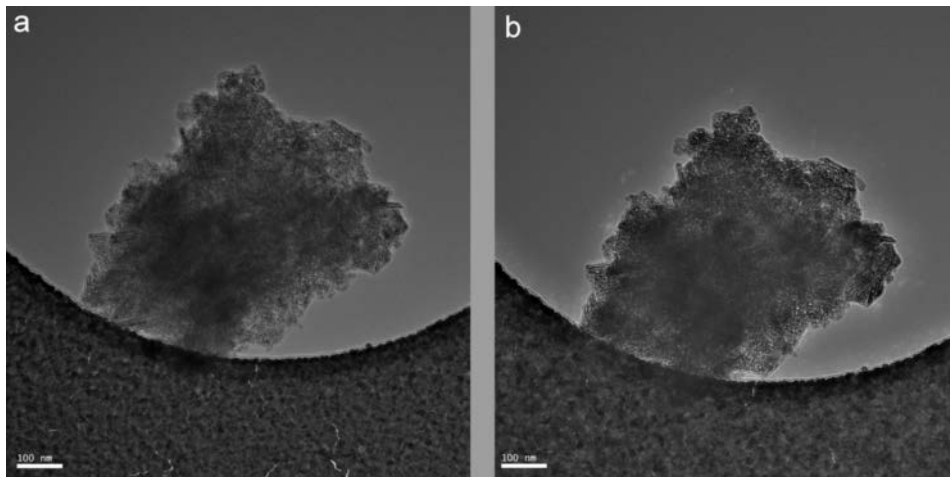
Figure 9: TEM images before (a) and after (b) heating for 240 minutes at 270°C

In addition, the Fe/O ratio remains unchanged. Note that in experiments 1 and 2, this Fe/O ratio increased substantially after a similar reaction time. Only by increasing the temperature to 400°C, some minor coalescence of individual crystallites is observed after 60 minutes. However, the effects are much less pronounced compared to our ETEM experiments with CO.

Overall, these results prove that a combination of low pressure and elevated temperature alone cannot explain the extensive sintering we observed in experiments 1-3.

4.3.5. Experiments 5 and 6, effects of the TEM grid

Two experiments were performed in order to discover the possible effects of the noble metal TEM grid on the sintering behavior. Potassium promoted samples were carbided in a diluted stream of CO gas with and without a TEM grid present (experiment 5 and 6 respectively).

TEM micrographs of both experiments are shown in Figure 10. It shows that, irrespective of whether a grid is present or not, similar results are obtained (compare Figure 10a with Figure 10b). After treatment, the bulk of the materials still consists of small crystallites similar to the starting material. Also, the iron L_3/L_2 edge- and Fe/O ratios remain virtually unchanged after treatment (see Table 2). Some minor sintering is observed, as indicated by the arrows in Figure 10. Nevertheless, it is in no way comparable to the extensive sintering that was observed in experiments 1-3.

Based on these results we can conclude that the TEM grids themselves do not play any significant role in the sintering of our catalyst precursors.
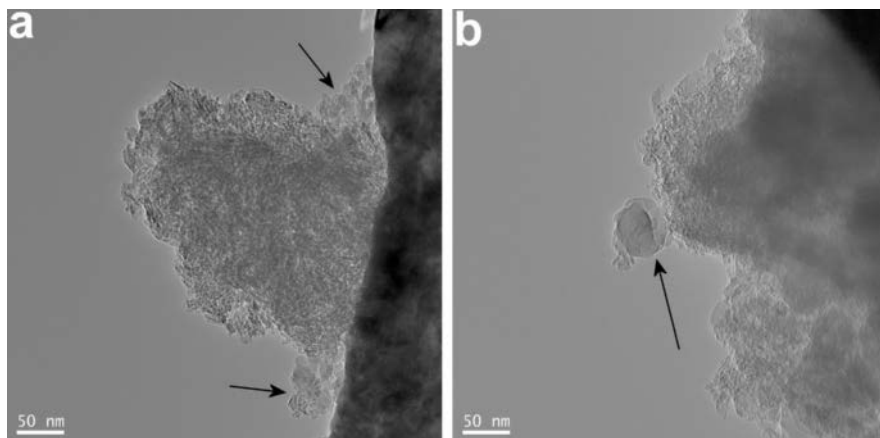
Figure 10: carbided samples while mounted on a grid (a) and without any grid present (b).

4.4. Conclusions

During carburization inside an ETEM at 20 Torr CO, hematite containing precursors are reduced. During, or shortly after, this reduction huge sintering occurs. We proved that this sintering is enhanced by low pressure conditions in combination with CO gas. Since the oxygen removal during the decomposition of iron oxide is improved in vacuum, we conclude that this process is diffusion limited. The role of CO gas is to react with the oxygen forming CO2. In all, our results show that this process is very pressure dependent.

Based on the increasing Fe/O ratio, we conclude that further reduction takes place with longer reaction times. The reduction inside the ETEM is so effective that metallic iron can be formed. Eventually, about 50 nm size crystallites grow out of the iron (oxide) particles. In time, these newly formed crystallites reduce in size to about 5-30 nm. EELS proves these features are iron carbides.

In contrast to literature data published so far, we found no carbon deposits on the outer rim of the iron carbides at high temperature conditions (experiment 2). Note however, that all previous studies involve catalysts that are cooled prior to analysis. During this cooling, carbon deposits could have been formed. In addition, many available studies are performed on passivated samples. We have shown previously that this passivation can also lead to carbon deposits. Overall, more study is required to elucidate the exact mechanism. The new challenge will be to perform in situ TEM studies at even higher pressures than what is possible today.

4.5. References

1.   Le Caër, G., Dubois, J. M., Pijolat, M., Perrichon, V. & Bussiere, P. Characterization by Moessbauer spectroscopy of iron carbides formed by Fischer-Tropsch synthesis. *J. Phys. Chem.* **86,** 4799–4808 (1982).

2.   Bukur, D. B. *et al.* Activation Studies with a Precipitated Iron Catalyst for Fischer-Tropsch Synthesis. *J. Catal.* **155,** 353–365 (1995).

3.   O'Brien, R. J. *et al.* Activity and selectivity of precipitated iron Fischer-Tropsch catalysts. *Catal. Today* **36,** 325–334 (1997).

4.   Davis, B. H. Fischer-Tropsch synthesis: relationship between iron catalyst composition and process variables. *Catal. Today* **84,** 83–98 (2003).

5.   Jung, H. & Thomson, W. J. Dynamic x-ray diffraction study of an unsupported iron catalyst in Fischer-Tropsch synthesis. *J. Catal.* **134,** 654–667 (1992).

6.   Jung, H. & Thomson, W. J. Dynamic x-ray diffraction study of an unreduced iron oxide catalyst in Fischer-Tropsch synthesis. *J. Catal.* **139,** 375–382 (1993).

7.   Li, S. *et al.* Structural analysis of unpromoted Fe-based Fischer-Tropsch catalysts using X-ray absorption spectroscopy. *Appl. Catal., A* **219,** 215–222 (2001).

8.   Hansen, T. W. & Wagner, J. B. Catalysts under Controlled Atmospheres in the Transmission Electron Microscope. *ACS Catal.* **4,** 1673–1685 (2014).

9.   Janbroers, S., Zandbergen, H. W., Louwen, J. N. & Kooyman, P. J. Insights into the nature of iron-based Fischer–Tropsch catalysts from quasi in situ TEM-EELS and XRD. *J. Catal.* **268,** 235–242 (2009).

10.   Boyes, E. D. & Gai, P. L. Environmental high resolution electron microscopy and applications to chemical science. *Ultramicroscopy* **67,** 219–232 (1997).

11.   Li, P., Liu, J., Nag, N. & Crozier, P. A. In situ synthesis and characterization of Ru promoted Co/Al2O3 Fischer-Tropsch catalysts. *Appl. Catal., A* **307,** 212–221 (2006).

12.   Mitchell, D. R. G. Measure EELS Peak Intensities script version 2.1, http://www.felmi-zfe.tugraz.at/dm_scripts/http://www.felmi-zfe.tugraz.at/dm_scripts/. (2006).

13.   Janbroers, S., Zandbergen, H. W., de Kruijff, T. R., Xu, Q. & Kooyman, P. J. Preparation of carbon-free TEM microgrids by metal sputtering. *Ultramicroscopy* **109,** 1105–9 (2009).

14.   Zandbergen, H. W., Kooyman, P. J. & an Langeveld, A. D. Electron Microscopy 1998, proceedings ICEM 14. in *Electron Microscopy 1998, proceedings ICEM 14* **II,** 491–492 (1998).

15.   Shroff, M. D. & Datye, A. K. The importance of passivation in the study of iron Fischer-Tropsch catalysts. *Catal. Lett.* **37,** 101–106 (1996).

16.   Bukur, D. B., Koranne, M., Lang, X., Rao, K. R. P. M. & Huffman, G. P. Pretreatment effect studies with a precipitated iron Fischer-Tropsch catalyst. *Appl. Catal., A* **126,** 85–113 (1995).

17.   Li, S., Ding, W., Meitzner, G. D. & Iglesia, E. Spectroscopic and Transient Kinetic Studies of Site Requirements in Iron-Catalyzed Fischer-Tropsch Synthesis. *J. Phys. Chem. B* **106,** 85–91 (2002).

18.   Tomohiro, A., Hiromichi, O., Reijiro, T., Yoshio, W. & Jun-ichiro, Y. Measurement and Modeling of Thermal Conductivity for Dense Iron Oxide and Porous Iron Ore Agglomerates in Stepwise Reduction. *ISIJ* **32,** 829–837 (1992).

19.   Koelbel, H. & Giehring, H. The action of alkali promoters upon iron catalysts. VI. Influence of potassium carbonate upon selectivity. I. *Brennst.-Chem.* **44,** 343–347 (1963).

20.   Dictor, R. A. & Bell, A. T. A comparison of the activity, selectivity and kinetics of several iron-based Fischer-Tropsch catalysts. *Prepr. - Am. Chem. Soc., Div. Pet. Chem.* **31,** 126–132 (1986).

21.   Dictor, R. A. & Bell, A. T. Fischer-Tropsch synthesis over reduced and unreduced iron oxide catalysts. *J. Catal.* **97,** 121–136 (1986).

22.   Eliason, S. A. & Bartholomew, C. H. Kinetics and deactivation of unpromoted and potassium-promoted iron Fischer-Tropsch catalysts at low pressure (1 atm). *Stud. Surf. Sci. Catal.* **68,** 211–218 (1991).

23.   O'Brien, R. J. *et al.* Fischer-Tropsch synthesis: impact of potassium and zirconium promoters on the activity and structure of an ultrafine iron oxide catalyst. *Top. Catal.* **2,** 1–15 (1995).

24.   Raje, A. P., O'Brien, R. J. & Davis, B. H. Fischer-Tropsch synthesis with coal derived syngas. *Proc. - Annu. Int. Pittsburgh Coal Conf.* **15th,** 106–123 (1998).

25.   Raje, A. P., O'Brien, R. J. & Davis, B. H. Effect of potassium promotion on iron-based catalysts for Fischer-Tropsch synthesis. *J. Catal.* **180,** 36–43 (1998).

26.   Bartholomew, C. H., Datye, A. K., Mansker, L. D. & Stoker, M. W. Effects of pretreatment, reaction, and promoter on microphase structure and Fischer-Tropsch activity of precipitated iron catalysts. *Stud. Surf. Sci. Catal.* **126,** 265–272 (1999).

27.   Wan, H., Zhang, C.-H., Wu, B., Xiang, H.-W. & Li, Y. Promotional effects of Cu and K on precipitated iron-based catalysts for Fischer-Tropsch synthesis. *J. Mol. Catal. A* **283,** 33–42 (2008).

28.   Shroff, M. D. *et al.* Activation of precipitated iron Fischer-Tropsch synthesis catalysts. *J. Catal.* **156,** 185–207 (1995).

29.   Jin, Y., Xu, H. & Datye, A. K. Electron Energy Loss Spectroscopy (EELS) of Iron Fischer-Tropsch Catalysts. *Microsc. Microanal.* **12,** 124–134 (2006).

30.   Mondal, K., Lorethova, H., Hippo, E., Wiltowski, T. & Lalvani, S. B. Reduction of iron oxide in carbon monoxide atmosphere--reaction controlled kinetics. *Fuel Process. Technol.* **86,** 33–47 (2004).

31.   Nobuhito, K., Mitsuo, O. & Akio, H. Process for producing sintered ferrous alloys. **US4614638,** (1986).

32.   L'vov, B. V. Mechanism of carbothermal reduction of iron, cobalt, nickel and copper oxides. *Thermochim. Acta* **360,** 109–120 (2000).

33.   Jin, Y. & Datye, A. K. Phase transformations in iron Fischer-Tropsch catalysts during temperature-programmed reduction. *J. Catal.* **196,** 8–17 (2000).

34.   Niemantsverdriet, J. W. & Kraan, A. M. van der. On the time-dependent behavior of iron catalysts in Fischer-Tropsch synthesis. *J. Catal.* **72,** 385–388 (1981).

5

CSTR testing of FT slurry catalysts

In previous chapters, different model studies have been presented on a variety of catalysts. In this chapter, test results of these catalysts are presented using typical Fischer-Tropsch reaction conditions. The tests have been performed at the Centre of Applied and Energy Research (CAER) of Kentucky University in Lexington, Kentucky, USA.

The experiments were partially done for other purposes that cannot be disclosed in this thesis. As a result, the data obtained are not suitable for kinetic studies since only fixed test conditions were used. Nevertheless, the results will show the catalysts are suitable for, and active in Fischer-Tropsch synthesis.

5.1   Introduction

The Fischer-Tropsch process produces linear hydrocarbons by reacting CO and H_2 according to:

$$nCO + 2nH_2 \leftrightarrow [-CH2-]n + nH_2O \qquad\qquad\qquad (eq.\ 1)$$

where 'n' is the chain length of the hydrocarbon formed. It typically ranges from 1 up to 100, depending on the catalyst type and testing conditions. The theoretical chain length distribution of the produced hydrocarbons in the Fischer-Tropsch process is described by the Anderson-Schulz-Flory (ASF) distribution (as also explained in Chapter 1):

$$Wn = n\ (1-\alpha)^2 * \alpha^{(n-1)} * 100 \qquad\qquad\qquad (eq.\ 2)$$

where 'n' is the chain length and 'Wn' is the wt% of the respective hydrocarbons produced. The ASF distribution is a function of alpha (α). A higher alpha means longer hydrocarbon chains. An example of the theoretical chain length distribution according to ASF for alpha = 0.88 is given in Figure 5.1.1:
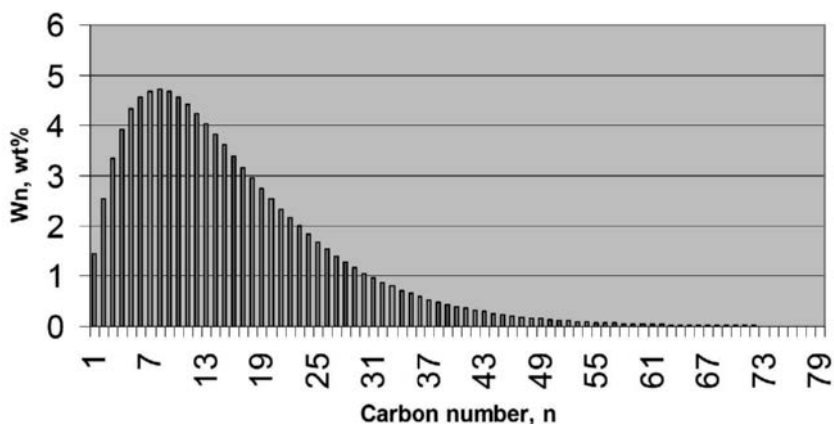
Figure 5.1.1: ASF example, alpha = 0.88

Typically, α is calculated using the ASF distribution by plotting the chain length 'n' versus the Log(Wn/n), as depicted in Figure 5.1.2. α can be calculated from the slope of the resulting line according to: $\log \frac{K_n}{W}() \quad W\log = G\left(-\log \frac{+G^2}{G}\right.$ (eq. 3)
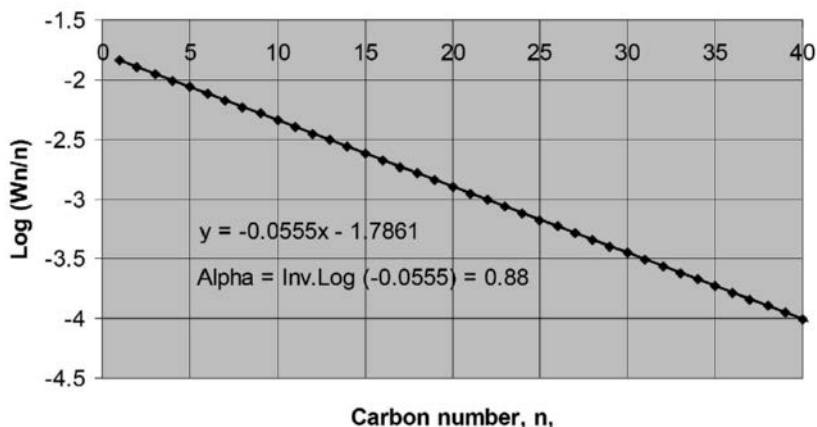
Figure 5.1.2: Carbon number (n) v.s. Log (Wn/n)

Longer chain hydrocarbons are typically indicated by the term 'wax', although this is ill defined. In general, it refers to fractions that are solid at room temperature.

Additional hydrogen is produced by reaction of CO and water, the so called water-gas-shift (WGS) reaction:

$H_2O + CO \leftrightarrow H_2 + CO_2$ (eq. 4)

Note that due to the WGS reaction, a syngas with a relatively low H_2/CO ratio can be used. Such syngas is typically obtained from coal or biomass gasification[1]. The downside however, is that a substantial amount of CO is converted into CO_2, making the iron based Fischer-Tropsch process less carbon-efficient.

The rate the of WGS reaction is defined as the rate of CO_2 formation (in mole CO_2^{-1} h^{-1} g^{-1}). The reaction is in itself dependent on the H_2O formed during the FT reaction. As a consequence, the rate of WGS (r_{WGS}) can never exceed the rate of FT (r_{FT}). The WGS equilibrium constant is highly dependent on temperature. Based on tabulated thermodynamic data, the following expression has been derived[2]:

$$\log S_{KPC}() \ + 2.4198 - 0.0003855\,\alpha \ -\frac{2180.6}{\alpha} \qquad\text{(eq. 5)}$$

where *K* is the WGS equilibrium constant.

From test data, the WGS equilibrium can be calculated as follows:

$$S_{KPC}) \ \frac{O\,HT_2\,On_{\,2}}{O\,HT\ On_{\,2}\,T} \qquad\text{(eq. 6)}$$

The experimental data in which these calculations are used are shown in the next paragraph.

5.2   Experimental

5.2.1   Catalyst preparation

Preparation details of the catalysts are described in more detail in chapters 2 and 3. The preparation technique is based on precipitation which is still the most common manner on commercial scale[3]. The main differences between the samples are the type of promoter metal in combination with the preparation procedure. A distinction can be made between non-copper and copper containing catalysts. An overview is shown in the next Table:

Sample	Promoter addition via	CuO (wt%)	K₂O (wt%)	Chapter	Notations
1	-	0.0	0.0	5	S-Cu0.0K0.0
2	spray drying	0.0	5.4	5	S-Cu0.0K5.4
3	spray drying	0.8	0.8	2, 4	S-Cu0.8K0.8
4	impregnation	0.8	0.8	2	I-Cu0.8K0.8

Tabel 5.2.1: sample compositions (Notations indicates 'S'=spray-dried, 'I'= impregnated, 'Cu'= CuO content in wt%, 'K'=K_2O content in wt%)

5.2.2   Testing

Catalyst evaluations were performed at the Center for Applied Energy Research (CAER) in Kentucky (USA) in a Fischer-Tropsch application. A 1 liter continuously stirred tank reactor (CSTR) was used in this study as shown in Figure 5.2.1.
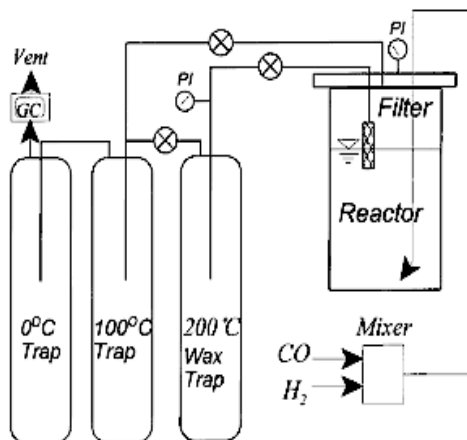
Figure 5.2.1: CAER unit

CO and H_2 mass flow controllers were used to provide synthesis gas of the desired composition. During the reaction, longer chain hydrocarbons are produced that form a wax. To extract wax samples from the catalyst slurry during the process, a metal filter of 2μm was installed. The wax samples were extracted and separated from the catalyst through this filter and collected in a hot trap operated at 200°C. As catalyst fines will pass through this filter as well, some catalyst is inevitably lost during sampling. Since active catalyst is being removed, this will influence the actual test results. Therefore we weighed the catalyst loss and corrected for this in our calculations.

A warm trap (at 100 °C) and cold trap (at 0 °C) were used to collect light wax and water on a daily basis. The non-condensable tail gas from the cold trap was analyzed with an online HP Quad Series Micro GC, providing molar compositions of C1–C7 olefins and paraffins as well as for H_2, CO, and CO_2 (Column 1: 10 m 0.32 mm ID, 30 μm film molecular sieve 5A isothermal at 110°C; Column 2: 8 m 0.32 mm ID, 10 μm film, Pora Plot U, isothermal at 80°C; Column 3:10 m 0.32 mm ID, 8 μm film alumina isothermal at 140°C; Column 4: 10 m 0.15 mm ID, 2 μm film OV-1 isothermal at 120°C.). Hydrogen and carbon monoxide conversions were calculated based on the gas product GC analysis results and the gas flow measured at the reactor outlet.

The non-copper promoted and copper promoted catalysts were each tested under typical conditions[4]. Details are as follows:

Non-copper promoted catalysts

Catalysts were pretreated with 24 nl/h CO at 270 °C at 1.2MPa for 24 hours. The CO flowed through a catalyst slurry containing 20 g (d.b.) catalyst and 280 g polywax C-30 (as a starting liquid). After the catalysts were activated with CO, syngas was introduced at a rate of 3.1 nl/h/g Fe. The feed composition was 41.2 vol% H_2 / 58.8 vol% CO. Reaction conditions were 230 °C, 1.2MPa and a stirrer speed of 750 rpm.

Copper promoted catalysts

8.0 g of Fe-FT catalyst was dosed into a 1 liter CSTR reactor, together with 310 g of C-30 oil. The catalysts were pretreated with 20 nl/h syngas with a molar H_2/CO ratio of 1.4 at 275°C and 1.1MPa for 6 hours. The feed composition was 9.1 vol% N_2 / 53.0 vol% H_2 / 37.9 vol% CO. After completion of the activation, the syngas was introduced at a rate of 3.5 nl/h/g Fe. The feed composition was 9.1 vol% N_2 / 39.6 vol% H_2 / 51.4 vol% CO. Reaction conditions were 255 °C, 3.0MPa and a stirrer speed of 750 rpm.

5.3   Results and discussion

5.3.1   Test results on non-copper catalysts:

The effect of potassium promotion was measured by comparing a completely promoter free sample, S-Cu0.0K0.0, with a potassium promoted sample S-Cu0.0K5.4. An overview of the test data obtained is shown in Table 5.3.1. As can be envisaged, the omission of copper (or similar promoter) leads to rather low activity compared to the state of the art catalysts[5]. In Figure 5.3.1, the conversion data is plotted for both catalysts.
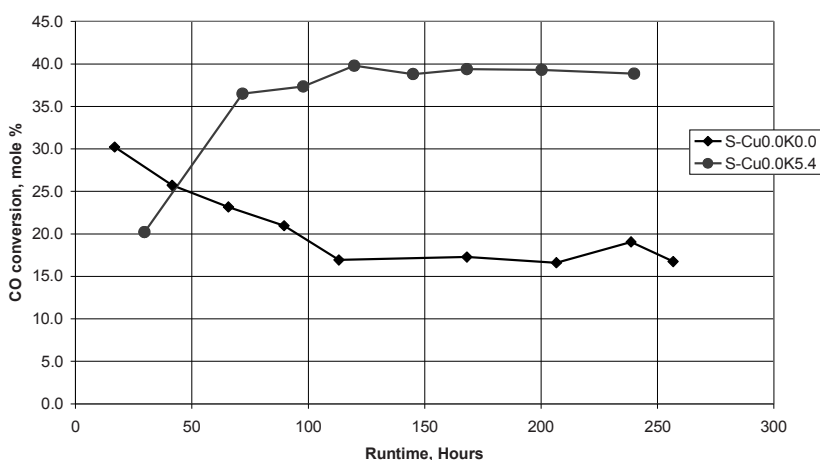
Figure 5.3.1: CO conversion

As can be seen, the CO conversion declines during the first 100 hours for sample S-Cu0.0K0.0 and then seems to stabilize. The potassium-promoted sample shows a different behavior in which the CO conversion is increased during the first 100 hours.

It is known that potassium promoted catalysts have an induction period in which the catalyst becomes more active[6]. It is reasonable to assume that during this period phase changes take place although the bulk composition proved not to be the dominant factor. Compared to the non-promoted catalyst S-Cu0.0K0.0, potassium enhances CO conversion considerably. This is in line with previous findings as reported by Raje et al.[7]. Potassium also increases the alpha value. In fact, during the test period of 240 hours, the alpha value increased from 0.78 to 0.85. This is common for alkali metals, especially potassium. Overall, the data we found are in line with an elaborated study performed by Luo et al.[8]
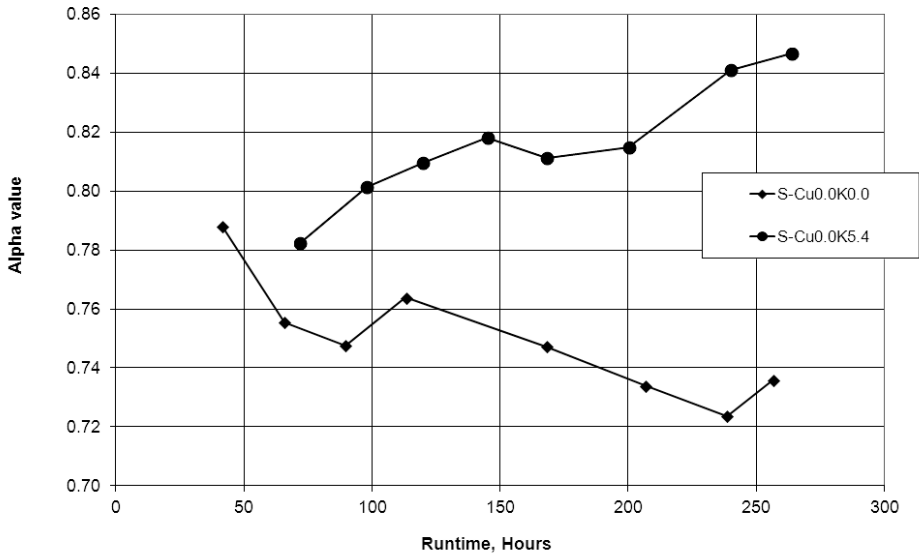
Figure 5.3.2: Alpha value

As can be deduced from Table 5.3.1, the H_2/CO usage significantly differs between the two samples. This can be explained by a higher WGS activity in case potassium is added as a promoter. In WGS, hydrogen is formed at the expense of CO. This leads to a lower H_2/CO usage in case potassium is added as shown in Figure 5.3.3. Based on the WGS reaction, CO_2 formation increases as can be seen in Figure 5.3.4.

As stated above, the WGS rate is dependent on the water formed during the FT reaction. Based on the r_{WGS} / r_{FT} ratio (Table 5.3.1), it is clear the FT rate dominates the WGS rate and therefore WGS is not rate limiting in these tests.

	alpha	TOS	Syngas conv.	K WGS	H_2/CO Usage	CH_4 Rate	FT rate	CO_2 Rate	r WGS / r FT	CO_2 selectivity	CH_4 selectivity
		hours	%			moles/h/g	moles/h/g	moles/h/g		mole%	mole%
S-Cu0.0K0.0	0.79	42	30.6	0.6	1.0	0.0006	0.011	0.003	0.31	23.8	5.0
	0.76	66	27.7	0.2	1.0	0.0005	0.010	0.003	0.27	21.2	5.1
	0.75	90	25.1	0.2	1.0	0.0005	0.009	0.002	0.22	18.4	5.0
	0.76	113	20.8	0.2	1.1	0.0004	0.007	0.002	0.27	21.2	6.2
	0.75	168	20.5	0.2	1.0	0.0004	0.008	0.002	0.20	16.4	5.4
	0.73	207	19.1	0.2	1.0	0.0004	0.007	0.001	0.18	15.2	5.3
	0.72	239	20.9	0.2	0.9	0.0003	0.008	0.001	0.14	12.2	4.2
	0.74	257	18.7	0.2	0.9	0.0003	0.007	0.001	0.16	14.0	4.9
S-Cu0.0K5.4	0.78	30	16.9	1.0	0.4	0.0002	0.007	0.004	0.63	38.6	3.2
	0.80	72	33.2	1.9	0.5	0.0002	0.012	0.007	0.58	36.5	1.8
	0.81	98	33.6	1.8	0.5	0.0002	0.011	0.007	0.64	39.2	1.8
	0.82	120	35.9	1.9	0.5	0.0002	0.012	0.007	0.62	38.3	1.6
	0.81	145	34.8	2.0	0.5	0.0002	0.011	0.008	0.69	40.8	1.7
	0.81	168	35.3	2.1	0.5	0.0002	0.011	0.008	0.69	40.8	1.6
	0.84	200	35.3	2.0	0.5	0.0002	0.011	0.008	0.66	39.9	1.5
	0.85	240	34.0	2.2	0.5	0.0002	0.009	0.007	0.81	44.6	1.9

Table 5.3.1: Test data on 'non-copper' catalysts
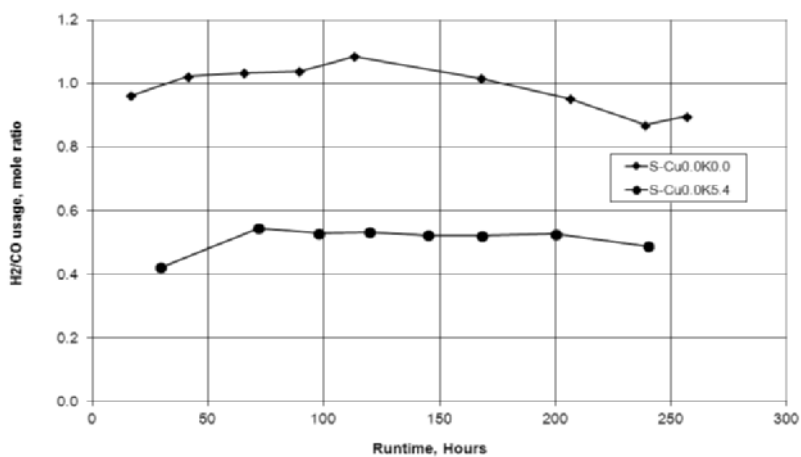
Figure 5.3.3: H_2/CO usage
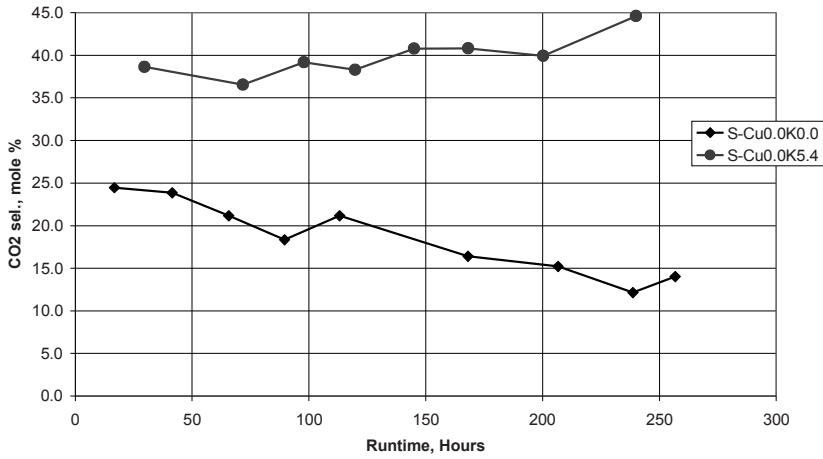
Figure 5.3.4: CO$_2$ selectivity (mole %)

By adding an alkali like potassium, the catalyst surface becomes more basic compared to a non-promoted sample. This increase in basicity leads to a lower methane selectivity as shown previously already by Ngantsoue-Hoc et al.[9] Our data shows the methane selectivity drops from about 5 mole% to below 2 mole% comparing a potassium versus non-potassium containing sample (see Figure 5.3.5).
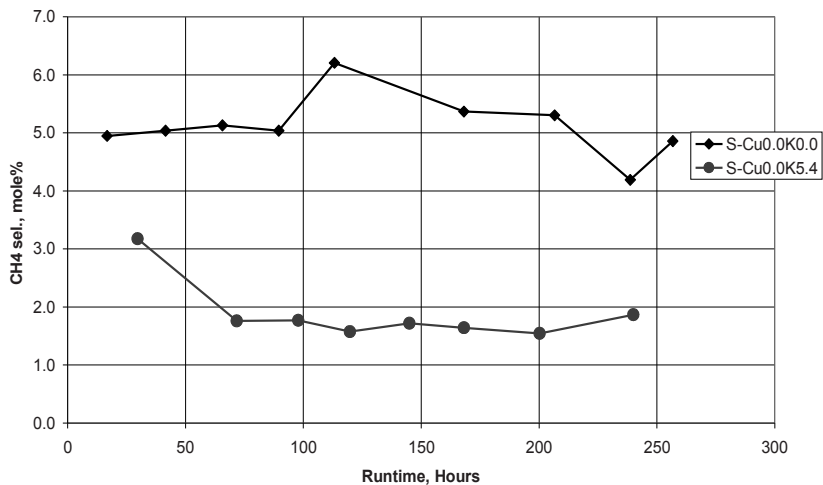
Figure 5.3.5: CH$_4$ selectivity (mole %)

CSTR TESTING OF FT SLURRY CATALYSTS

Alkene selectivity

As has been published before[7,10,11], the alkene selectivity is strongly dependent on the carbon number. It was shown that secondary hydrogenation reactions play a major role in ethene. The alkene fraction depends on both alkali content and on CO conversion, with CO conversion having a greater impact than alkali content. C_3-alkenes proved to be only little dependent on CO conversion or alkali content while it is almost insignificant for C_4 and C_5-alkenes.

GC analyses data, as presented in Table 5.3.2, show our data fits these conventions. The propylene fractions of both samples are close to 0.8, despite the big differences in both CO conversion and potassium content. Note that the absolute value of 0.8 is similar to what has been published before on propylene [7]. For ethene the differences are much larger. This is partly due to the difference in CO conversion. In general, at higher CO conversion, lower ethene concentrations are found.

By comparing our samples, it is clear that potassium has a very big effect. Potassium suppresses the hydrogenation reaction[12] leading to a higher ethene fraction.

	TOS	ethane	ethene	ethene fraction	propane	propylene	propylene fraction
	hours	mole%	mole%	-	mole%	mole%	-
S-Cu0.0K0.0	42	0.203	0.157	0.436	0.105	0.465	0.816
	66	0.198	0.194	0.495	0.110	0.392	0.781
	90	0.179	0.166	0.481	0.101	0.342	0.772
	113	0.154	0.104	0.403	0.097	0.303	0.757
	168	0.143	0.091	0.389	0.093	0.272	0.745
	207	0.148	0.088	0.373	0.087	0.247	0.740
	239	0.141	0.116	0.451	0.089	0.234	0.724
	257	0.139	0.082	0.371	0.080	0.224	0.737
Avg.	-	0.163	0.125	**0.425**	0.095	0.310	**0.759**
S-Cu0.0K5.4	30	0.022	0.125	0.850	0.020	0.117	0.854
	72	0.033	0.207	0.863	0.049	0.214	0.814
	98	0.034	0.219	0.866	0.037	0.231	0.862
	120	0.031	0.226	0.879	0.064	0.227	0.780
	145	0.033	0.226	0.873	0.053	0.235	0.816
	168	0.033	0.268	0.890	0.051	0.235	0.822
	200	0.032	0.257	0.889	0.060	0.226	0.790
	240	0.034	0.201	0.855	0.071	0.246	0.776
Avg.	-	0.032	0.216	**0.871**	0.051	0.216	**0.814**

Tabel 5.3.2: tail gas composition

5.3.2 Test results on copper containing catalysts:

An overview of the test results of the copper containing samples is shown in Table 5.3.3. The catalysts show a high CO conversion under the conditions applied as depicted in Figure 5.3.6. After the 24 hour activation procedure, both catalysts run very stable. The differences between the catalysts are minimal, indicating that the way the promoters are added (either by spray-drying or impregnation) does not make a difference.
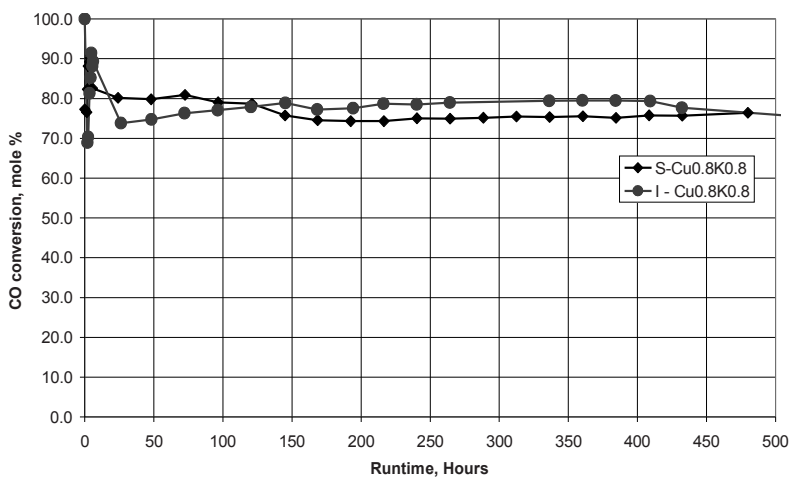
Figure 5.3.6: CO conversion

The alpha values obtained are in line with typical copper-promoted catalysts[13]. Overall, these copper containing samples run at a higher conversion level compared to the non-copper samples as described in the previous paragraph.

Similar to the potassium promoted sample described in §5.3.1, the H_2/CO usage is much lower than 1 indicating a substantial WGS activity (see Figure 5.3.7). As a result, a high amount of CO_2 formation is expected which is the case as shown by Figure 5.3.8. Based on the r_{WGS} / r_{FT} ratio (Table 5.3.3), we can conclude that the FT rate still dominates the WGS rate. In other words, like our non-copper samples, the WGS reaction is not rate limiting.

Figure 5.3.7: H₂/CO usage

Figure 5.3.8: CO₂ selectivity

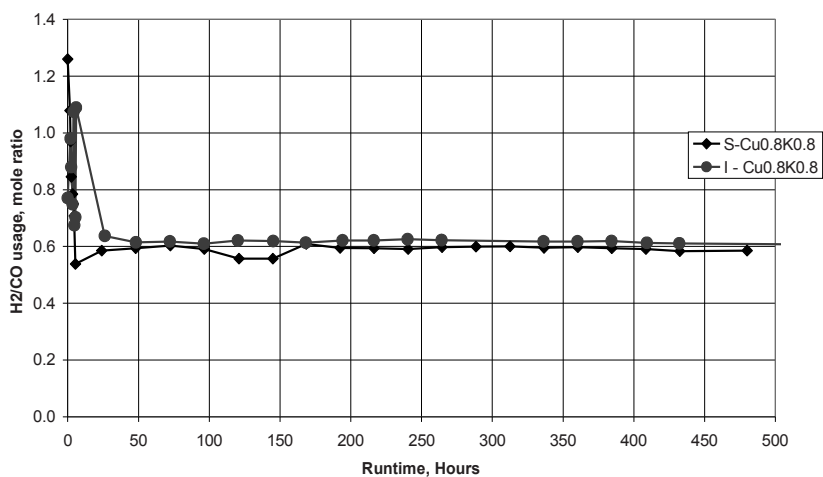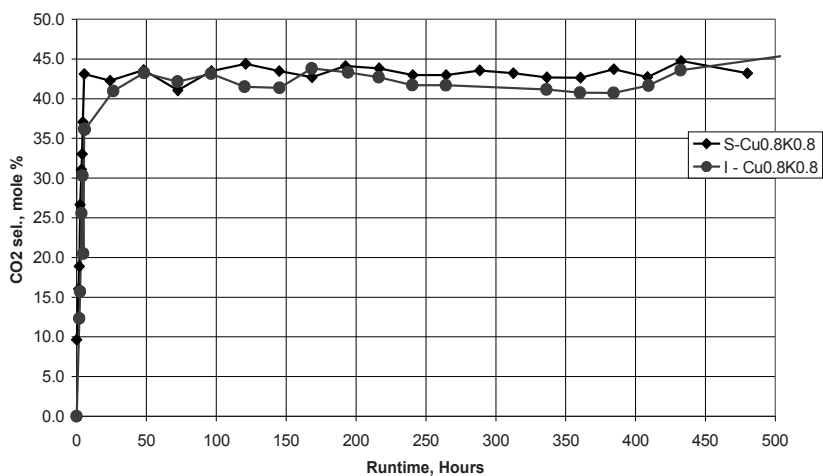|	alpha	TOS hours	Syngas conv. %	K WGS	H_2/CO Usage	CH_4 Rate moles/h/g	FT rate moles/h/g	CO_2 Rate moles/h/g	r WGS / r FT	CO_2 selectivity mole%	CH_4 selectivity mole%
S-Cu0.8K0.8	0.86	24	71.8	10.2	0.6	0.0005	0.028	0.020	0.73	42.3	1.8
	0.86	48	71.9	11.2	0.6	0.0005	0.027	0.021	0.77	43.6	1.9
	0.86	73	73.3	11.5	0.6	0.0005	0.028	0.020	0.70	41.0	1.8
	0.87	97	71.1	10.5	0.6	0.0005	0.027	0.020	0.77	43.5	2.0
	0.86	121	69.2	10.8	0.6	0.0006	0.026	0.021	0.80	44.4	2.2
	0.85	145	66.6	9.7	0.6	0.0005	0.025	0.020	0.77	43.5	2.1
	0.85	169	67.8	9.5	0.6	0.0005	0.025	0.019	0.75	42.7	1.8
	0.87	193	67.0	9.9	0.6	0.0005	0.025	0.020	0.79	44.1	1.9
	0.86	217	66.9	9.8	0.6	0.0005	0.025	0.019	0.78	43.8	1.9
	0.86	241	67.4	9.9	0.6	0.0005	0.025	0.019	0.75	43.0	1.9
	0.86	265	67.7	10.1	0.6	0.0005	0.025	0.019	0.75	43.0	1.9
	0.86	289	67.9	9.6	0.6	0.0005	0.025	0.020	0.77	43.6	1.9
	0.86	313	68.3	10.8	0.6	0.0005	0.026	0.019	0.76	43.2	1.9
	0.86	337	67.9	10.5	0.6	0.0005	0.026	0.019	0.74	42.7	1.8
	0.87	361	68.2	10.6	0.6	0.0005	0.026	0.019	0.74	42.7	1.8
	0.87	385	67.6	9.6	0.6	0.0005	0.025	0.020	0.78	43.7	1.9
	0.86	409	68.1	11.5	0.6	0.0005	0.026	0.019	0.75	42.7	1.9
	0.86	433	67.7	5.8	0.6	0.0005	0.025	0.020	0.81	44.7	2.0
	0.86	480	68.5	12.0	0.6	0.0005	0.026	0.020	0.76	43.2	1.9
I-Cu0.8K0.8	0.86	26	68.3	7.3	0.6	0.0005	0.026	0.018	0.69	41.0	1.9
	0.86	48	68.2	9.5	0.6	0.0006	0.025	0.019	0.76	43.3	2.2
	0.85	72	69.7	9.6	0.6	0.0006	0.026	0.019	0.73	42.2	2.2
	0.85	96	70.1	10.1	0.6	0.0006	0.026	0.020	0.76	43.1	2.3
	0.85	120	71.3	10.4	0.6	0.0006	0.027	0.019	0.71	41.5	2.2
	0.85	145	72.1	11.2	0.6	0.0006	0.028	0.019	0.71	41.4	2.2
	0.86	168	70.4	11.1	0.6	0.0006	0.026	0.020	0.78	43.8	2.3
	0.85	194	71.0	10.3	0.6	0.0006	0.026	0.020	0.76	43.3	2.3
	0.85	216	72.1	11.1	0.6	0.0006	0.027	0.020	0.75	42.7	2.2
	0.86	240	72.1	10.4	0.6	0.0006	0.027	0.020	0.72	41.7	2.1
	0.86	264	72.4	11.9	0.6	0.0006	0.027	0.020	0.71	41.7	2.2
	0.85	336	72.6	11.9	0.6	0.0006	0.028	0.019	0.70	41.2	2.1
	0.86	360	72.7	12.6	0.6	0.0006	0.028	0.019	0.69	40.8	2.2
	0.86	384	72.7	12.0	0.6	0.0006	0.028	0.019	0.69	40.7	2.2
	0.86	409	72.3	12.3	0.6	0.0006	0.028	0.020	0.71	41.7	2.2
	0.85	432	70.7	10.9	0.6	0.0006	0.026	0.020	0.77	43.6	2.5
	0.85	504	68.9	11.3	0.6	0.0007	0.025	0.020	0.83	45.4	2.6
	0.84	528	69.7	13.8	0.6	0.0006	0.026	0.020	0.77	43.4	2.5
	0.84	552	70.0	12.9	0.6	0.0007	0.026	0.020	0.78	43.8	2.6
	0.84	576	68.9	10.9	0.6	0.0007	0.025	0.020	0.79	44.0	2.6
	0.84	602	70.0	11.3	0.6	0.0007	0.026	0.020	0.75	43.0	2.5

Table 5.3.3: Test data on copper promoted catalysts

The methane selectivity is mainly determined by the basicity of the catalyst surface as explained in the previous paragraph. In this respect, potassium is the main contributor. Therefore, as could be expected, the methane selectivity is in line with the potassium-promoted catalyst S-Cu0.0K5.4. For both catalysts about 2 mole% methane is formed over time as shown in Figure 5.3.9.
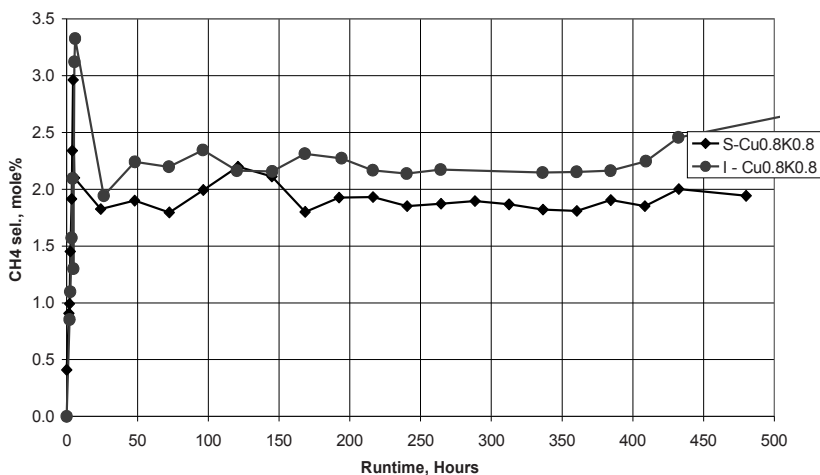
Figure 5.3.9: CH_4 selectivity

Alkene selectivity

As explained before, especially the alkene selectivity is strongly dependent on CO conversion or alkali content. GC data, as presented in Table 5.3.4, show that both ethene and propylene fractions are close to 0.8. For propylene, the absolute value of 0.8 is similar to what has been published before[7] and coincides with our findings in paragraph 5.3.1. For ethene there are very slight differences between the samples that can be explained by the slight differences in conversion between these samples. Typically, a lower ethene fraction is obtained at higher CO conversions[7]. Overall, the data is consistent with previous findings.

	TOS	ethane	ethene	ethene fraction	propane	propylene	propylene fraction
	hours	mole%	mole%	-	mole%	mole%	-
S-Cu0.8K0.8	24	0.111	0.497	0.817	0.094	0.456	0.829
	48	0.093	0.447	0.828	0.076	0.402	0.841
	73	0.098	0.466	0.826	0.074	0.412	0.848
	97	0.102	0.476	0.824	0.083	0.428	0.838
	121	0.100	0.469	0.824	0.077	0.432	0.849
	145	-	-	-	0.079	0.437	0.847
	169	0.097	0.456	0.825	0.075	0.416	0.847
	193	0.085	0.401	0.825	0.066	0.372	0.849
	217	0.085	0.411	0.829	0.067	0.371	0.847
	241	0.083	0.410	0.832	0.070	0.370	0.841
	265	0.085	0.418	0.831	0.069	0.369	0.842
	289	0.085	0.413	0.829	0.071	0.368	0.838
	313	0.085	0.419	0.831	0.072	0.378	0.840
	337	0.086	0.417	0.829	0.068	0.372	0.845
	361	0.086	0.409	0.826	0.069	0.368	0.842
	385	0.084	0.414	0.831	0.069	0.367	0.842
	409	0.083	0.415	0.833	0.070	0.368	0.840
	433	0.086	0.417	0.829	0.069	0.369	0.842
	480	0.090	0.428	**0.826**	0.073	0.390	**0.842**
Avg.	-	0.086	0.417	**0.829**	0.070	0.373	**0.842**
I-Cu0.8K0.8	26	0.095	0.343	0.783	0.070	0.330	0.825
	48	0.109	0.377	0.776	0.076	0.364	0.827
	72	0.118	0.402	0.773	0.077	0.392	0.836
	96	0.125	0.422	0.771	0.081	0.428	0.841
	120	0.131	0.435	0.769	0.083	0.451	0.845
	145	0.137	0.456	0.769	0.086	0.463	0.843
	168	0.130	0.444	0.774	0.082	0.447	0.845
	194	0.128	0.443	0.776	0.081	0.451	0.848
	216	0.136	0.473	0.777	0.083	0.452	0.845
	240	0.128	0.451	0.779	0.081	0.451	0.848
	264	0.133	0.458	0.775	0.083	0.457	0.846
	336	0.136	0.464	0.773	0.085	0.471	0.847
	360	0.137	0.468	0.774	0.085	0.471	0.847
	384	0.138	0.470	0.773	0.088	0.469	0.842
	409	0.139	0.472	0.773	0.085	0.475	0.848
	432	0.137	0.465	0.772	0.086	0.475	0.847
	504	0.134	0.456	0.773	0.086	0.465	0.844
	528	0.138	0.462	0.770	0.089	0.469	0.841
	552	0.146	0.475	0.765	0.095	0.483	0.836
	576	0.138	0.457	0.768	0.088	0.462	0.840
	602	0.144	0.468	**0.765**	0.091	0.482	**0.841**
Avg.	-	0.139	0.466	**0.770**	0.089	0.473	**0.842**

Tabel 5.3.4: GC analyses

5.4   Conclusions

The aim was to show that the catalysts used in this thesis are actually suitable for Fischer-Tropsch synthesis. It is shown that in case potassium is used as a promoter, the water-gas-shift (WGS) reaction increases considerably. The WGS reaction was found not to be rate-determining. Addition of potassium leads to a longer induction period, a higher alpha value, lower H_2/CO usage and lower methane selectivity compared to a potassium free sample.

The catalyst conversion can be enhanced by addition of copper as promoter. The way the promoters are added, either by spray-drying or via impregnation, does not make a significant difference in our study. Like in the copper free samples, the WGS was found not to be rate-determining. Copper clearly increases the overall chain length making it a better catalyst.

All catalysts were able to produce hydrocarbons. Still, a combination of copper and potassium leads to the best performance.

All data is consistent with previous literature data and we can conclude that the samples are able to perform Fischer-Tropsch chemistry.

5.5   References

1.   Van der Laan, G. P. *Kinetics, Selectivity and Scale Up of the Fischer-Tropsch Synthesis*. *University of Groningen* (Thesis, University of Groningen, 1999).

2.   Callaghan, C. Kinetics and catalysis of the water-gas-shift reaction: A microkinetic and graph theoretic approach. (Worcester Polytechnic Institute, 2006).

3.   Davis, B. H. Preparation of iron FT catalysts. in *Greener Fischer-Tropsch Processes Fuels Feedstocks* 173–191 (Wiley-VCH Verlag GmbH & Co. KGaA, 2013).

4.   Todic, B., Nowicki, L., Nikacevic, N. & Bukur, D. B. Fischer-Tropsch synthesis product selectivity over an industrial iron-based catalyst: Effect of process conditions. *Catal. Today* **261,** 28–39 (2016).

5.   Brien, R. J. O. & Davis, B. H. Impact of copper on an alkali promoted iron Fischer – Tropsch catalyst. *Catal. Lett.* **94,** 1–6 (2004).

6.   Davis, B. H. Fischer-Tropsch synthesis: relationship between iron catalyst composition and process variables. *Catal. Today* **84,** 83–98 (2003).

7.   Raje, A. P., O'Brien, R. J. & Davis, B. H. Effect of potassium promotion on iron-based catalysts for Fischer-Tropsch synthesis. *J. Catal.* **180,** 36–43 (1998).

8.   Luo, M. & Davis, B. H. Fischer-Tropsch synthesis: Group II alkali-earth metal promoted catalysts. *Appl. Catal., A* **246,** 171–181 (2003).

9.   Ngantsoue-Hoc, W., Luo, M., Zhang, Y., O'Brien, R. J. & Davis, B. H. Fischer-Tropsch synthesis: activity and selectivity for Group I alkali promoted iron-based catalysts. *Appl. Catal., A* **236,** 77–89 (2002).

10.   Satterfield, C. N. & Yates, I. An innovative catalyst system for slurry-phase Fischer-Tropsch synthesis: Cobalt plus a water-gas-shift catalyst. DOE/PC/79816-T3 (DE92011275). (1991). Available at: http://www.osti.gov/energycitations/product.biblio.jsp?osti_id=10133118.

11.   Tau, L. M., Dabbagh, H. A. & Davis, B. H. Fischer-Tropsch synthesis: carbon-14 tracer study of alkene incorporation. *Energy & Fuels* **4,** 94–99 (1990).

12.   Yang, Y., Xiang, H.-W., Xu, Y.-Y., Bai, L. & Li, Y.-W. Effect of potassium promoter on precipitated iron-manganese catalyst for Fischer-Tropsch synthesis. *Appl. Catal., A* **266,** 181–194 (2004).

13.   Luo, M., O'Brien, R. J., Bao, S. & Davis, B. H. Fischer-Tropsch synthesis: induction and steady-state activity of high-alpha potassium promoted iron catalysts. *Appl. Catal., A* **239,** 111–120 (2003).

6

Preparation of carbon-free TEM microgrids by metal sputtering

A new method for preparing carbon-free, temperature stable TEM grids is presented. An 80% Au / 20% Pd metal film is deposited onto a 'holey' microgrid carbon supported on standard mixed mesh Au TEM grids. Subsequently, the carbon film is selectively removed using plasma-cleaning. This way, an all-metal TEM film is made containing the 'same' microgrid as the original carbon film. Although electron transparency of the foil is reduced significantly, the open areas for TEM inspection of material over these areas are maintained. The metal foil can be prepared with various thicknesses and ensures good electrical conductivity. The new Au/Pd grids are stable to at least 775K under vacuum conditions.

Part of this work was published in Ultramicroscopy[1]

CHAPTER 6

6.1   Introduction

The effectiveness of high resolution (Scanning) Transmission Electron Microscopy
((S)TEM) in combination with high resolution Electron Energy Loss Spectroscopy (EELS)
in providing chemical information, such as the oxidation state and coordination of specific
atoms[2], depends on a various non-TEM related factors, including sample thickness[3],
contamination and thickness of the support. For the latter two, the composition and
quality of the TEM grids play an essential role.

TEM grids covered with microgrid carbon films are often used in combination with EELS.
Although these TEM grids suffice in many cases, sometimes the use of carbon needs to
be avoided. For example, carbon films are not stable at elevated temperatures. This
problem has already been addressed two decades ago[4], when microgrid carbon film
supported on Pt mesh TEM grids was covered with Si_3N_4 by RF-cathodic sputtering of Si
in an atmosphere of 6% N_2 in Ar at a total pressure of $8*10^{-3}$ mbar. The carbon support
film was then removed by air calcination at 775°C. Although this method produces
stable, inert, microgrid TEM supports, it requires precise control of the gas atmosphere
during sputtering. Nowadays, perforated Si_3N_4 grids can also be obtained commercially.
Although Si_3N_4 grids have a distinct advantage in being carbon-free, the grids are brittle
and break easily. In this chapter we describe a straightforward method to prepare
carbon-free TEM grids suitable for HRTEM-HREELS. The method consists of applying a
metal coating to carbon-covered TEM grids followed by selective removal of the carbon
using plasma-cleaning.

The metal coatings can easily be applied using a standard SEM sputter-coater. Although
not shown in this paper, obviously a variety of metals can be sputtered depending only
on the availability of metal targets as shown by Stokroos et al.[5]

6.2   Experimental

Metal coatings were applied to Quantifoil R1.2/1.3 carbon microgrid on Au mixed mesh
TEM grids. These grids were sputtered using a standard SEM sputter-coater (Quorum
Technologies SC7640) in combination with a standard 80% gold / 20% palladium target.
The settings applied were: Voltage = 2.0 kV, plasma current = 10-20 mA and chamber
pressure = 0.3 mbar argon. To control the layer thickness, the coater was equipped with
a 'film thickness monitor' (Quorum Technologies FT7690). Coatings of 7 nm, 10 nm and
15 nm were prepared. Our coatings were applied on the foil side of the TEM grids.

The carbon film was selectively removed using a plasma cleaner (Fischione Model 1020) using a 13.56 MHz oscillating field system with a gas mixture containing 25% oxygen and 75% argon. The gradual removal of the carbon film was monitored using a FEI Tecnai F20 TEM equipped with a FEG and Gatan Image Filter (GIF) and operated at 200 kV. Both Energy Dispersive X-ray analysis (EDAX EM-200ST) and TEM-EELS were used. EEL spectra were recorded using the GIF electron energy loss spectrometer. Thermal stability of the pure metal films was investigated using an in-situ heating holder (type: Gatan 652 double tilt heating holder). Next to this, a grid was calcined at 775 K in air for 2 hours (ramp rate = 10 K/min) using a traditional thermo gravimetric analysis (TGA) set-up. An overview of the grids prepared is shown in Table 1.

Sample#	Film thickness (nm)	Plasma Cleaned	Calcined in air	T* (K)
1	7	No	No	RT
2	7	Yes	No	RT
3	10	No	No	RT
4	10	Yes	No	775**
5	10	No	Yes	775#
6	10	No	Yes	1075#
7	15	No	No	RT
8	15	Yes	No	RT

Table 1: Grids overview.

*   *Maxiumum temperature the grid was subjected to. RT= room temperature.*
**   *Temperature inside the TEM using the in-situ heating holder.*
#   *Pre-calcined in air, measured at room temperature.*

6.3   Results and discussion

6.3.1   Effects of coating

The Au/Pd coating increases the image contrast of the carbon microgrid in TEM. This is illustrated in Figure 1a and b for the thinnest metal coating used: 7 nm. A similar increase in contrast is observed when applying a 10 nm or 15 nm coating (not shown). At higher magnification, small metal clusters can be observed (Figure 1c and d). These figures also show that the coating is not completely continuous; some electron transparent gaps are visible. Such gaps are typically observed in for instance gold coated biological samples for SEM measurements[6]. The size of these gaps mainly depends (inversely) on

the grain size of the deposited metal crystallites and the thickness of the metal coating. Indeed, the number of gaps is less when applying thicker coatings (not shown). In between the gaps, areas of coalesced grains are present. At high magnification the individual metal crystallites can be distinguished (Figure 1d). Based on 50 different crystallites, the average grain size of sample #1 was determined to be 8.3 nm ± 2.0 nm; similar to the value determined by the film thickness monitor (7 nm). Although not visible in Figure 1b-d, the carbon foil is still present after coating: EELS shows a carbon edge of amorphous carbon (Figure 2).
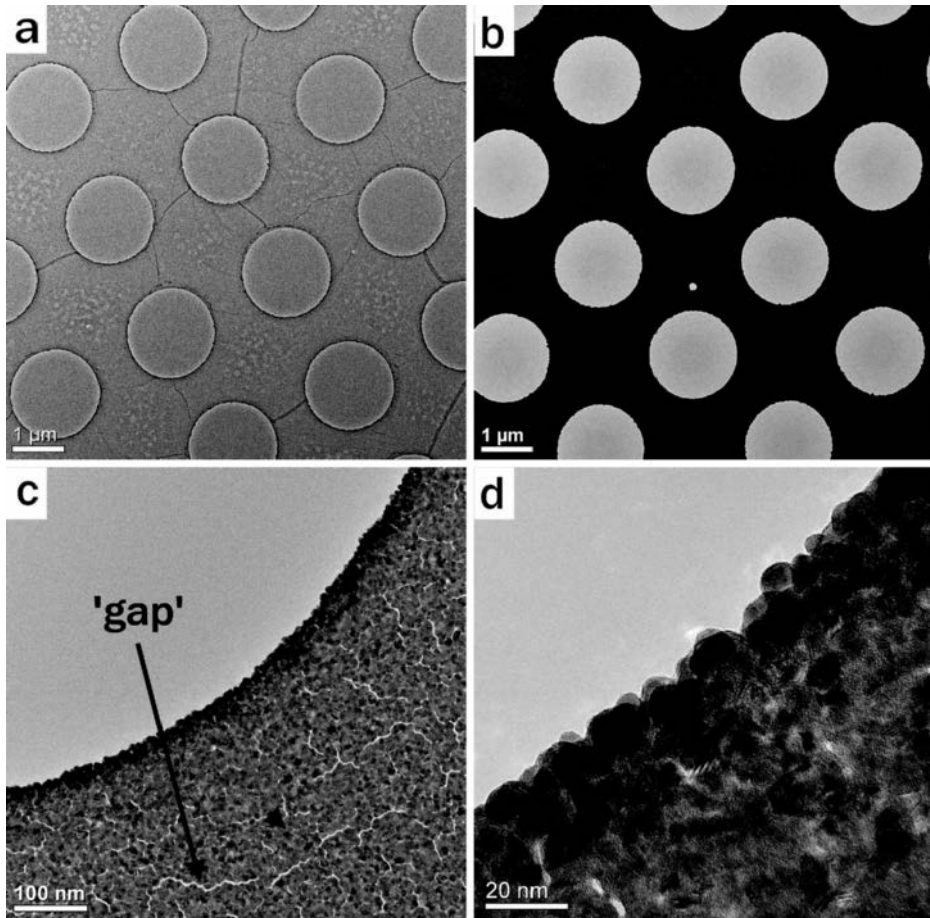
Figure 1: TEM images of a Quantifoil carbon film before coating (a), sample #1 with 7 nm Au/Pd coating (b) and sample #1 at higher magnifications (c-d).
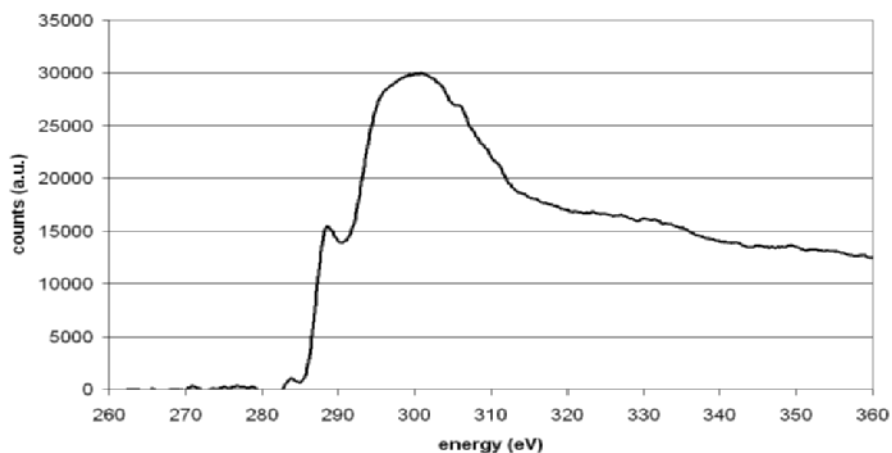
Figure 2: EEL spectrum of sample #1 showing the carbon edge.

6.3.2   Plasma-cleaning

The original carbon foil was removed using plasma cleaning. To determine the effectiveness, EELS measurements were performed after different time intervals of plasma cleaning. Identical microscope settings were maintained so we can compare the data quantitatively. The time dependency of carbon removal is shown in Figure 3.
It was found that 12 minutes of continuous plasma-cleaning is sufficient to remove the 12 nm thick carbon film. EDX analysis was performed on the same samples. The results corroborate the selective removal of carbon and show the presence of the gold / palladium coating (see Figure 4). The stability of the gold / palladium coating during plasma cleaning is illustrated in Figure 5, which shows the same area before and after plasma cleaning.

Figure 3: Carbon EEL spectra showing the effect of plasma cleaning in time.

Figure 4: EDX spectra of samples #1 and #2, 7 nm Au/Pd coating, before and after plasma cleaning (normalized to Au signal).
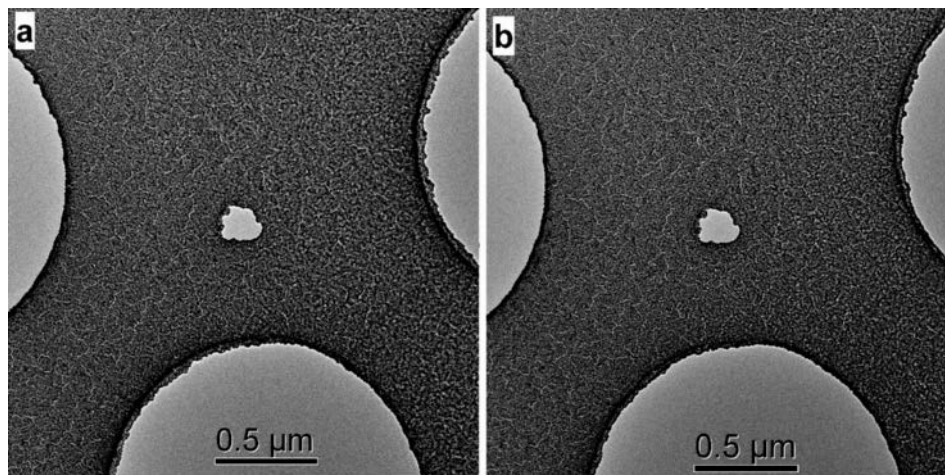
Figure 5: TEM images of samples #1 and #2, the same area before (a) and after (b) plasma cleaning.

6.3.3 Examples

The advantage of our method is illustrated with STEM experiments on $LaCaMnO_3$ crystals supported on the new grids. Specimens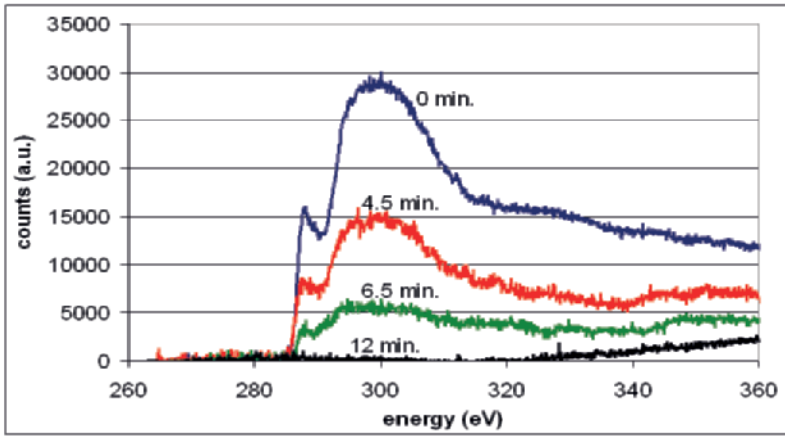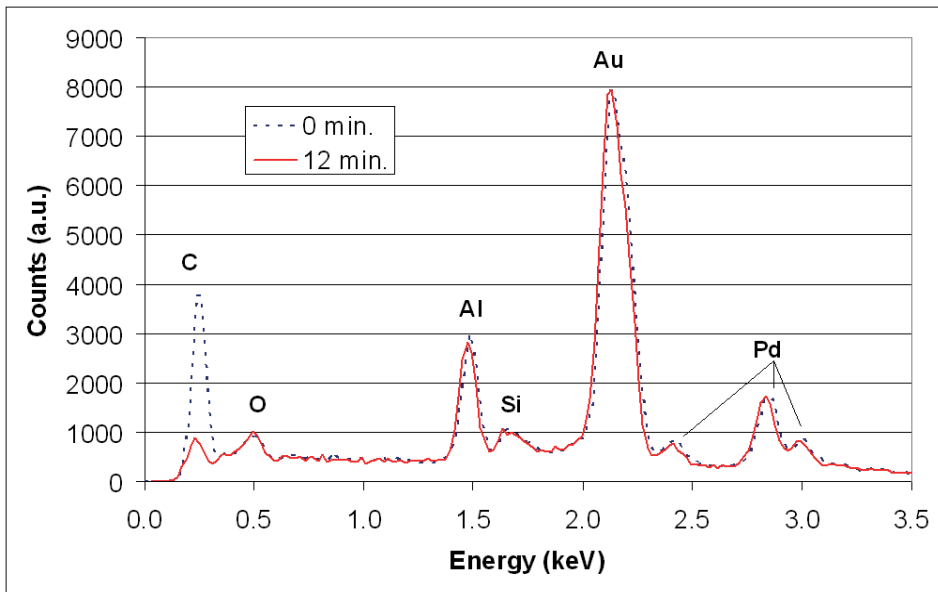 like this are often dispersed onto TEM grids using a low boiling organic liquid such as ethanol or hexane. This procedure ensures a good electrical contact of the specimen with the film, essential to prevent charging effects. Although the majority of the organic liquid will evaporate quickly, this procedure can lead to carbon contamination. This is a common problem, especially for STEM.

Figure 6a shows a HAADF STEM image of a $LaCaMnO_3$ crystal on a Quantifoil R1.2/1.3 carbon microgrid dispersed with ethanol. Figure 6b shows the same crystal after placing a focused electron beam onto the crystal for about 4 seconds. A deposit is formed instantly, as indicated by the arrows. EELS and EDX measurements proved this deposit to be carbon (not shown). The fast accumulation of carbon hampers any further analyses.

A similar effect is seen using our Au/Pd grid (even though the carbon film has been removed) as shown in Figure 7a and b respectively. However, an advantage of using Au/Pd grids, in contrast to carbon films, is their stability towards plasma cleaning. In Figure 8a and b, we again show STEM data of $LaCaMnO_3$ crystals (like in Figure 7) but now after 30 seconds of plasma cleaning of the sample on the grid. In this case, no deposit is formed, even after 5 minutes of focused beam exposure (Figure 8b). The

surface remains clean of contamination and can easily be analyzed (for instance using STEM-EELS). Such 'clean' measurements could never have been obtained using regular carbon-based grids.
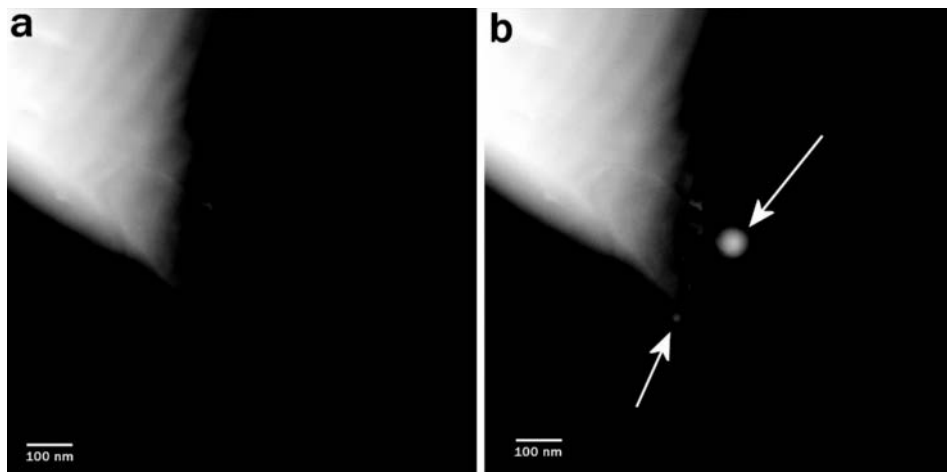
Figure 6: HAADF STEM images of LaCaMnO$_3$ on a carbon microgrid before (a) and after (b) exposure to a focused electron beam.
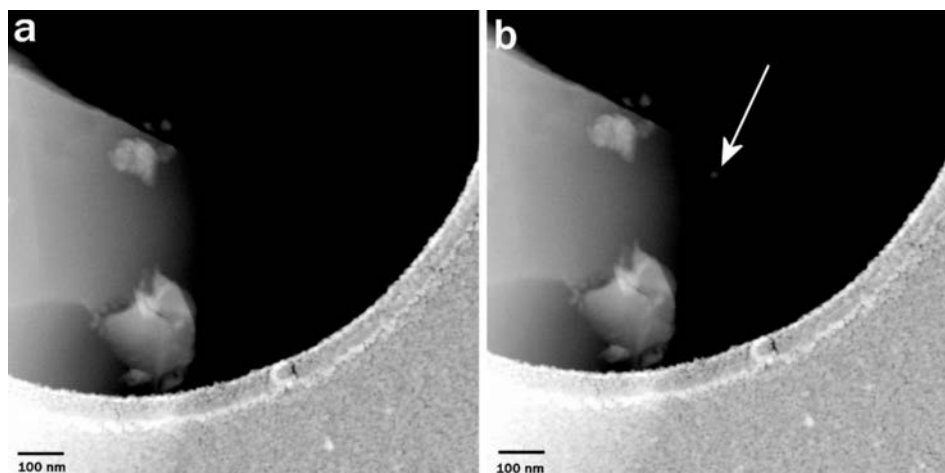
Figure 7: HAADF STEM images of LaCaMnO₃ on an Au/Pd grid before (a) and after (b)
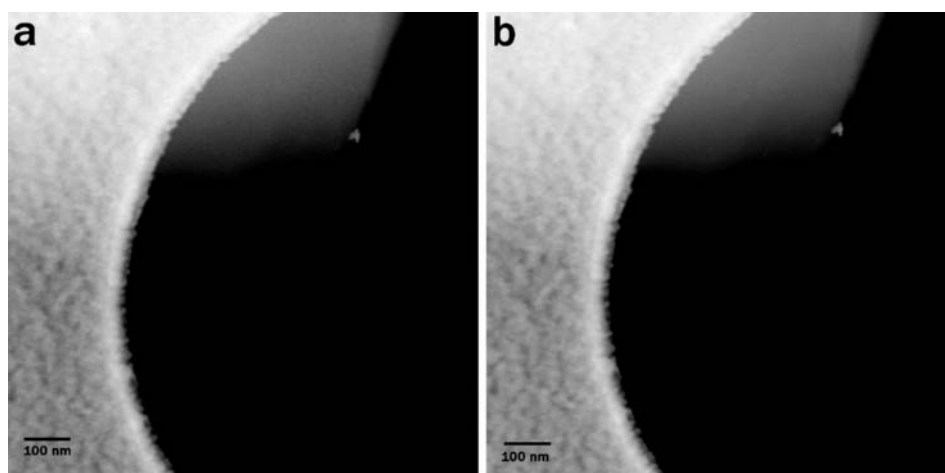
Figure 8: HAADF STEM images of LaCaMnO₃ on an Au/Pd grid after 30 seconds plasma cleaning before (a) and after (b) exposure to a focused electron beam.

6.3.4 Thermal stability

To determine the thermal stability of the metal film, a 10 nm Au/Pd coated, plasma cleaned TEM grid was mounted in a Gatan heating stage. Starting from 304K, the temperature was increased to 775K in about 30 minutes. During this procedure we noticed a slight change in focus, likely due to minor thermal expansion of the foil. The Au/Pd foil is stable at least up to 775 K in vacuum (Figure 9a).

In an attempt to burn off the original carbon foil in air, we used a traditional TGA set-up. Although the weight loss of a single grid is too low to be determined by TGA, this system is very convenient for calcination of small samples. After 2 hours calcination at 775K (ramp rate = 10K / min) the grid shows large defects (see Figure 9b). Apparently, sintering of the Au/Pd metals occurred while part of the carbon was still present according to EDX and EELS (not shown). After calcination at 1075K, the metal foil was completely destroyed, leaving only the grid bars visible.
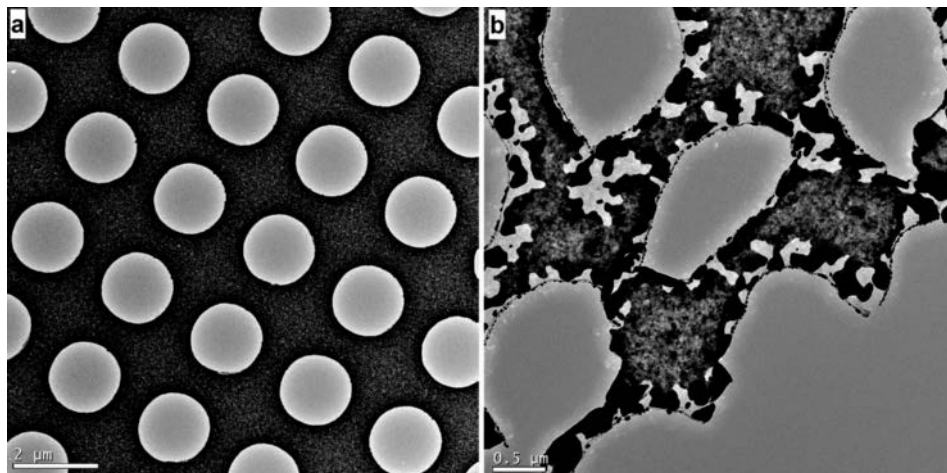
Figure 9: TEM images of sample #4, 10 nm Au/Pd coating at 775K in vacuum (a) and after calcination in air at 775K (b).

6.4   Conclusions

Starting from standard microgrid carbon film covered TEM grids, the use of a standard SEM sputter-coater in combination with a thickness monitor is very convenient for preparing carbon-free TEM grids. After coating, the carbon film is still present but can be removed easily and selectively using plasma cleaning. An all-metal microgrid is obtained while maintaining the open areas of the original carbon microgrid. Since very thin films can be prepared and the thickness can be controlled easily, this technique is also very suitable for creating metal specimens for EELS analysis.

Carbon removal by burning it off in air is less favorable for the Au/Pd films presented here. After two hours at 775K, large deformations of the film were observed. After calcination at 1075K, the metal foil had been destroyed completely.

Although not shown in this paper, other metals than Au/Pd can be sputtered using the same procedure. When a metal or alloy can be found that is stable to removal of the

carbon film by calcination in air, multiple grids can be prepared in large batches, thereby shortening the preparation time.

6.5   <u>References</u>

1.   Janbroers, S., Zandbergen, H. W., de Kruijff, T. R., Xu, Q. & Kooyman, P. J. Preparation of carbon-free TEM microgrids by metal sputtering. *Ultramicroscopy* **109,** 1105–9 (2009).

2.   Lazar, S., Zandbergen, H. W., Botton, G. A., Wu, M.-Y. & Tichelaar, F. D. Materials science applications of HREELS in near edge structure analysis and low-energy loss spectroscopy. *Ultramicroscopy* **96,** 535–546 (2003).

3.   Egerton, R. F. in *Electron Energy-Loss Spectroscopy in the Electron microscope, 2nd ed.* 26 (Plenum press).

4.   Zandbergen, H. W., Pruymboom, A. & Van Tendeloo, G. Highly temperature-stable Si3N4 perforated grids. *Ultramicroscopy* **24,** 45 (1988).

5.   Stokroos, I., Kalicharan, D., Van Der Want, J. J. L. & Jongebloed, W. L. A comparative study of thin coatings of Au/Pd, Pt and Cr produced by magnetron sputtering for FE-SEM. *J. Microsc.* **189,** 79 (1998).

6.   Kemmenoe, B. & Bullock, G. Structure analysis of sputter-coated and ion-beam sputter-coated films: a comparative study. *J. Microsc.* **132,** 153–163 (1983).

CHAPTER 6

7

Conclusions

CHAPTER 7

7.1. __Conclusions__

In this thesis it is shown that carburization of iron Fischer-Tropsch catalysts in a stream of CO gas yields a mixture of different phases. XRD and TEM-EELS show that the precursor hematite is reduced to magnetite and iron carbide. XRD showed mainly iron carbide with an unknown structure to be present next to magnetite. By combining information from both X-ray powder diffraction and (TEM) electron diffraction we characterized the unknown iron carbide phase.

It is built up from two different layers (A and B; Layer A contains three and B contains two iron sub-layers while both have one sub-layer of carbon) of an irregular stacking in which A^+ is always followed by B^+ (and A^- by B^-) but B^+ has a 60% chance of being followed by B^- instead of A^+ (and, likewise, B^- has a 60% chance of being followed by B^+). This stacking model explains the observed PXRD pattern. We also observed χ-Fe_5C_2 carbide ($A^+B^+A^+B^+A^+B^+\ldots$ or, equivalently, $A^-B^-A^-B^-A^-B^-\ldots$) and for what in the literature has been designated as the "hypothetical θ_∞-Fe_2C" ($B^+B^-B^+B^-\ldots$). One implication of this structure model is that the C-content is higher than in the pure χ-Fe_5C_2 carbide (Fe/C = 2.29 instead of 2.5). At this point we can only speculate about cause and effect: whether the faulted nature of the carbide allows more carbon to be stored or whether the chemical potential of carbon during the carburization process forces the faulted structure on the carbide. To estimate the relative stability of the θ_∞–Fe_2C, Projector-Augmented Wave (PAW) calculations were done that reveal that θ_∞-Fe_2C is relatively high in energy and thermodynamically unstable. This implies that θ_∞-Fe_2C is probably only stable in a mixed layer stacking such as described in Chapter 3.

TEM results also showed that after carburization, carbon layers are present but reside predominantly on iron-carbide species and not on iron oxide species. Exposure to air leads to re-oxidation of the iron carbides. After exposure to air, the iron oxide species are covered in amorphous carbon. We believe that during re-oxidation, carbon is liberated from its solid solution in iron or iron carbide and deposited as a separate amorphous phase. Additional research is required to determine the exact nature of these mobile carbon species. Nevertheless, our data show that the carbon surface layers can change, or even form, during exposure to air. We proved that activated iron-based Fischer-Tropsch catalysts are very air-sensitive. Even after careful passivation the catalyst surface changes significantly and does not represent the actual catalyst surface anymore. Therefore, when studying these catalysts, any exposure to air should be

avoided. This also means that one should be vigilant when interpretation data from studies on catalysts that have been passivated or otherwise have been exposed to air.

During carburization inside an ETEM at 20 Torr CO, hematite containing precursors are reduced. During, or shortly after this reduction huge sintering occurs. We proved that this sintering is enhanced by low pressure conditions in combination with CO gas. Since the oxygen removal during the decomposition of iron oxide is improved in vacuum, we conclude that this process is diffusion limited. In all, our results show that this process is very pressure dependent. The reduction inside the ETEM is so effective that metallic iron can be formed. Eventually, about 50 nm size crystallites grow out of the iron (oxide) particles. In time, these newly formed crystallites reduce in size to about 5-30 nm. EELS proves these features are iron carbides. In contrast to literature data published so far, we found no carbon deposits on the outer rim of the iron carbides at high temperature conditions. Note however, that all previous studies involve catalysts that are cooled prior to analysis. During this cooling, carbon deposits could have been formed. In addition, many available studies are performed on passivated samples. We have shown previously that this passivation can also lead to carbon deposits.

We proved that the catalysts used in this thesis are actually suitable for Fischer-Tropsch synthesis. All performance data is consistent with previous literature data.

Overall, still more study is required to elucidate the exact mechanism. The next challenge will be to perform real in situ (TEM) studies under industrial relevant conditions; viz. at even higher pressures than what is possible today.

CHAPTER 7

Appendix A

Electronic structure and energy of formation of θ_∞-Fe$_2$C

With special thanks to J. Louwen for his contribution to this work.

A.1. <u>Introduction</u>

In chapter 3 we concluded that, based on both powder X-ray and electron diffraction data, the iron carbide present in a freshly carburized Fisher-Tropsch catalyst is due to a semi-random stacking of layers that in some instances corresponds to the well known χ-Fe_5C_2, but in others to the unknown θ_∞-Fe_2C. This left us with questions about the relative stability of θ_∞-Fe_2C, given that, to the best of our knowledge, it has never been identified before.

Relevant experimental data on iron carbides are hard to obtain since it is difficult, if not actually impossible, to obtain the carbides in a pure form. Thus, even for the well-known χ-Fe_5C_2 there is still no consensus about its crystal structure. Some claim a monoclinic lattice [1], others a triclinic one[2]. This does not bode well for the prospects of ever obtaining accurate experimental thermodynamic data of iron carbides.

In the absence of such data, the best we can do is to apply quantum mechanics as rigorously as available computer resources allow. At the current state of the art, and stipulating affordable computational resources, the Projector-Augmented Wave (PAW) method of Blöchl[3] is arguably the best choice.

A few computational studies on iron carbides have been reported in the literature. Faraoun et al.[4] computed the structures of θ-Fe_3C, χ-Fe_5C_2 and η-Fe_2C with an all-electron method (as opposed to the PAW method where core orbitals are frozen, i.e. constrained to be as in the free atom). Calculations with the commercial VASP package which implements the same methodology applied here[5] were done by De Smit et al. on θ-Fe_3C, monoclinic χ-Fe_5C_2 and η-Fe_2C, ε-Fe_3C, ε-Fe_2C and the hexagonal form of Fe_7C_3[6] as well as by Fang et al. on hexagonal and orthorhombic Fe_7C_3[7] as well as on θ-Fe_3C, monoclinic χ-Fe_5C_2,η-Fe_2C and ε-Fe_2C[8]. Lv et al. reported calculations on various Fe_2C polymorphs using a pseudopotential method[9]. None of these publications has dealt with θ_∞-Fe_2C.

In this chapter, therefore, we report PAW calculations on θ_∞-Fe_2C, as well as on θ-Fe_3C, η-Fe_2C, triclinic χ-Fe_5C_2 and both the orthorhombic and hexagonal forms of Fe_7C_3. Inclusion of the other carbide phases might seem a duplication of effort but is in fact required for a good comparison. For the same reasons, calculations on α-Fe and the diamond structure were performed with the same method to provide reference energies.

A.2.   Materials and Methods

Computed lattice parameters are compared with experimental values. These were taken from the following references: θ-Fe$_3$C[10], η-Fe$_2$C[11], χ-Fe$_5$C$_2$[2], the orthorhombic form of Fe$_7$C[12], the hexagonal form of Fe$_7$C$_3$[13], α-Fe[14] and diamond[15].

The calculations were done with the PWSCF program from the Quantum ESPRESSO Version 4.2.1 software suite[16], employing the Perdew-Burke-Ernzerhof (PBE) functional[17] in the Projector Augmented Wave function (PAW)[3] approach. The PAW setups (defining the frozen core and the pseudization of the valence orbitals in the core region) were obtained using ATOMPAW[18] with input files taken from the repository[19]. These input files were slightly modified to account for the difference between the original PAW formulation[3] and the Kresse implementation[5] that has been adopted in PWSCF, as outlined by Torrent et al.[20]. The ATOMPAW input files are given in paragraph A.3.4.

In all calculations, the cutoff value for inclusion of plane waves in the wave functions was set at 30 Rydberg energy units while the cutoff for inclusion in the density was set at 300 Ry. In view of the metallic character of the carbides, electron smearing was applied using the Marzari-Vanderbilt scheme[21] and a smearing parameter of 0.00735 Ry, i.e. 0.1 eV. Both atom positions and cell constants were optimized to obtain the minimum energy. With the exception of the diamond structure, all calculations were done in a spin-polarized mode (meaning that separate densities for α and β spin electrons were allowed). The resulting magnetic moments are reported.

Numerical integration over the Brioullin zone was done using the Monkhorst-Pack k point distribution scheme[22], choosing n k-points along each reciprocal unit cell axis such that n times the unit cell axis is approximately 35 Å.

Since the PWSCF program appears to base the number of plane waves on the cutoff energy values and the *initial* geometry, at the end of each geometry optimization the result was used as input for a subsequent calculation until self-consistency was reached in that respect too.

A.3. Results and Discussion

A.3.1. Computed magnetic moments

As stated in the computational part, in all calculations (except those on the diamond structure) different electron densities for α and β spin electrons were allowed (since transition metals often feature high-spin states). By integrating the difference between these two states we obtain the magnetic moment of the unit cell. This value is usually normalized by dividing either by the number of stoichiometric units or by the number of transition metal atoms in the unit cell. Table 1 reports both options.

The computed magnetic moments are of interest for two completely different reasons. Firstly, a comparison between the computed magnetic moments and experimental values or values computed by others is a good way to check whether the calculations have produced meaningful results.

Secondly, an exploration of the magnetic properties of different iron carbides might suggest ways of influencing the carburization by the application of magnetic fields.

	Calculated magnetic moment [μB]	per unit [μB]	per unit exp. [μB]	per unit other calculations [μB]	per Fe [μB]
cementite, θ-Fe_3C	22.20	5.55		5.59[7], 5.77[4]	1.85
θ_∞-Fe_2C	11.35	2.84			1.42
η-Fe_2C	6.24	3.12		3.34[4]	1.56
χ-Fe_5C_2	33.70	8.43	8.9[23]	8.81[4]	1.69
hexagonal Fe_7C_3	23.26	11.63		11.81[7]	1.66
orthorhombic Fe_7C_3	47.99	12.00		12.15[7]	1.71
ferrite, α-Fe	4.41	2.21	2.2[24,25]		2.21
diamond	0.00	0.00			0.00

Table 1: Magnetic moments given in Bohr magneton, or mB, units as calculated and compared to experimental values or values calculated by others.

As can be seen, the calculated magnetic moments match the values previously reported in literature. Obviously, there is neither an experimental nor a theoretical value for the magnetic moment of θ_∞-Fe_2C to compare with. This makes it plausible that the methodology used here is capable of reproducing the true electronic structure of iron carbides.

We find a correlation between Fe/C ratio and magnetic moment per Fe atom, which implies that the presence of C diminishes the net spin excess. Thus, pure iron has the

largest moment, followed by Fe_5C_2 and Fe_7C_3 while Fe_2C has the smallest magnetic moment. However, other factors come into play too, since there is a significant difference between the values computed for θ_∞-Fe_2C (1.42 μ_B) and η-Fe_2C (1.56 μ_B).

A.3.2. Carbide structures

Another way of evaluationg the quality of our calculations is by comparing the computed geometries with the observed ones. Table 2 lists the experimental and computed lattice parameters (axes only). Gratifyingly, we find that the deviations are in the order of magnitude of 1% relative. Note that the experimental structures were determined at finite temperature whereas the computed values refer to, effectively, 0 K (and do not account for zero-point vibration either). Since the computed axis lengths are in all cases smaller than the observed ones, a correction for thermal expansion would even reduce the average error to well below the 1% level.

The exception is θ_∞-Fe_2C. Here, the errors are substantially larger than for all other compounds. Since the "experimental" values were fairly coarse estimates obtained by manually adapting the fit between the observed and simulated X-ray diffraction patterns as described in Chapter 3, either the estimates were quite inaccurate or, more likely, the virtual single crystal structure of θ_∞-Fe_2C is considerably different from the structure of nanolayers of θ_∞-Fe_2C within the semi-random stacking in the freshly carburized catalyst studied.

	experimental			computed		
	a	b	c	a	b	c
cementite, θ-Fe₃C	4.525	5.088	6.74	4.4667 (1.3 %)	5.0436 (0.9 %)	6.7127 (0.4 %)
θ∞-Fe₂C	4.625	5.059	4.616	4.4966 (2.8 %)	4.9275 (2.6 %)	4.8990 (6.1 %)
η-Fe₂C	4.704	4.318	2.83	4.6921 (0.3 %)	4.2748 (1.0 %)	2.8147 (0.5 %)
χ-Fe₅C₂	11.5695	4.5712	5.0588	11.5269 (0.4 %)	4.5071 (1.4 %)	4.9956 (1.2 %)
hexagonal Fe₇C₃	6.882	6.882	4.54	6.8178 (0.9 %)	6.8178 (0.9 %)	4.4847 (1.2 %)
orthorhombic Fe₇C₃	4.537	6.892	11.913	4.5075 (0.6 %)	6.8521 (0.6 %)	11.735 (1.5 %)
ferrite, α-Fe	2.86623	2.86623	2.86623	2.8405 (0.9 %)	2.8405 (0.9 %)	2.8405 (0.9 %)
diamond	3.56712	3.56712	3.56712	3.5456 (0.6 %)	3.5456 (0.6 %)	3.5456 (0.6 %)

Table 2: Experimental and computed unit cell axis lengths for all compounds. Values are given in Å units. Underneath the computed values the relative deviation from the corresponding experimental value is given.

To complete the comparison of experimental and computed lattice parameters: in all cases except χ-Fe₅C₂, the computed angles agree with the experimental values (all 90° for the cubic and orthorhombic structures; 90° and 120° for hexagonal Fe₇C₃) either completely or to within 0.001°. For χ-Fe₅C₂ we used a triclinic starting structure taken from reference[26] instead of the monoclinic one claimed by Retief [18]. Ultimately, we obtained an equilibrium geometry with angle values of 90.001°, 97.678° and 90.012° respectively. These are closer to the angle values of 90°, 97.746° and 90° of Retief[1] than to the values of 90.115°, 97.765° and 90.036° of du Plessis et al.[26], so our calculations do not appear to support a triclinic structure for χ-Fe₅C₂.

A.3.3. Iron carbide energies of formation

The energy of formation, an estimate for the heat of formation, can be obtained from the total energy computed for a carbide with m Fe and n C atoms in the unit cell and the total energies computed for α-Fe (with two Fe atoms in the unit cell) and graphite (with four C atoms in the unit cell):

$$E_f(Fe_mC_n) = E_{Total}(Fe_mC_n) - m\frac{E_{Total}(\alpha - Fe)}{2} - n\frac{E_{Total}(\text{graphite})}{4}$$

Unfortunately, PBE, like most density functionals, does not describe non-covalent interactions very well[27]. As a result, a computed energy would be of questionable value. Diamond, on the other hand, consists of covalently bonded C atoms and no such issues are to be expected there. Consequently, Fang et al. have suggested using the computed value for diamond and adding the experimentally determined (small) difference in energy between diamond and graphite for which they propose a value of 17meV (0.39 kcal/mol) per C atom[7]. We will follow the same approach, but with an energy difference of 0.45 kcal/mol as derived from the difference in enthalpy of combustion of graphite and diamond[28], which leads to (for the energy expressed in kcal/mol):

$$E_f(Fe_mC_n) = E_{Total}(Fe_mC_n) - m\frac{E_{Total}(\alpha - Fe)}{2} - n\left(\frac{E_{Total}(\text{diamond})}{8} - 0.45\right)$$

Using a different reference does not, of course, affect the relative ordering of carbides, but will give more realistic estimates of the heats of formation.

The energy of formation per unit cell is not a practical number in this case since the unit cells vary in size and content (for instance, the unit cell for orthorhombic Fe$_7$C$_3$ is two times as large and has twice the number of atoms of the hexagonal cell). In Table 3 we have therefore normalized the energy by dividing by, respectively, the total number of atoms in the unit cell, the number of Fe atoms or the number of C atoms.

	per atom	per Fe	per C
Cementite, θ- Fe$_3$C	0.35	0.47	1.41
θ_∞-Fe$_2$C	0.77	1.16	2.31
η-Fe$_2$C	0.15	0.22	0.44
χ-Fe$_5$C$_2$	0.30	0.42	1.04
hexagonal Fe$_7$C$_3$	0.48	0.68	1.59
orthorhombic Fe$_7$C$_3$	0.34	0.49	1.14

Table 3: Calculated energies of formation (in kcal/mol) normalized per atom, per Fe atom and per C atom, respectively.

Apart from cementite and orthorhombic Fe$_7$C$_3$, which are quite close in energy per atom, the ordering obtained is the same no matter how the energy is normalized. The relative stability can be summarized as: θ_∞-Fe$_2$C << hexagonal Fe$_7$C$_3$ < θ-Fe$_3$C < orthorhombic Fe$_7$C$_3$ < χ-Fe$_5$C$_2$ < η-Fe$_2$C. This ordering partly agrees with that obtained by De Smit et

al.[29], but not completely. In part this is trivial since De Smit et al. did not include orthorhombic Fe_7C_3 into the set, only the less stable hexagonal form. In part the difference is real since the ordering of θ-Fe_3C and χ-Fe_5C_2 is reversed. Fang et al. find the same θ-Fe_3C and χ-Fe_5C_2 ordering as we do[8] despite the fact that they use the same VASP program as De Smit et al. The conclusion that the orthorhombic form of Fe_7C_3 is significantly more stable than the hexagonal form agrees with the findings of Fang et al.[7] This renders the existence of truly hexagonal Fe_7C_3 questionable.

Our focus is on θ_∞-Fe_2C. It is obvious that the energy of formation for this carbide is substantially higher than for the other ones, in particular that of the stoichiometrically similar η-Fe_2C. From a purely thermodynamic viewpoint, θ_∞-Fe_2C is stable neither with respect to a phase transition (to η-Fe_2C) nor with respect to disproportionation into a carbide with smaller C content and carbon. The fact that it has been observed at all must be due to kinetic factors and the operational conditions for carburization of a Fisher-Tropsch catalyst precursor. It should also be noted that we have found this carbide only in the form of a few layers interspersed with crystallographically incommensurable ones as explained in Chapter 3. It is likely that θ_∞-Fe_2C can only be found in this form.

The relatively high energy of formation of the θ_∞-Fe_2C is interesting from a catalytic point of view. The adsorption and subsequent dissociation of CO on exposed χ-Fe_5C_2 surfaces has been studied computationally[30] and found to depend strongly on the local chemical composition and geometry. The presence of θ_∞-Fe_2C layers in between χ-Fe_5C_2 layers will add to the diversity of exposed surface sites. In general, surfaces due to less stable solids will provide higher activity. Further, apart from its role as catalyst, the carbide in a Fisher-Tropsch catalyst can also be viewed as serving as intermediate in that carbon atoms are stored in a solid solution in iron. For that function, it is important that C atoms are dissolved at relatively high energy so that they remain available for further reaction. It is probably no accident that θ_∞-Fe_2C is found in active Fisher-Tropsch catalysts and we speculate that its presence is important for good catalytic activity.

A.3.4. PAW setup input FILE's

The PAW approach requires for each atom type a setup file that defines which atomic orbitals are frozen and how the valence orbitals are related to smooth pseudized orbitals in the core region. The program ATOMPAW has been written at the Wake Forest University department of physics to provide setups for their PWPAW program. However, ATOMPAW can also produce setups for other programs such as PWSCF. Unfortunately, while PWPAW faithfully follows the orginal PAW formulation of Blöchl[3], in most current programs, including PWSCF, the Kresse implementation[5] has been followed. The difference between the two is in the handling of the so-called augmentation charge density as has been documented by Torrent et al.[20] In that paper, it was shown that the results obtained with the Kresse implementation could be affected if the augmentation charge density was too localized.

The ATOMPAW input files used in the calculations reported here were mainly based on those from the repository[19], but slightly modified to get a proper augmentation charge density. In the interest of reproducibility, the input files used are given below (in a two column format). For further details, I refer to the ATOMPAW input manual[31].

Carbon $(1s^2)2s^22p^2$

```
C 6                              n
GGA-PBE loggrid 2001             n
2 2 0 0 0 0                      VANDERBILT   besselshape
2 1 2                            2 0
0 0 0                            1.3
c                                1.3
v                                3
v                                upfdx 0.005    upfxmin -9.0   upfzmesh 1.0
1                                0
1.3   1.08   1.3   1.3
```

Iron $(1s^22s^22p^6)3s^24s^23p^64p^03d^6$

```
Fe 26                            n
GGA-PBE loggrid 2001             n
4 4 3 0 0 0                      y
3 2 6                            2
4 1 0                            n
0 0 0                            VANDERBILT   besselshape
```

c   3 0
c   2.1
v   2.1
v   2.1
c   2.1
v   2.1
v   2.1
v   3
2   upfdx 0.005   upfxmin -9.0   upfzmesh 1.0
2.1 1.75   2.1   2.1   0

A.4.   Conclusions

In Chapter 3 we concluded that, based on both powder X-ray and selected area electron diffraction evidence, the iron carbide present in a freshly carburized Fisher-Tropsch catalyst is due to a semi-random stacking of layers that in some sequences corresponds to the well known χ-Fe$_5$C$_2$, but in others to the unknown θ_∞-Fe$_2$C. This left us with questions about the relative stability of θ_∞-Fe$_2$C.

Quantum mechanical calculations of the Projector Augmented Wave (PAW) type on a range of iron carbides reveal that θ_∞-Fe$_2$C is relatively high in energy and thermodynamically unstable. Several degradation pathways would be energetically favorable, including a phase transition to the stoichiometrically equivalent η-Fe$_2$C, the most stable of all carbides. This implies that θ_∞-Fe$_2$C is formed and retained for kinetic reasons and probably only stable in a mixed layer stacking such as described in Chapter 3. It is conceivable that the presence of this metastable iron carbide is a prerequisite for an active Fisher-Tropsch catalyst.

A.5.   References

1.   Retief, J. J. Powder diffraction data and Rietveld refinement of Hägg-carbide, χ-Fe5C2. *Powder Diffr.* **14,** 130–132 (1999).

2.   du Plessis, H. E., de Villiers, J. P. R. & Kruger, G. J. Re-determination of the crystal structure of χ-Fe5C2 Hägg carbide. *Zeitschrift für Krist. - Cryst. Mater.* **222,** 211–217 (2007).

3.   Blöchl, P. E. Projector augmented-wave method. *Phys. Rev. B* **50,** 17953–17979 (1994).

4.   Faraoun, H. I., Zhang, Y. D., Esling, C. & Aourag, H. Crystalline, electronic, and magnetic structures of theta-Fe3C, chi-Fe5C2, and eta-FeC from first principle calculation. *J. Appl. Phys.* **99,** 93508 (2006).

5.   Kresse, G. & Joubert, D. From ultrasoft pseudopotentials to the projector augmented-wave method. *Phys. Rev. B* **59,** 1758–1775 (1999).

6.   de Emiel, S. *et al.* Stability and Reactivity of ε-χ-θ Iron Carbide Catalyst Phases in Fischer-Tropsch Synthesis: Controlling μc. *J. Am. Chem. Soc.* **132,** 14928–14941 (2010).

7.   Fang, C., Huis, M. Van & Zandbergen, H. Structural, electronic, and magnetic properties of iron carbide Fe_ {7} C_ {3} phases from first-principles theory. *Phys. Rev. B* **80,** 1–9 (2010).

8.   Fang, C. M., van Huis, M. A. & Zandbergen, H. W. Structure and stability of Fe2C phases from density-functional theory calculations. *Scr. Mater.* **63,** 418–421 (2010).

9.   LV, Z. Q., SUN, S. H., JIANG, P., WANG, B. Z. & FU, W. T. First-principles study on the structural stability, electronic and magnetic properties of Fe2C. *Comput. Mater. Sci.* **42,** 692–697

10.   Lyashchenko, B. G. & Sorokin, L. M. Determination of the position of carbon in cementite by the neutron diffraction method. *Sov. Physics, Crystallogr.* **8,** 300–304 (1963).

11.   Hirotsu, Y. & Nagakura, S. Crystal structure and morphology of the carbide precipitated from martensitic high carbon steel during the first stage of tempering. *Acta Met.* **20,** 645–655 (1972).

12.   J.P. Bouchard. Etude structurale des carbures de manganese. *Ann. Chim.* 392–393 (1965).

13.   Herbstein, F. H. & Snyman, J. A. Identification of Eckstrom-Adcock iron carbide as Fe7C3. *Inorg. Chem. F. Full J. Title* **3,** 894–896 (1964).

14.   Straumanis, M. E. & Kim, D. C. Lattice constants, thermal expansion coefficients, densities and perfection of structure of pure iron and iron loaded with hydrogen. *Zeitschrift für Met.* **60,** 272–277 (1969).

15.   Yamanaka, T. & Morimoto, S. Isotope effect on anharmonic thermal atomic vibration and {κ} refinement of {\sp 12}C and {\sp 3}C diamond. *Acta Crystallogr. Sect. B* **52,** 232–238 (1996).

16.   Giannozzi, P. *et al.* QUANTUM ESPRESSO: a modular and open-source software project for quantum simulations of materials. *J. Phys. Condens. Matter* **21,** 395502 (2009).

17.   Perdew, J. P., Burke, K. & Ernzerhof, M. Generalized Gradient Approximation Made Simple. *Phys. Rev. Lett.* **77,** 3865–3868 (1996).

18.   Holzwarth, N. A. W., Tackett, A. R. & Matthews, G. E. A Projector Augmented Wave (PAW) code for electronic structure calculations, Part I: atompaw for generating atom-centered functions. *Comput. Phys. Commun.* **135,** 329–347 (2001).

19.   Periodic Table of PAW Functions. (2011). Available at: http://www.wfu.edu/~natalie/papers/pwpaw/periodictable/periodictable.html.

20. Torrent, M. *et al.* Electronic structure packages: Two implementations of the projector augmented wave (PAW) formalism. *Comput. Phys. Commun.* **181,** 1862–1867 (2010).

21. Marzari, N., Vanderbilt, D., De Vita, A. & Payne, M. C. Thermal Contraction and Disordering of the Al(110) Surface. *Phys. Rev. Lett.* **82,** 3296–3299 (1999).

22. Monkhorst, H. J. & Pack, J. D. Special points for Brillouin-zone integrations. *Phys. Rev. B* **13,** 5188–5192 (1976).

23. Wijn, H. P. J. *Magnetic Properties of Metals: Alloys and Compounds of d-Elements with Main Group Elements (part 2)*. (Springer-Verlag, 1988).

24. Pauling, L. *The nature of the chemical bond*. (Cornell University Press, 1960).

25. Schwartz, M. *Principles of Electrodynamics*. (Dover Publications, 1987).

26. Tuling, A. S., du Plessis, H. E. & de Villiers, J. P. R. A TEM morphology study of Hagg iron carbide. *Proc. - Microsc. Soc. South. Afr. F. Full J. TitleProceedings - Microsc. Soc. South. Africa* **36,** 34 (2006).

27. Hohenstein, E. G., Chill, S. T. & Sherrill, C. D. Assessment of the Performance of the M05−2X and M06−2X Exchange-Correlation Functionals for Noncovalent Interactions in Biomolecules. *J. Chem. Theory Comput.* **4,** 1996–2000 (2008).

28. Hawtin, P., Lewis, J. B., Moul, N. & Phillips, R. H. The Heats of Combustion of Graphite, Diamond and Some Non-Graphitic Carbons. *Philos. Trans. R. Soc. London. Ser. A, Math. Phys. Sci.* **261,** 67–95 (1966).

29. de Smit, E. *et al.* Stability and reactivity of -chi-theta iron carbide catalyst phases in Fischer-Tropsch synthesis: controlling mu(C). PG - 14928-41. *J. Am. Chem. Soc.* **132,** 14928–14941 (2010).

30. Sorescu, D. C. Plane-Wave Density Functional Theory Investigations of the Adsorption and Activation of CO on Fe5C2 Surfaces. *J. Phys. Chem. C* **113,** 9256–9274

31. Torrent, M. A user ' s guide for atompaw code. 1–24 (2010).

Summary

This thesis focused on iron-based Fischer-Tropsch catalysts. It deals with different iron phases that might play a role in the catalytic process. As the activation step takes place inside the reactor (in-situ at high temperature and pressure), studying the catalyst activation process is not trivial. In addition, since the working catalysts are air sensitive, also post analysis on activated and used catalysts is challenging. As a result, the identity of the real active phase is still unknown.

To gain more insight in Fischer-Tropsch catalysts, we used different techniques like (in-situ) TEM, TEM-EELS, ED and PXRD. TEM and ED are very suitable techniques since they provide very high spatial resolutions (in the Å range). Special TEM grids and TEM transfer holder, with cooling option, were designed for this research in order to mimic the activation conditions and / or avoid any exposure to air.

The results indeed showed that it is essential to avoid any exposure to air prior to analysis. In fact, we can question the results of some older publications where catalysts were exposed. In contrast to literature data published so far, we found no carbon deposits on the outer rim of the iron carbides at high temperature conditions. Overall, we showed that carbon surface layers can change, or even form, during exposure to air. We also found evidence for what in the literature has been designated as "hypothetical θ_∞-Fe_2C". We proposed a structure model for which the carbon content is higher than in the pure χ-Fe_5C_2 carbide. More research is required to elucidate the exact nature of working iron-based Fischer-Tropsch catalysts.

Samenvatting

Dit proefschrift beschrijft een onderzoek aan ijzer gebaseerde Fischer-Tropsch-katalysatoren. Het behandelt verschillende ijzer-fasen die een rol kunnen spelen in het katalytische proces. Omdat de activeringsstap plaatsvindt binnen in de reactor (in situ bij hoge temperatuur en druk), is het bestuderen van het activeringsproces niet triviaal. Daarnaast zijn de katalysatoren zuurstofgevoelig wat het analyseren van geactiveerde en gebruikte katalysatoren bemoeilijkt. Als gevolg hiervan is de identiteit van de echte actieve katalytische fase nog steeds onbekend.

Om meer inzicht te krijgen in Fischer-Tropsch-katalysatoren hebben we verschillende technieken gebruikt, zoals (in-situ) TEM, TEM-EELS, ED en PXRD. TEM en ED zijn zeer geschikte technieken omdat ze zeer hoge resoluties bieden (in het Å bereik). Voor dit onderzoek zijn speciale TEM-grids en een TEM-houder, met optie om te koelen, ontworpen om de activeringsomstandigheden na te bootsen en / of blootstelling aan lucht te vermijden.

Onze resultaten tonen inderdaad aan dat het essentieel is om elke blootstelling aan lucht vóór analyses te vermijden. In feite kunnen we de resultaten van sommige oudere publicaties in twijfel trekken waarin katalysatoren aan lucht zijn blootgesteld. In tegenstelling tot eerdere publicaties hebben we bij hoge temperatuur geen koolstofafzettingen op de buitenrand van de ijzercarbiden gevonden. We hebben aangetoond dat koolstofoppervlaktelagen kunnen veranderen, of zelfs kunnen vormen, tijdens blootstelling aan lucht. We hebben ook bewijs gevonden voor wat in de literatuur is aangeduid als "hypothetisch θ_∞-Fe$_2$C". We hebben een structuurmodel voorgesteld waarin het koolstofgehalte hoger is dan voor het zuivere χ-Fe$_5$C$_2$-carbide. Er is nog alrijd meer onderzoek nodig om de precieze aard van de werkende ijzer Fischer-Tropsch-katalysatoren op te helderen.

List of patents and publications

Janbroers, S. et al., (2011), A model study on the carburization process of iron-based Fischer-Tropsch catalysts using in situ TEM-EELS. Applied Catalysis B: Environmental, 102, Issues 3–4, 521–527

Janbroers, S. et al., (2009), Preparation of carbon-free TEM microgrids by metal sputtering. Ultramicroscopy, 109, 1105-1109

Janbroers, S. et al., (2009), Insights into the nature of iron-based Fischer-Tropsch catalysts from quasi in situ TEM-EELS and XRD. Journal of Catalysis, 268, 235-242

Yildiz, G. et al., (2012) Catalytic fast pyrolysis of biomass. Communications in agricultural and applied biological sciences 77, 73–77

US6565643 B2 / EP1252096 B1 - Process for preparing clay minerals

US6537442B - Cogel containing oxidic compounds of tetravalent, trivalent and divalent metallic elements

US7781619 BB - Process for the decarboxylation of fatty acids

US8980782 - Bulk sulfidic mixed metal catalyst and methods for its manufacture and use in converting syngas to alcohol

WO07107336 - Silicoaluminophosphate isomerization catalyst

WO07141293 - Catalytic hydrodeoxygenation of an oxygenate feedstock

Dankwoord

Vele mensen hebben bijgedragen gedurende de lange periode dat ik aan dit proefschrift heb gewerkt. Allereerst wil ik mijn co-promotor Patricia Kooyman bedanken. Patricia is diegene die deze promotie heeft geïnitieerd en mede heeft vormgegeven. Ze heeft altijd in mij geloofd, mij gesteund en mij continue aangespoord om door te zetten. Patricia, dankjewel! Verder ben ik veel dank verschuldigd aan Eelco Vogt. Hij heeft het mogelijk gemaakt dat ik parallel aan mijn werkzaamheden bij Albemarle dit promotieonderzoek heb kunnen uitvoeren. Ik wil ook mijn promotor Henny Zandbergen bedanken voor de steun, goede adviezen en natuurlijk dat ik in zijn onderzoeksgroep terecht kon! Verder wil ik Jaap Louwen bedanken voor zijn bijdragen en goede dicussies om het één en ander te ontrafelen. Jaap, ik denk met veel plezier terug aan onze gesprekken over werk, promotie en privé! Verder ook dank aan Tosca Langereis voor de hulp met de Casimir aanvraag. Ik wil ook Mark de Boer, Leon van den Oetelaar en Edgar Steenwinkel, mijn lijnmanagers die na Eelco zijn gekomen, bedanken voor hun geduld en steun. Het is niet altijd makkelijk om zo'n onderzoek naast het "gewone" werk uit te voeren. Dan zijn er natuurlijk Esther Schilder, Jelle Kampen, Pieter Schreuder, Bert Klaver en Leo van der Ende. Zonder jullie hulp had er allemaal weinig van terecht gekomen. Ook aan de kant van de universiteit heb ik de nodige ondersteuning gehad. In het bijzonder wil ik Frans Tichelaar, Jouk Jansen en Tom de Kruijff danken voor de ondersteuning. Het was mij een groot genoegen met jullie samen te werken! Also many thanks to Peter Crozier. I spent a wonderful time at ASU. Simply writing this already brings a big smile to my face. I hope to run into you at conferences for many years to come. Also many thanks to Burtron Davis. It was great spending some time at the CAER. I really appreciated your input on testing conditions but most of all showing me around Kentucky.

Mijn ouders ben ik dankbaar voor hun onvoorwaardelijke steun, in goede en slechte tijden zoals het overlijden van Andreea. Andreea heeft nog teksten uit dit proefschrift nagekeken en was een groot voorstander dat ik deze promotie zou afronden.

Rust zacht lieve Andreea.

Ten slotte wil ik Natallia, Tim, Anna en Shorab bedanken. Jullie zijn mijn steun en toeverlaat. Laten we er samen iets moois van maken!

Curriculum Vitae

Stephan Janbroers is geboren op 17 september 1971 in Amsterdam. Hij behaalde in 1987 zijn M.A.V.O. diploma aan de "P.C. Mavo Noord". Aansluitend heeft hij aan de Hoge School van Amsterdam eerst het MLO afgerond met een onderzoeksverslag over nieuwe oplosmiddelen voor verf uitgevoerd bij het toenmalige Koninklijke Shell Laboratorium in Amsterdam. Daarna heeft Stephan het HLO afgerond. Hij behaalde in 1994 zijn ingenieursdiploma met een scriptie over ontzwavelingskatalysatoren uitgevoerd bij het toenmalige Akzo in Amsterdam. Sinds 1994 was Stephan werkzaam bij Akzo, wat later Akzo-Nobel en weer later Albemarle Catalysts is geworden. Gedurende een periode van bijna 20 jaar heeft hij daar verschillende functies vervuld. Allereerst als chemisch analyst daarna als project leider, sectiechef en uiteindelijk als groepshoofd verantwoordelijk voor 3 R&D afdelingen binnen Albemarle. Tijdens deze periode heeft Stephan verschillende bijdragen geleverd op het gebied van katalyse, getuige meerdere patenten en publicaties. Naast zijn werkzaamheden bij Albemarle heeft Stephan vanaf 2005 in deeltijd gewerkt aan dit promotieonderzoek. Sinds 2012 is Stephan werkzaam bij Avantium Chemicals als Director Business Development.